AD-A074 891 COMPUTER SCIENCES CORP ALBUQUERQUE N MEX F/G 19/4
HULL MODELING OF STRESS WAVE PROPAGATION.(U)
JUL 79 M A FRY, L P GABY F29601-78-C-0012
UNCLASSIFIED CSC-C4-C-4083 AFWL-TR-79-17 NL

1 OF 2
AD A074891

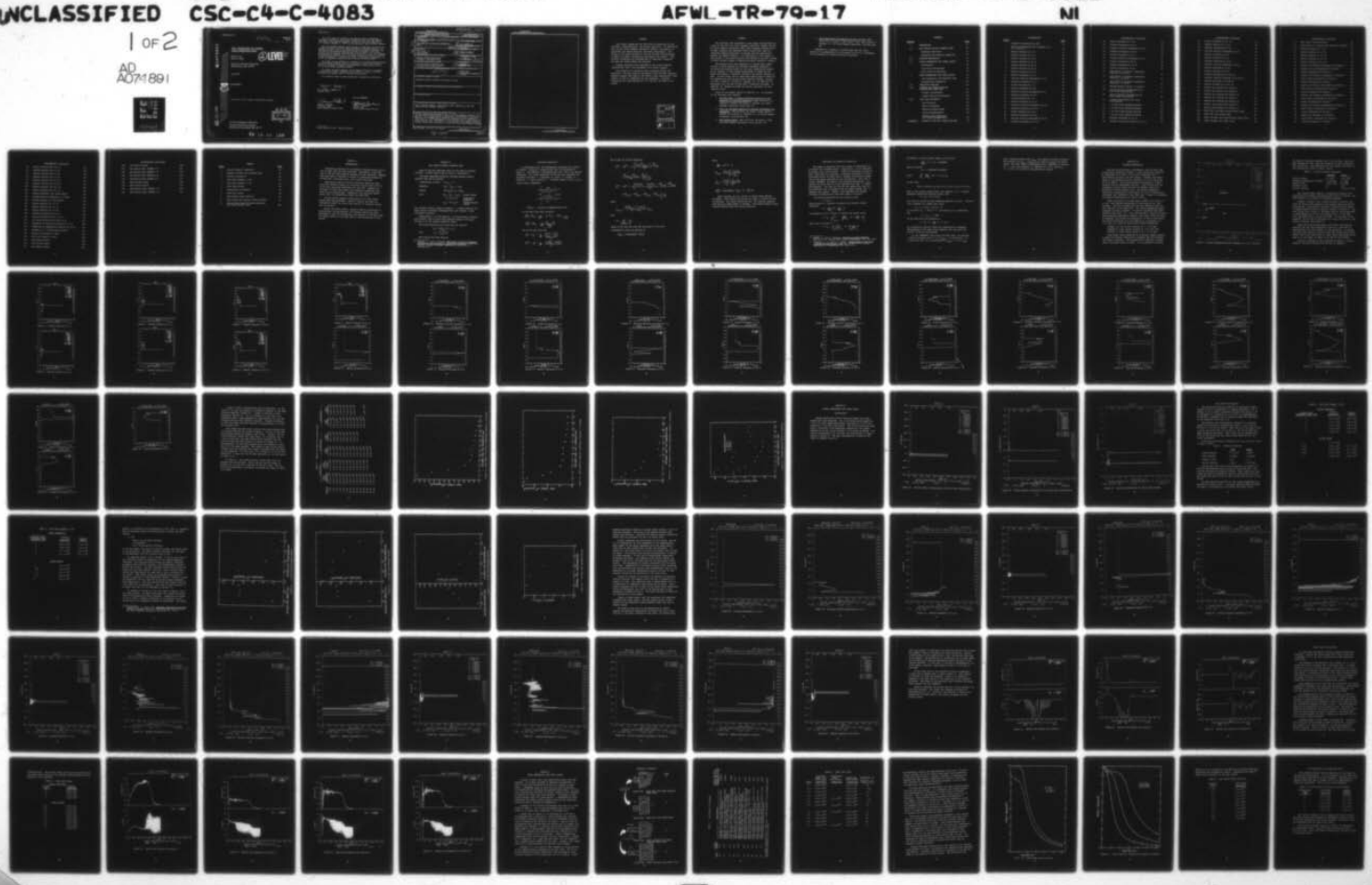

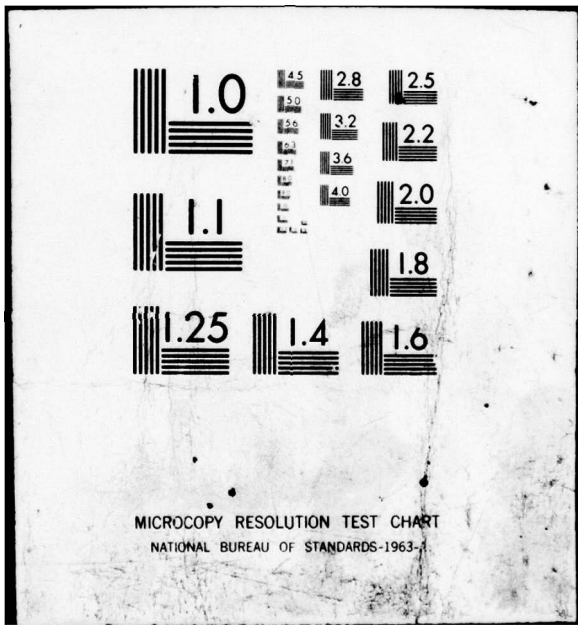
1.0
1.1
1.25
1.4
1.6
1.8
2.0
2.2
2.5
2.8
3.2
3.6
4.0
4.5
5.0
5.6
MICROCOPY RESOLUTION TEST CHART
NATIONAL BUREAU OF STANDARDS-1963-A

HULL MODELING OF STRESS WAVE PROPAGATION

(2) LEVEL III

Mark A. Fry
Lewis P. Gaby

Computer Sciences Corporation
Albuquerque, NM 87108

July 1979

Final Report

Approved for public release; distribution unlimited.

Air Force Weapons Laboratory
Air Force Systems Command
Kirtland Air Force Base, NM 87117

This final report was prepared by the Computer Sciences Corporation, Albuquerque, New Mexico, under Contract F29601-78-C-0012, Job Order 88091821 with the Air Force Weapons Laboratory, Kirtland Air Force Base, New Mexico. Dr. Clifford E. Rhoades, Jr. (DYP) was the Laboratory Project Officer-in-Charge.

This report has been reviewed by the Information Office and is releasable to the National Technical Information Service (NTIS). At NTIS, it will be available to the general public, including foreign nations.

This technical report has been reviewed and is approved for publication.

Clifford P. Rhoades, Jr.

DR. CLIFFORD E. RHOADES, JR.
Project Officer

FOR THE COMMANDER

Norman F. Roderick

NORMAN F. RODERICK
Lt Colonel, USAF
Chief, Advanced Concepts Branch

Thomas W. Ciambrone

THOMAS W. CIAMBRONE
Colonel, USAF
Chief, Applied Physics Division

DO NOT RETURN THIS COPY. RETAIN OR DESTROY.

(18) AFWL, SBIE

UNCLASSIFIED

SECURITY CLASSIFICATION OF THIS PAGE (When Data Entered)

(19) **REPORT DOCUMENTATION PAGE**

READ INSTRUCTIONS BEFORE COMPLETING FORM

1. REPORT NUMBER: AFWL-TR-79-17	2. GOVT ACCESSION NO.: AD-E200 366
3. RECIPIENT'S CATALOG NUMBER:	
4. TITLE (and Subtitle): (6) HULL MODELING OF STRESS WAVE PROPAGATION.	5. TYPE OF REPORT & PERIOD COVERED: (9) Final Report
	6. PERFORMING ORG. REPORT NUMBER: (14) CSC-C4-C-4083
7. AUTHOR(s): (10) Mark A. Fry, Lewis P. Gaby	8. CONTRACT OR GRANT NUMBER(s): (15) F29601-78-C-0012
9. PERFORMING ORGANIZATION NAME AND ADDRESS: Computer Sciences Corporation 409656, Albuquerque, New Mexico 87108	10. PROGRAM ELEMENT, PROJECT, TASK AREA & WORK UNIT NUMBERS: (16) 62601F 88091821 (17) (18)
11. CONTROLLING OFFICE NAME AND ADDRESS: Air Force Weapons Laboratory (DYP), Kirtland Air Force Base, NM 87117	12. REPORT DATE: (11) July 1979
	13. NUMBER OF PAGES: 172
14. MONITORING AGENCY NAME & ADDRESS (if different from Controlling Office): (12) 173.	15. SECURITY CLASS. (of this report): UNCLASSIFIED
	15a. DECLASSIFICATION/DOWNGRADING SCHEDULE:

16. DISTRIBUTION STATEMENT (of this Report)

Approved for public release; distribution unlimited.

17. DISTRIBUTION STATEMENT (of the abstract entered in Block 20, if different from Report)

18. SUPPLEMENTARY NOTES

19. KEY WORDS (Continue on reverse side if necessary and identify by block number)

HULL, continuum mechanics, shock physics, armor, penetration, IBM, CRAY, ground coupling, fireball, radiation.

20. ABSTRACT (Continue on reverse side if necessary and identify by block number)

The HULL computer code developed by AFATL (Air Force Armaments Laboratory) has been utilized to perform studies of conventional, nonconventional, and nuclear munitions. The phenomenology of penetrator mechanics has been studied and a model proposed. Initial groundwork for using the HULL code in ground coupling studies has been laid. Additionally, in anticipation of new computer machinery, the HULL code has been converted to run upon both IBM and CRAY computer systems.

DD FORM 1 JAN 73 1473 EDITION OF 1 NOV 65 IS OBSOLETE

UNCLASSIFIED

SECURITY CLASSIFICATION OF THIS PAGE (When Data Entered)

409656

SUMMARY

This report summarizes the work done in simulation of conventional, nonconventional, and nuclear munitions. In cooperation with the Air Force Armament Laboratory (AFATL), the effects of penetrator and target materials have been investigated. The thrust of the study has been to utilize the HULL code developed by AFATL to produce calculations and analyze the results. Conclusions concerning the phenomenology of penetrator mechanics are made and simple models are proposed.

Nuclear munitions were addressed in the ground coupling investigation which laid groundwork for further research.

The process of an extensive code conversion effort are described. The HULL code was converted to IBM and CRAY computers. Numerous changes were made to the Control Data Corporation's (CDC) version to make it compatible for the machinery. Run-time comparisons are made between CDC 176, IBM 360, and CRAY-1 computers.

PREFACE

The technical work described in this report was performed as a part of the joint Air Force Armament Laboratory (AFATL) and the Air Force Weapons Laboratory (AFWL) HULL computer program effort. At AFWL, research was performed under Project 8809, Task 18, "Advanced Computer Simulation of Nuclear and Non-Conventional Weapons and Weapons Effects." All references in this report to HULL relate to the elastic-plastic HULL system as written in-house at AFATL by Major Daniel A. Matuska and Major Richard E. Durrett.

The authors would like especially to express their appreciation to Major Matuska who provided invaluable guidance in outlining the research goals for the armor penetration program. We are thankful to Miss Cydney Westmoreland of AFATL for her expert assistance in carefully verifying the various versions of HULL. We also would like to thank Major Marvin Alme of AFWL for his comments and help on the ground coupling problem. Finally, we wish to thank Dr. Clifford E. Rhoades, Jr., of AFWL for his assistance with the IBM 370 and CRAY-1 conversion problems. In addition, Dr. Rhoades provided the overall management of this research effort.

Users of this report should be familiar with the contents of the following four reports:

1. The HULL Code: A Finite Difference Solution to the Equations of Continuum Mechanics, AFATL TR-78-115, by Richard E. Durrett and Daniel A. Matuska, Air Force Armament Laboratory, Eglin AFB, Fl.
2. SAIL, An Automated Approach to Software Development and Management, AFWL TR-78-80, by Lewis P. Gaby, David H. Graham, and Clifford E. Rhoades, Jr., Air Force Weapons Laboratory, Kirtland AFB, NM.
3. HULL System Report, AFWL TR-78-115, by Lewis P. Gaby, Air Force Weapons Laboratory, Kirtland AFB, NM.

4. The Installation and Operation of HULL on 370s, AFWL TR-78-134, by Lewis P. Gaby, Mark A. Fry, and Clifford E. Rhoades, Jr., Air Force Weapons Laboratory, Kirtland AFB, NM.

Reference to a company or product name does not imply approval or recommendation of the product by the U.S. Government to the exclusion of others that may be suitable.

CONTENTS

ILLUSTRATIONS

ILLUSTRATIONS (continued)

ILLUSTRATIONS (continued)

ILLUSTRATIONS (continued)

ILLUSTRATIONS (continued)

ILLUSTRATIONS (continued)

TABLES

SECTION I

INTRODUCTION

Theoretical modeling for solid-media response events utilizing the HULL code has been performed. Conversion of the HULL code to IBM and CRAY computer systems has been completed. Efforts have been made to simulate a variety of conditions produced by conventional, nonconventional, and nuclear munitions.

Penetration events of metal projectiles impacting armor plate and concrete targets at velocities ranging from 3,000 to 25,000 ft/s have been simulated with the code. Spheres and cylinders of steel and copper with different geometries were used for the calculations. Comparison with available experimental data for penetration events has been made.

Initial ground coupling calculations of a 1-MT nuclear source have been performed. Results indicate the need for developing a model for early-time coupling of radiation energy into the ground.

During the entire effort, numerous sample calculations of conventional, nonconventional, and nuclear events have been performed to test the faithfulness and modeling of the HULL code. The latest version of the HULL code is the end product of this testing.

SECTION II

HULL ELASTIC PLASTIC COMPUTER CODE

Some of the more important parts of the code are briefly outlined. Further details may be found in Reference 1.

The basic equations solved by the HULL Elastic Plastic Computer Code are as follows:

Conservation of Mass	$\dot{\rho}-\rho u_{i,i} = 0$	
Momentum	$\rho\dot{u}_j - T_{ij,i} = -\rho g_j$	
Energy	$\rho\dot{E}-(T_{ij}U_j)_{,i} = -\rho U_j g_j .$	
Here	$T_{ij} = S_{ij} - \delta_{ij}P$	stress tensor
	$P = P(\rho,I,h)$	hydrostatic pressure
	$S_{ij} = S(\varepsilon,\varepsilon_p,I)$	stress deviator tensor

The repeated indices indicate summation. A comma preceding the index refers to partial differentiation with respect to that coordinate direction.

Additionally, ρ is the density, u is the material velocity, g is gravity, and E is the total specific energy, $E=I+U_iU_i/2$ defining I as the internal specific energy.

The stress deviators are found from the relation

$$S_{ij} = 2G\left(\dot{\varepsilon}_{ij}-1/3\ u_{i',i}\right)$$

with

$$\varepsilon_{ij} = \frac{u_{i',j}+u_{j,i}}{2}$$

and G being the shear modulus.

---

1. Durrett, R., and D. Matuska, HULL Code, A Finite Difference Solution to the Equations of Continuous Mechanics, AFATL TR-78-125, Air Force Armament Laboratory, Eglin AFB, Fl., December 1978.

Difference Equations

In difference form, the hydrodynamic equations are written as follows. Consider a computational cell as designated in Figure 1. The quantity n represents time, and i and j are spacial directions. All other quantities inside the cell represent the variables involved: P - pressure, m - mass, V - volume, u - velocity, v - axial velocity, I - internal energy, and S_r, S_z, T_{rz} - stress sensor components.

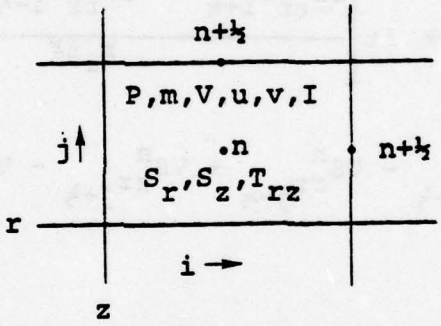

Figure 1. Diagram of Computational Cell

At the half time step, we write

$$p_{i+\frac{1}{2}}^{n+\frac{1}{2}} = p_{i+\frac{1}{2}}^{n} - \frac{\Delta t}{2\Delta r}\left(r\,u^{n}_{i+1} - r^{n}u_i^{n}\right)\frac{1}{r_{i+\frac{1}{2}}}$$

$$U_{i+\frac{1}{2}}^{n+\frac{1}{2}} = U_{i+\frac{1}{2}}^{n} - \frac{\Delta t}{2\Delta r}\frac{P_{i+1}^{n} - P_i^{n}}{\rho_{i+\frac{1}{2}}^{n+\frac{1}{2}}}$$

and at the new time step

$$U_i^{n+1} = U_i^{n} - \frac{\Delta t}{\Delta r}\frac{\left(P^{n+\frac{1}{2}}_{i+\frac{1}{2}} - P^{n+\frac{1}{2}}_{i-\frac{1}{2}}\right)}{\rho^{n}}$$

$$E_i^{n+1} = E_i^{n} - \frac{\Delta t}{\Delta r}\frac{rPu_{i+\frac{1}{2}}^{n+\frac{1}{2}} - rPu_{i-\frac{1}{2}}^{n-\frac{1}{2}}}{\rho^{n}}$$

Now we add the stress components

$$U_i^{n+1} = U_i^{n+1} + \Delta t \left[\frac{r_{i+\frac{1}{2}} S^n_{rr_{i+\frac{1}{2}}} - r_i S^n_{rr_{i-\frac{1}{2}}}}{r_i \Delta r} \right.$$

$$\left. + \frac{S^n_{rz_{i+\frac{1}{2}}} - S^n_{rz_{i-\frac{1}{2}}}}{\Delta Z} - \frac{S^n_{\theta\theta_i}}{r_i} \right] \frac{1}{\rho_i^n}$$

$$E_i^{n+1} = E_i^{n+1} + \Delta t \left[\frac{rS_{rr} U^n_{i+\frac{1}{2}} - rS_{rr} U^n_{i-\frac{1}{2}} + VS^n_{rz_{i+\frac{1}{2}}} - VS^n_{rz_{i+\frac{1}{2}}}}{r_i \Delta r} \right.$$

$$\left. + US^n_{rz_{j+\frac{1}{2}}} - US^n_{rz_{j-\frac{1}{2}}} + VS^n_{zz_{j+\frac{1}{2}}} - VS^n_{zz_{j-\frac{1}{2}}} \right] \frac{1}{\rho_i^n}$$

where

$$S_{rr_{i+\frac{1}{2}}} = \frac{\left(\rho_i S^n_{rr_{i+1}} + \rho_{i+1} S_{rr_i} \right)}{\rho_i + \rho_{i+1}} \delta V_{i+\frac{1}{2}}$$

here

$$\delta V = \sum_{K=\text{solid}} \frac{V_K}{V_T} ,$$

which is the sum over only the solid part of the cell.

Intermediate values are defined as

$$\rho C^2_{i+\frac{1}{2}} = \text{minimum} \left(\rho C^2_i, \rho C^2_{i+1} \right)$$

where

$$\frac{dp}{dt} = -\rho c^2 \vec{\nabla} \cdot \vec{U}$$

$$p^n_{i+\frac{1}{2}} = \frac{\rho^n_{i+1}\, p^n_i + \rho^n_i\, p^n_{i+1}}{\rho^n_i + \rho^n_{i+1}}$$

$$U^n_{i+\frac{1}{2}} = \frac{\rho^n_i\, U^n_i + \rho^n_{i+1}\, U^n_{i+1}}{\rho^n_i + \rho^{n+1}_i}$$

$$\rho^{n+\frac{1}{2}}_{i+\frac{1}{2}} = \text{maximum}\left(\rho^n_i,\ \rho^n_{i+1}\right) \cdot \left(1 - \frac{\Delta t}{2}\, \delta u\right)$$

These averages act as a filter to weight sharp density gradients. When density variations are small, a simple average is obtained. For sharp discontinuities, the physical quantity from the more dense region is favored. This method tends to keep discontinuities sharp and retard diffusion.

Addressing the Material Properties

The types of materials that this report is concerned with are metals and crushable media. Specifically, we are referring to copper, iron, and concrete. A PROC (a collection of cards in SAIL, identified for inclusion in multiple locations) has been formulated within the HULL code to address the material properties of the media simulated by the calculations. This PROC is called "GREENMET" and employs the following methodology. The equation of state form is a Mie-Gruneisen form (Ref. 2, Bakken and Anderson). The data for fitting the temperature into the Mie-Gruneisen form is obtained from the ANEOS program (Ref. 3, Thompson and Lauson). Finally, work hardening and thermal softening characteristics have been added to the PROC.

The Mie-Gruneisen EOS has the following form

$$P = P(\rho, I)$$

where stress is a function of density and internal energy. Therefore,

$$dP = \left(\frac{\partial P}{\partial \rho}\right)_I d\rho + \left(\frac{\partial P}{\partial I}\right)_\rho dI$$

An integration over a region of density and energy gives

$$P = P_o + \int_{\rho_o, I_o}^{\rho, I} \left[\left(\frac{\partial P}{\partial \rho}\right)_{I_o} d\rho + \left(\frac{\partial \rho}{\partial I}\right)_\rho dI\right]$$

which can be written as

$$P = P_o + \int_{\rho_o}^{\rho} \left[\left(\frac{\partial P}{\partial \rho}\right)_{I_o} d\rho + \int_{I_o}^{I} \left(\frac{\partial P}{\partial I}\right)_{\rho_o} dI\right.$$

---

2. Bakken, L., and P. Anderson, Equation of State Handbook, SCL OR 66 123, Sandia Laboratories, Albuquerque, NM, Jan. 1969.

3. Thompson, S. L., and H. S. Lauson, Improvements in the Chart D Radiation Hydrodynamic Code III, SC-RR-71-0714, Sandia Laboratories, Albuquerque, NM, March 1972.

For metals in the solid-melt phase, we can write

$$\left(\frac{\partial P}{\partial I}\right)_\rho = \rho\ \Gamma\ (\rho) = \text{CONSTANT}$$

where we define

$\Gamma(\rho)$ = Gruneisen Parameter

Since $$\int_{\rho_o}^{\rho} \left(\frac{\partial P}{\partial \rho}\right)_{I_o} d\rho = P\ (\rho, I_o) - P_o$$

we can write

$$P = P(\rho, I) = P_o + P(\rho, I_o) - P_o + \rho\,\Gamma(\rho)\,(I - I_o) = P(\rho, I_o) + \rho\,\Gamma(\rho)\,(I - I_o)$$

Now, if the initial state follows the Hugoniot, i.e., a single parameter defines the physical state, then

$$P = P_H + \Gamma(\rho)\,\rho(I - I_H)$$

This form is called the Mie-Gruneisen equation of state. Conservation of energy at a shock front gives

$$I_H - I_o = \tfrac{1}{2}(P_o + P_H)(V_o - V)$$

If initially $P_o = 0$ and $I_o = 0$ and defining in a traditional way

$$\mu = \rho/\rho_o - 1 = \frac{V_o}{V} - 1$$

we can then write the equation as

$$P = P_H\ (1 - \frac{\Gamma(\rho)}{2}\ \mu) + \Gamma(\rho)\,\rho I$$

P_H is generally found by using the conservation of momentum relationship at the shock front together with the shock and particle velocity relationship.

In the "GREENMET" PROC within the HULL code, the pressure P remains unlimited until $E = 0.6\ E_{melt}$. At that point, if P is less than zero, it is multiplied by $(E_{melt} - E)/0.4\ E_{melt}$.

When E becomes greater than E_{melt}, the pressure becomes unlimited. We currently use $E_{melt} = E_{melt}(\rho_o, P_o)$ where P_o equals one atmosphere. The vapor state is addressed within "GREENMET" as follows: if $\rho < 0.8\rho_o$, the pressure is a maximum of P or P_G where $P_G = (\gamma - 1)\rho(E - ES)$ and ES is the sublimation energy.

SECTION III

CONCRETE PENETRATION

The HULL elastic-plastic hydrodynamic code has been used to calculate penetration events. A steel projectile traveling at velocities of 25,000 to 10,000 ft/s impacting into a semi-infinite concrete slab was modeled. Geometry and dimensions of the penetration were a cylinder of 2.6 cm radius and 10 cm in length. The concrete medium was modeled as a semi-infinite slab of homogeneous concrete. Time history data was collected at points along the axis of symmetry within the projectile and the concrete slab. The stress components, velocities, accelerations, and density at each of these points (stations) were recorded at each time step. Figure 2 illustrates the problem configuration at initial time t_o.

These calculations utilized square zoning with ΔX and ΔY = 0.2 cm. The problem configuration is the same for all four problems. The only variable that has been changed is the initial velocity of the penetrator. The elastic-perfectly plastic treatment has been included. A constant atmosphere and three materials were used; air, iron, and concrete. Stations (points) which simulate experimental sensors) were placed along the axis of symmetry, both within the penetrator, as well as the target. The three calculations will be referred to as problems 11.1, 11.2, and 11.3 since the figures have these designations.

Problem 11.1 has initial velocity of $5. \times 10^5$ cm/s
Problem 11.2 has initial velocity of 7.62×10^5 cm/s
Problem 11.3 has initial velocity of $3. \times 10^5$ cm/s

High stress levels generated by projectile impacts require a model for concrete constitutive relations that will address the range of interest. The concrete model used here is based upon a very small amount of data. It is intended to simulate

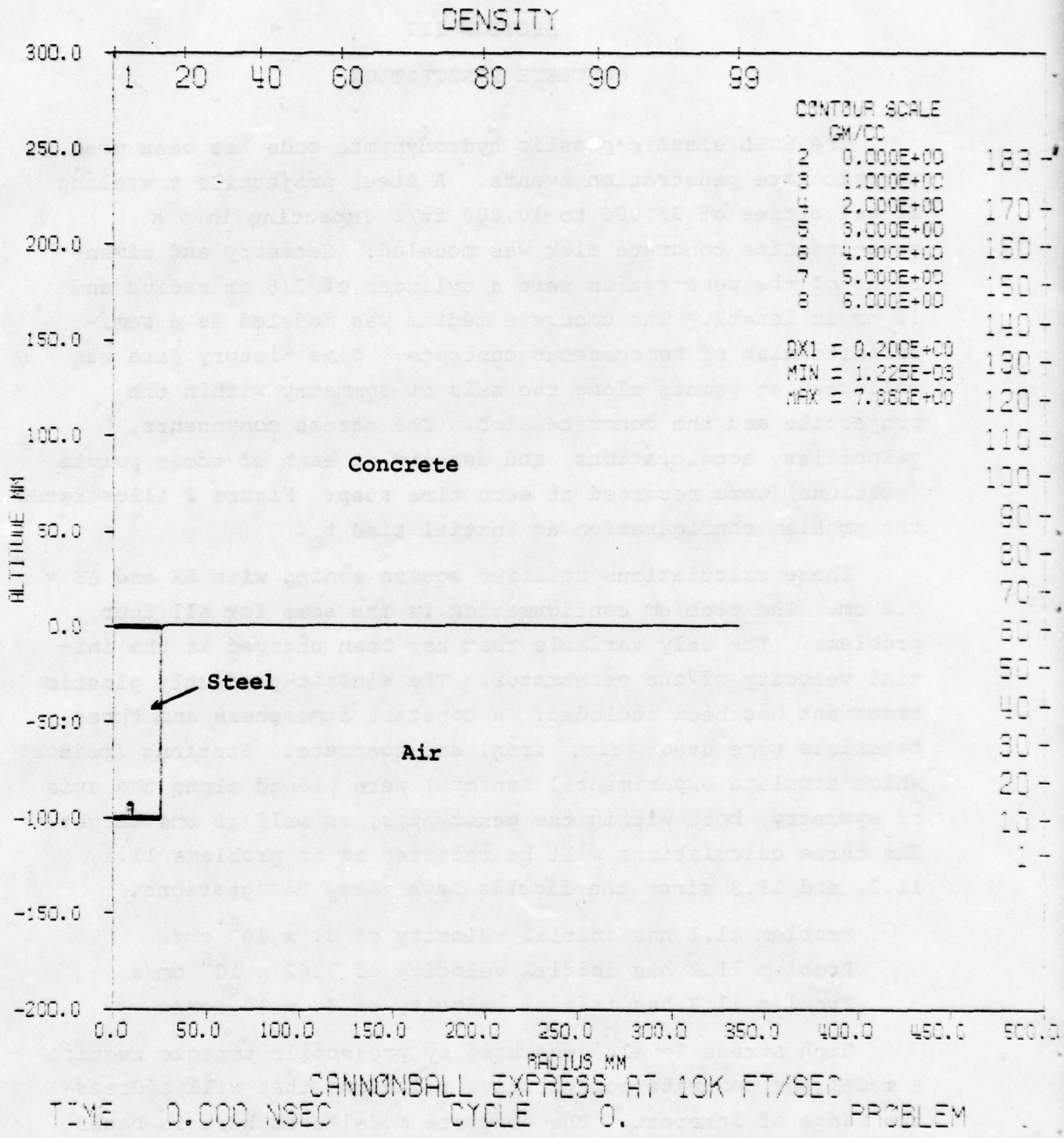

Figure 2. Initial Configuration for Problems 11.1, 11.2, and 11.3

the range of concrete responses from 1 to 300 kbar. Note that peak stresses of over 1 mbar are generated by the projectile in this calculation. The properties for the concrete and steel in this problem are listed in Table 1 below.

Table 1. Initial Material Properties

	Concrete	Steel
Initial density	2.2 g/cm^3	7.86 g/cm^3
Unconfined compressive strength	0.3345 kbar	4.7 kbar
Tensile limit	0.0115 kbar	12.0 kbar
Poisson's ratio	0.2	0.35
Initial velocity	0	7.62 x 10^5 cm/s

The concrete model supplies a hydrostatic pressure which replicates the crushing of concrete during initial loading. The yield surface is a function of confining pressure.

Figures 3 through 9 are a series of plots of density contours at various time intervals which clearly shows the spatial distribution. After impact, the nose of the penetrator begins to expand radially into the concrete (Figures 4 through 7). The last contour plot, Figure 9, indicates that the steel penetrator is approximately 15 cm into the concrete slab. At the same time, the shock wave is moving out ahead. On the front of the waveform, one can see the existence of a small wave which is the elastic precursor (see Figure 5).

These plots and similar plots of the other calculations indicate that the steel penetrator "digs out" a hole that is approximately twice the diameter of the penetrator. By examining peak stress levels at various times and extrapolating those levels down to the yield point at later times, some guess can be made as to the extent of damage to be done in the concrete.

Figures 10 through 33 are histograms of density, velocity, pressure, and axial stress along the axis of symmetry.

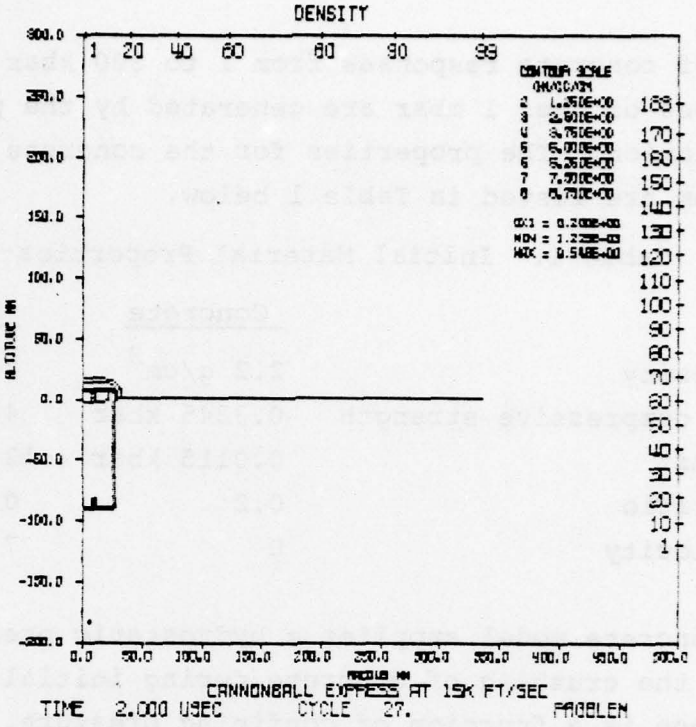

Figure 3. Density Contours at 2 μs

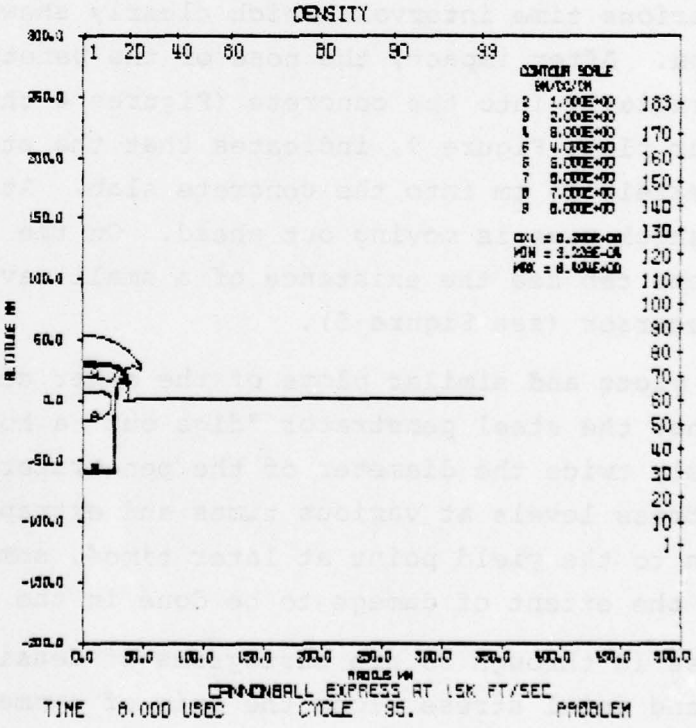

Figure 4. Density Contours at 8 μs

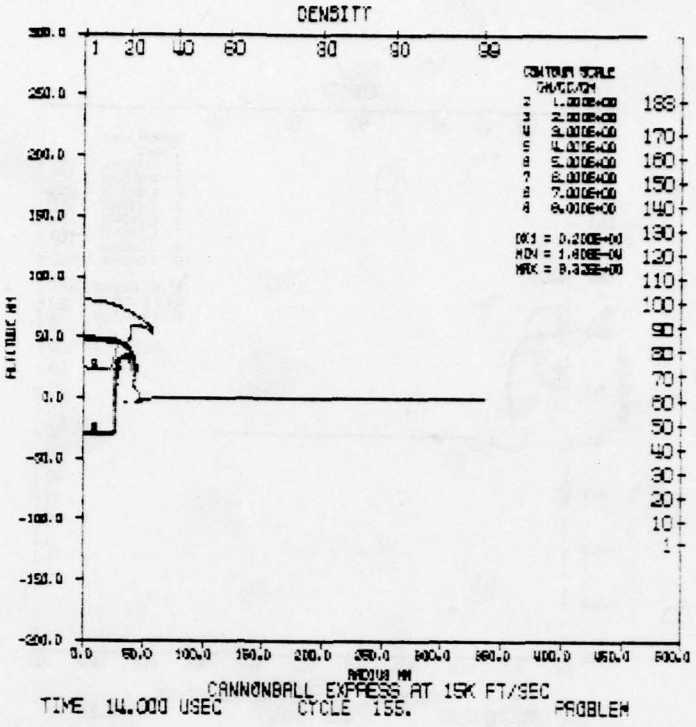

Figure 5. Density Contours at 14 μs

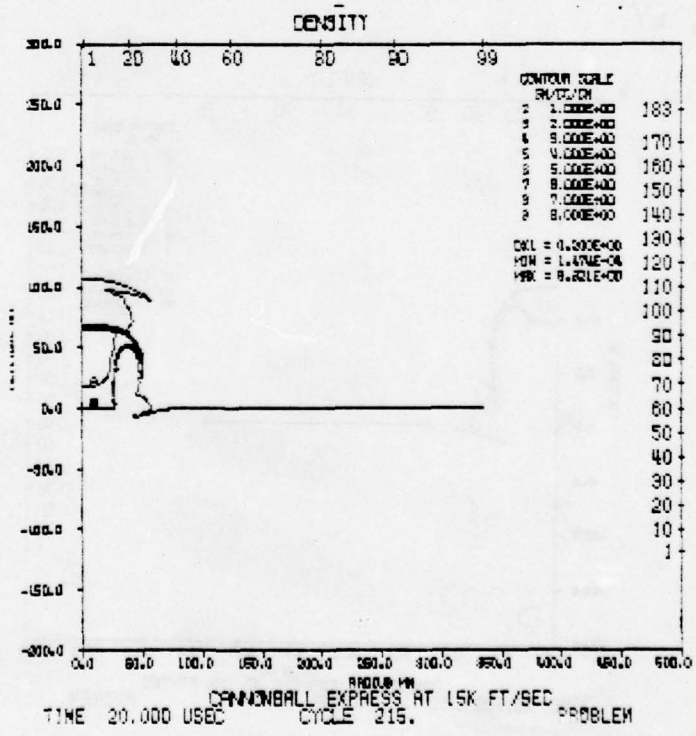

Figure 6. Density Contours at 20 μs

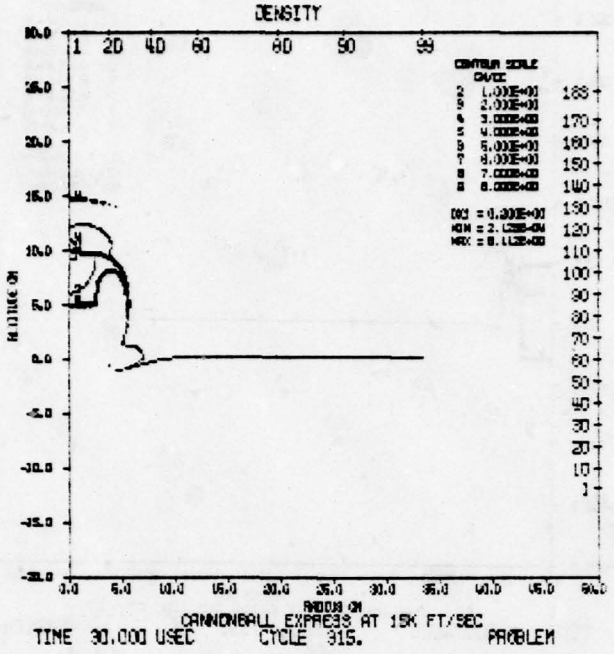

Figure 7. Density Contours at 30 μs

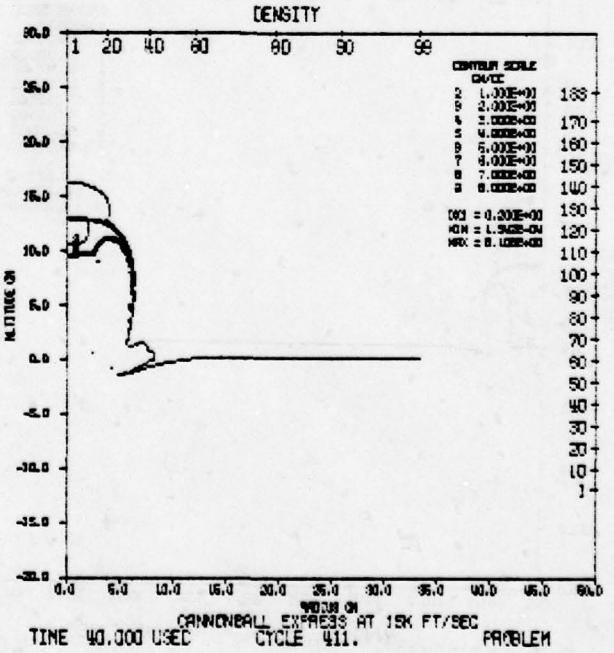

Figure 8. Density Contours at 40 μs

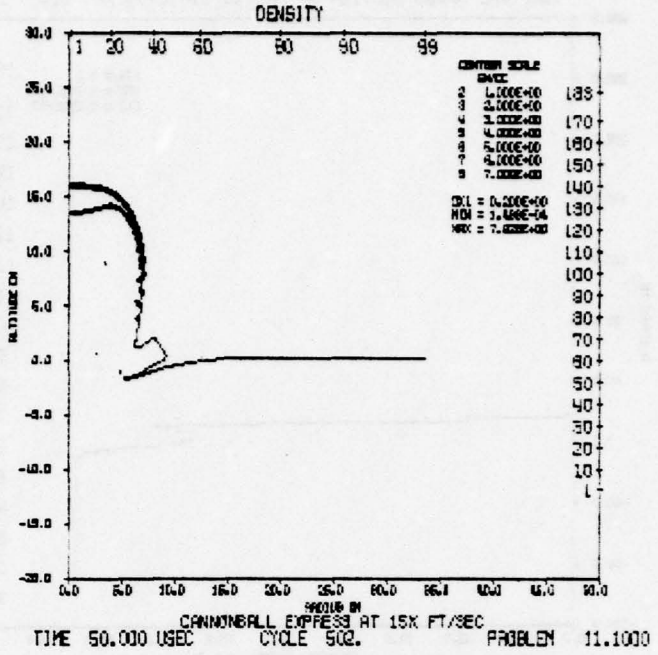

Figure 9. Density Contours at 50 μs

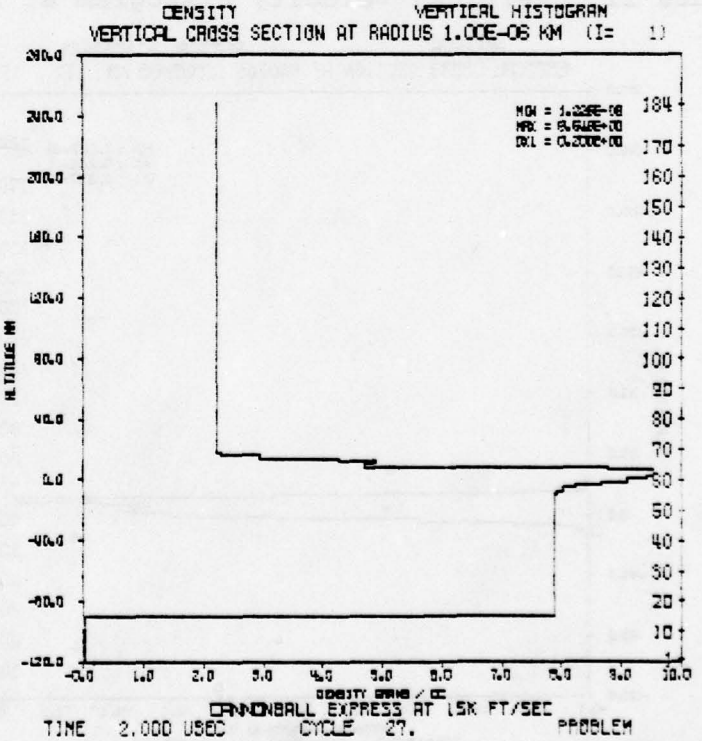

Figure 10. Density Histogram at 2 μs

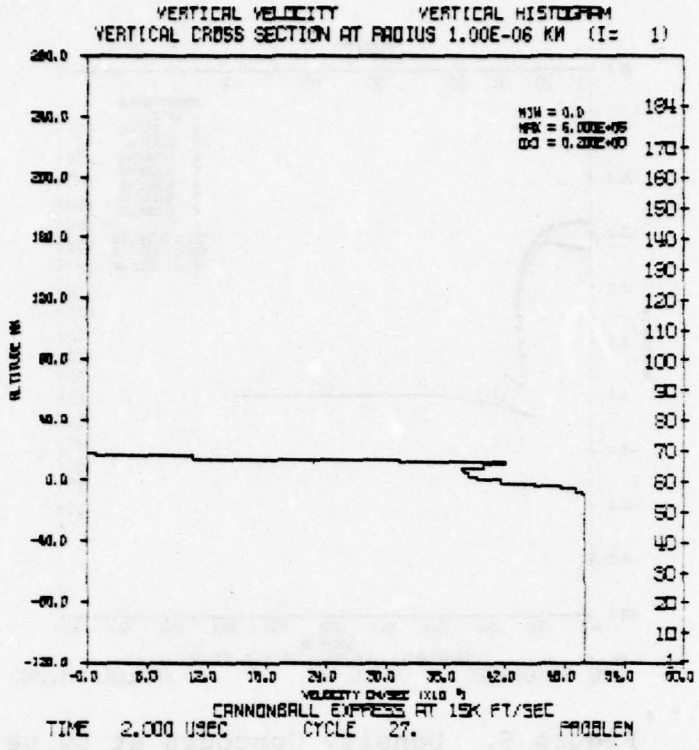

Figure 11. Vertical Velocity Histogram at 2 μs

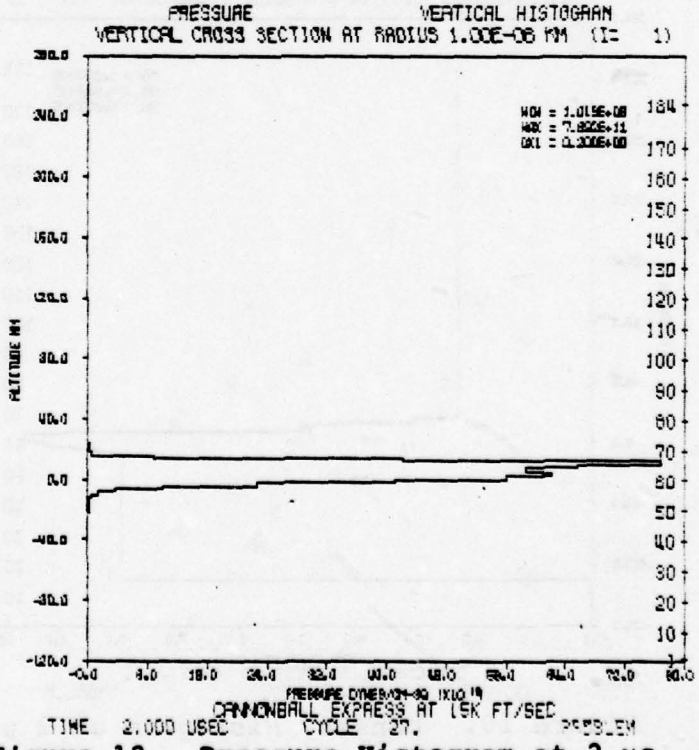

Figure 12. Pressure Histogram at 2 μs

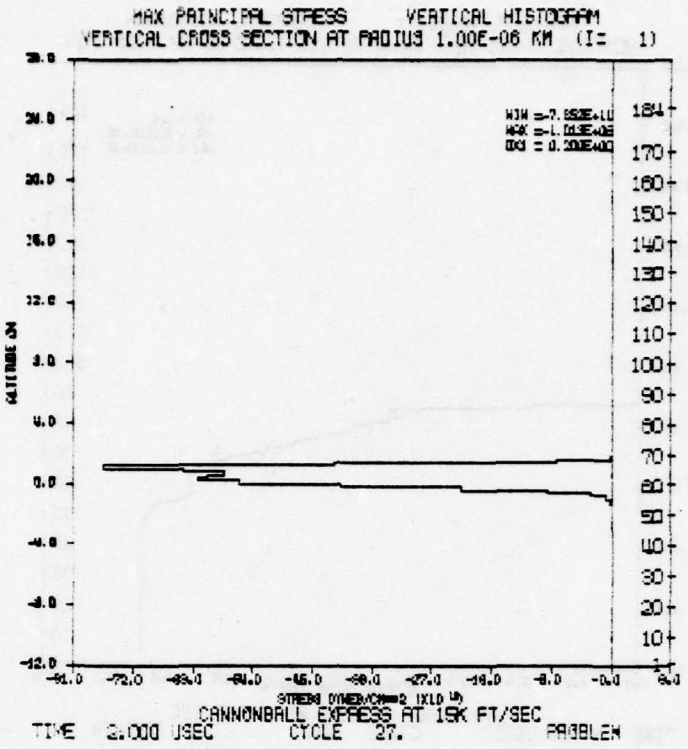

Figure 13. Stress Histogram at 2 μs

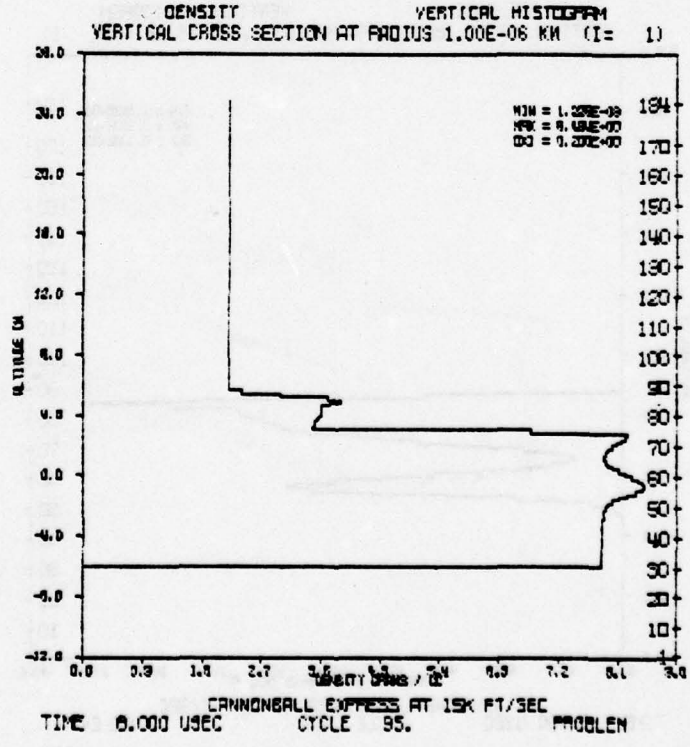

Figure 14. Density Histogram at 8 μs

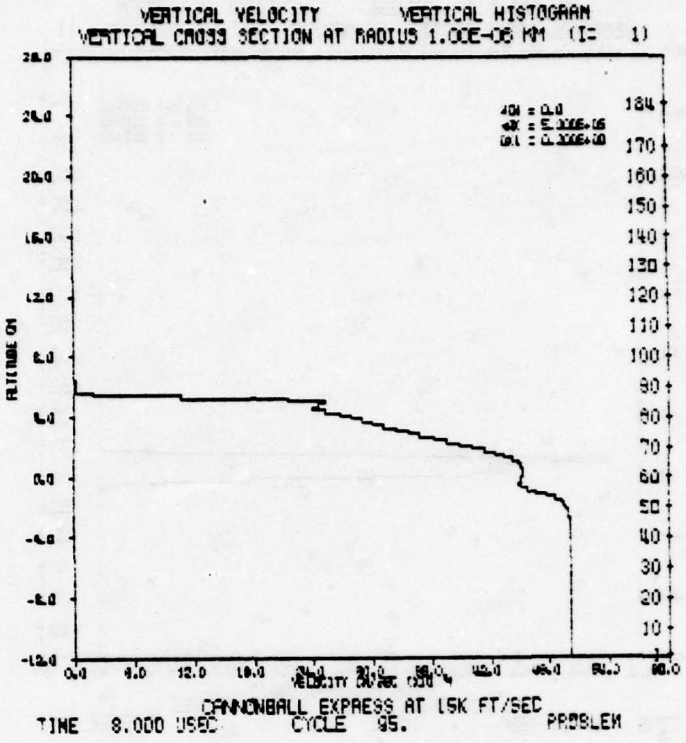

Figure 15. Vertical Velocity Histogram at 8 μs

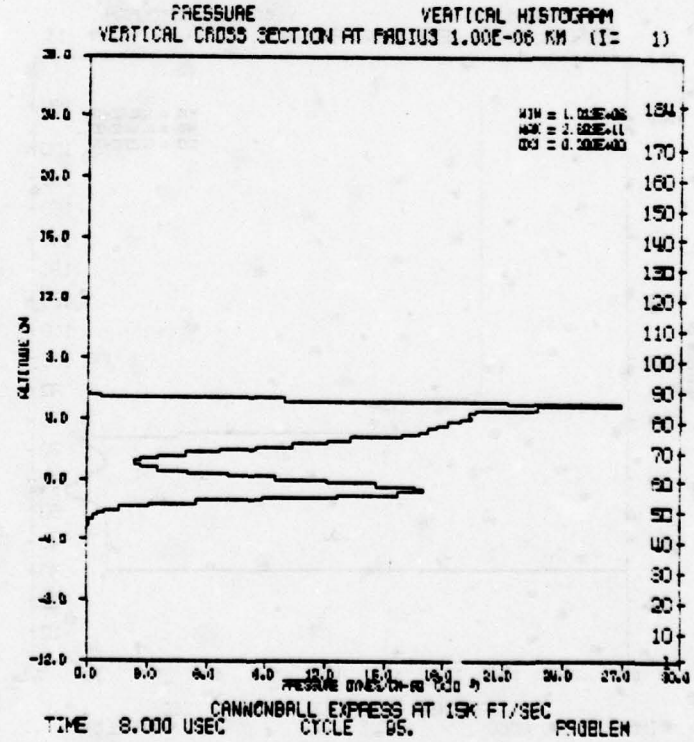

Figure 16. Pressure Histogram at 8 μs

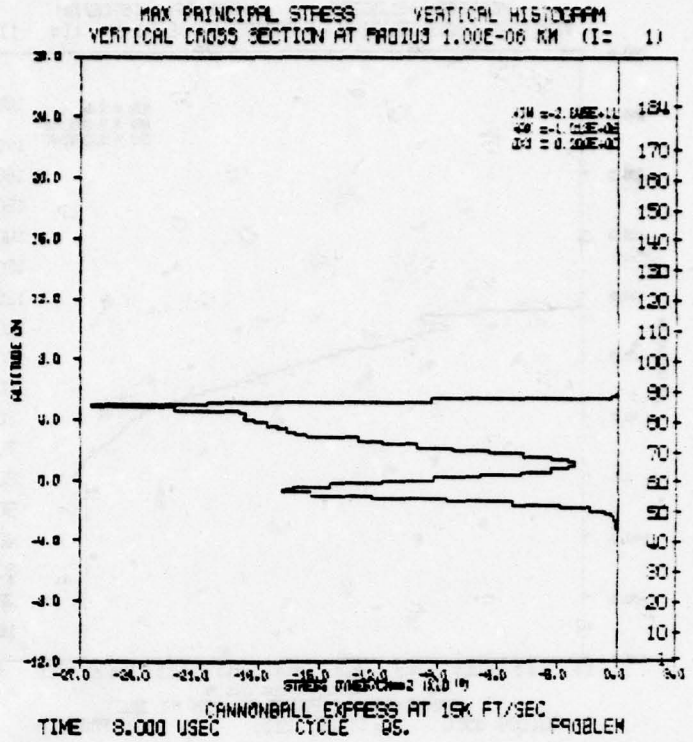

Figure 17. Stress Histogram at 8 μs

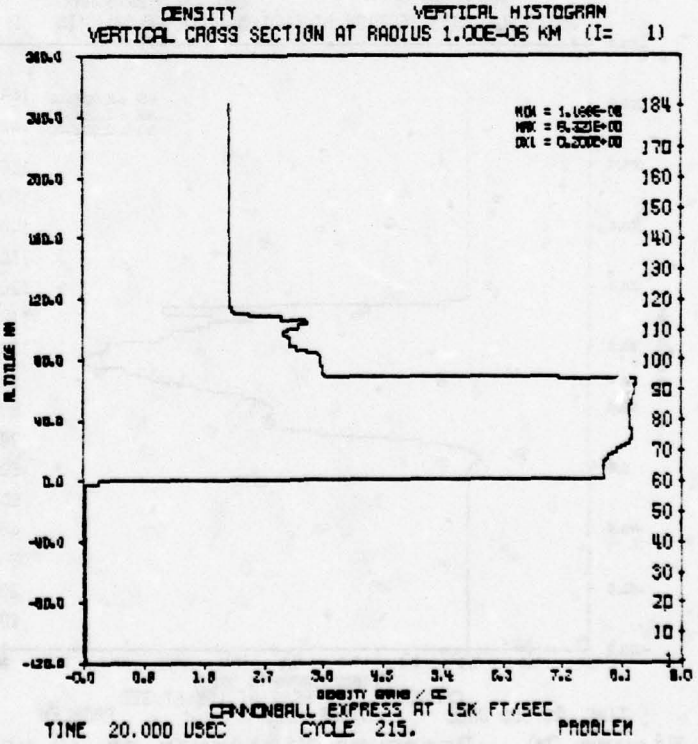

Figure 18. Density Histogram at 20 μs

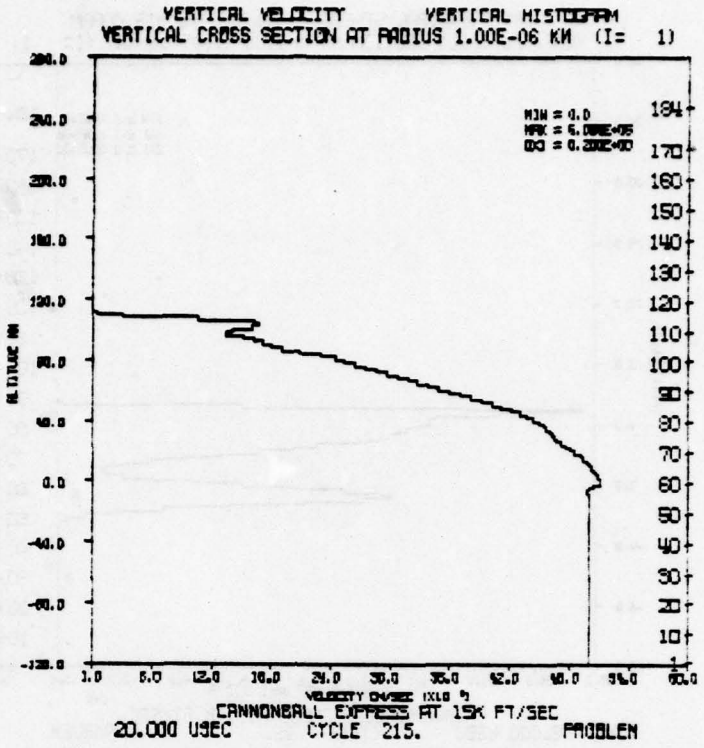

Figure 19. Vertical Velocity Histogram at 20 μs

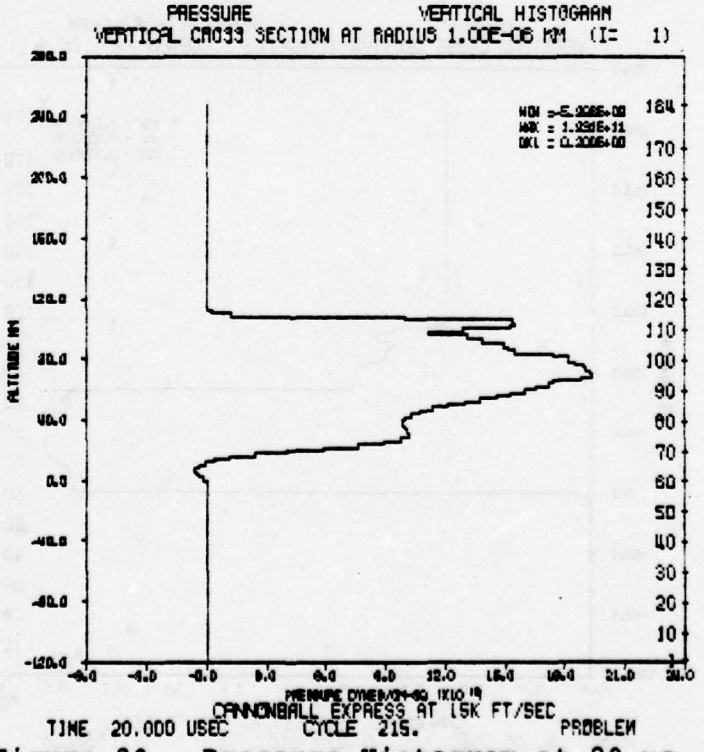

Figure 20. Pressure Histogram at 20 μs

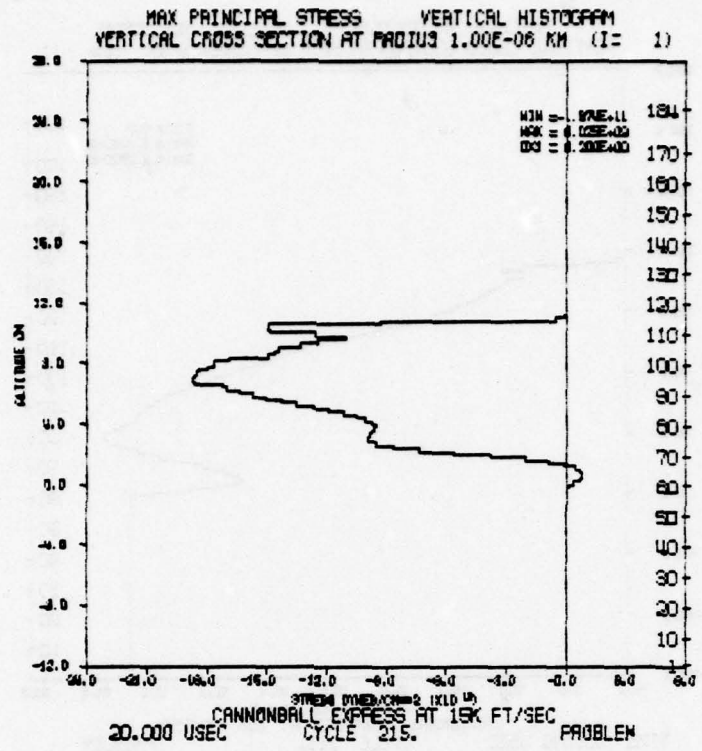

Figure 21. Stress Histogram at 20 µs

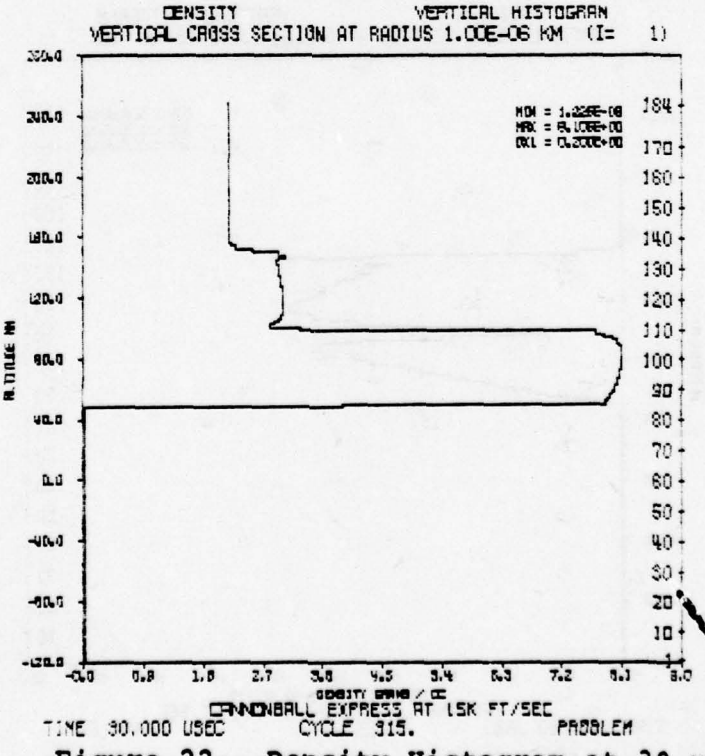

Figure 22. Density Histogram at 30 µs

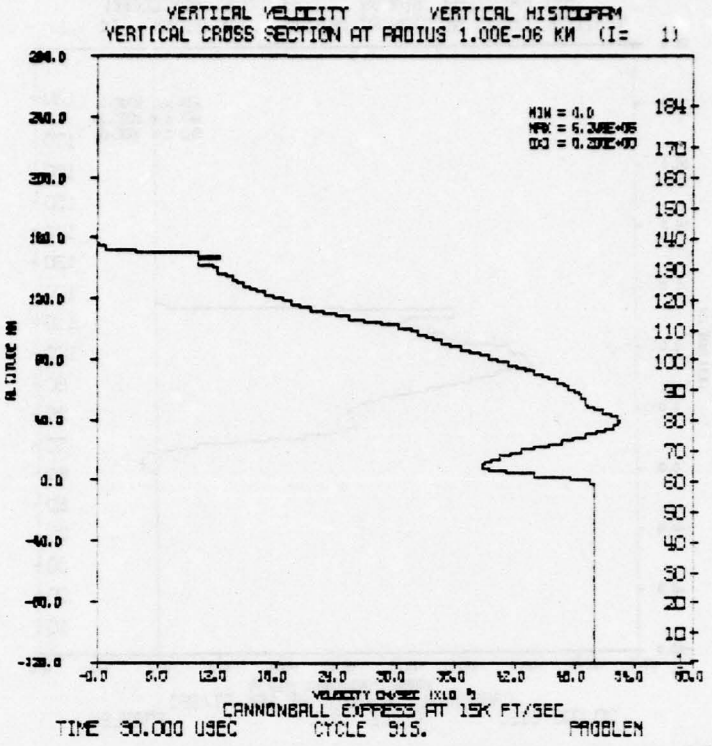

Figure 23. Vertical Velocity Histogram at 30 μs

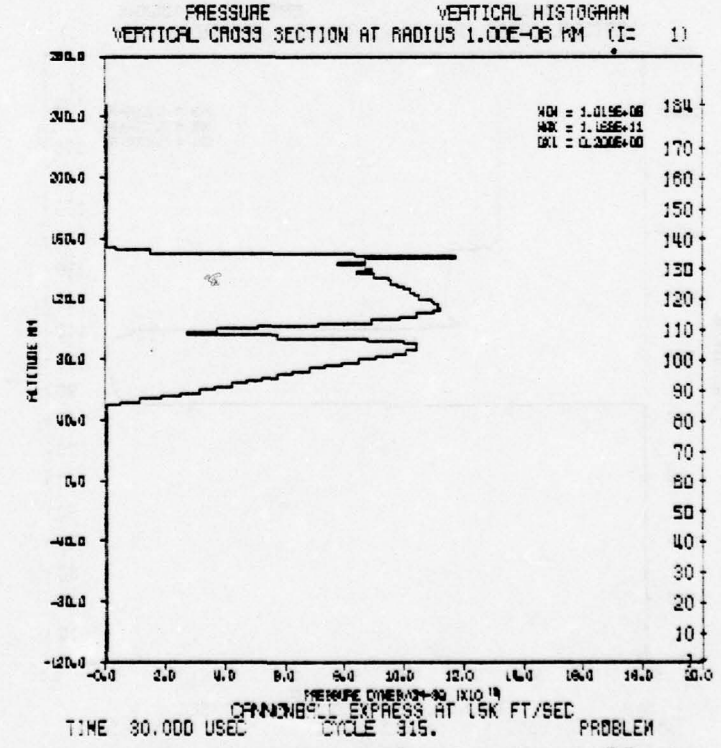

Figure 24. Pressure Histogram at 30 μs

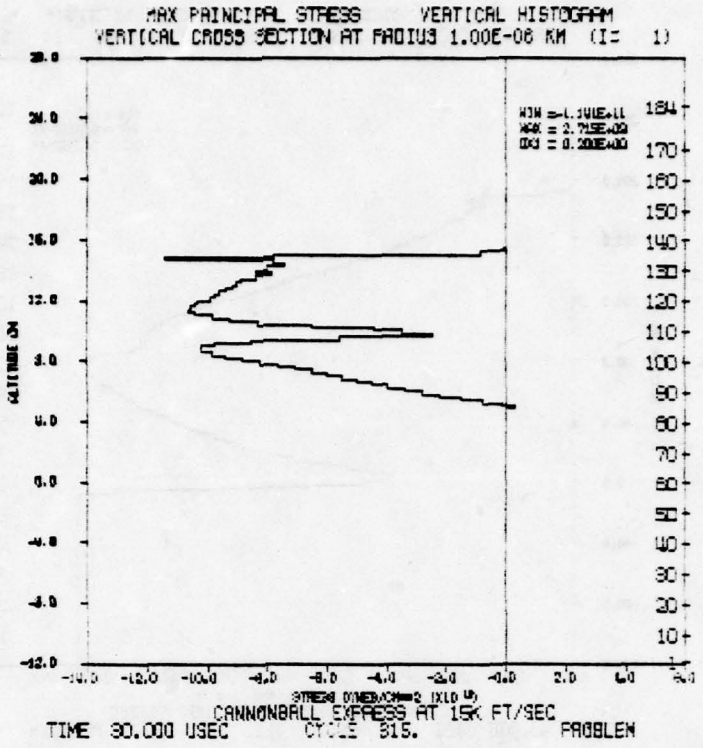

Figure 25. Stress Histogram at 30 µs

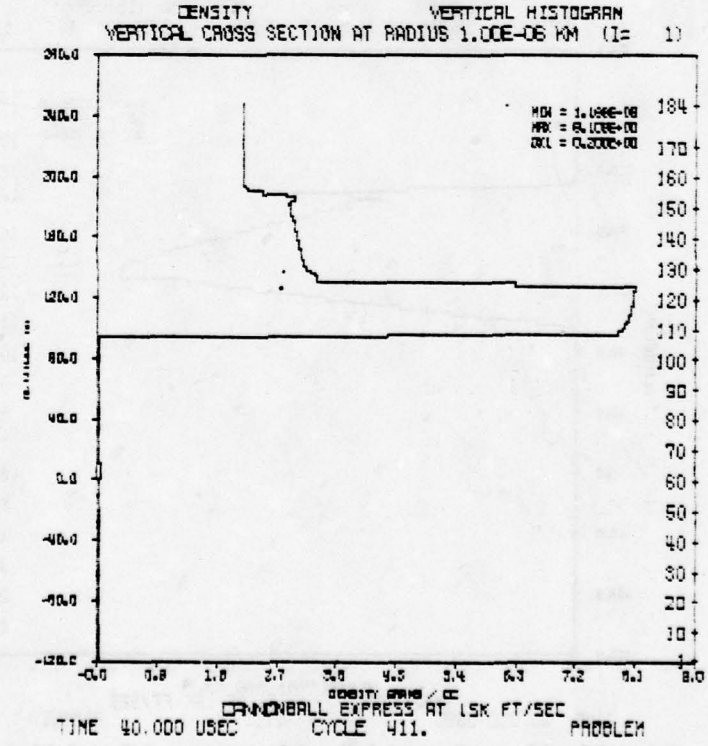

Figure 26. Density Histogram at 40 µs

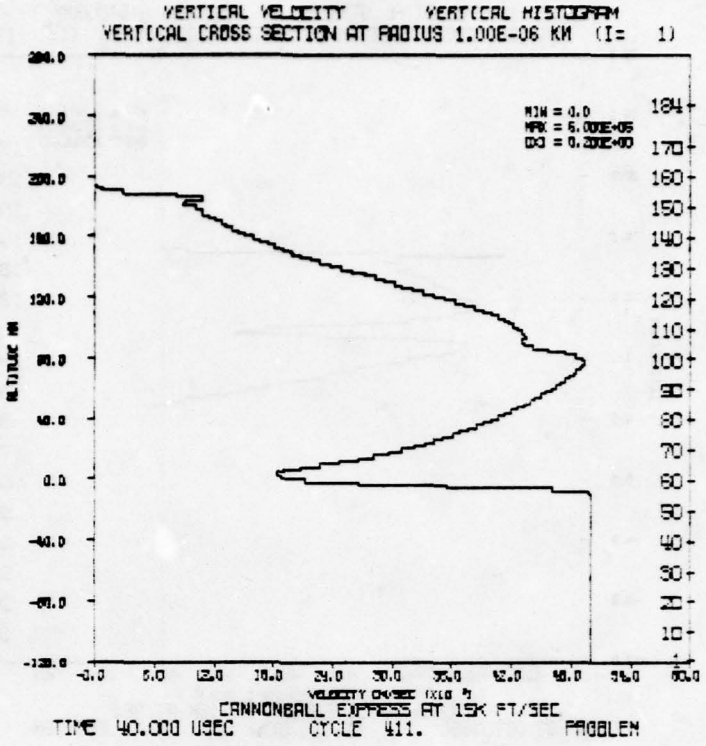

Figure 27. Vertical Velocity Histogram at 40 µs

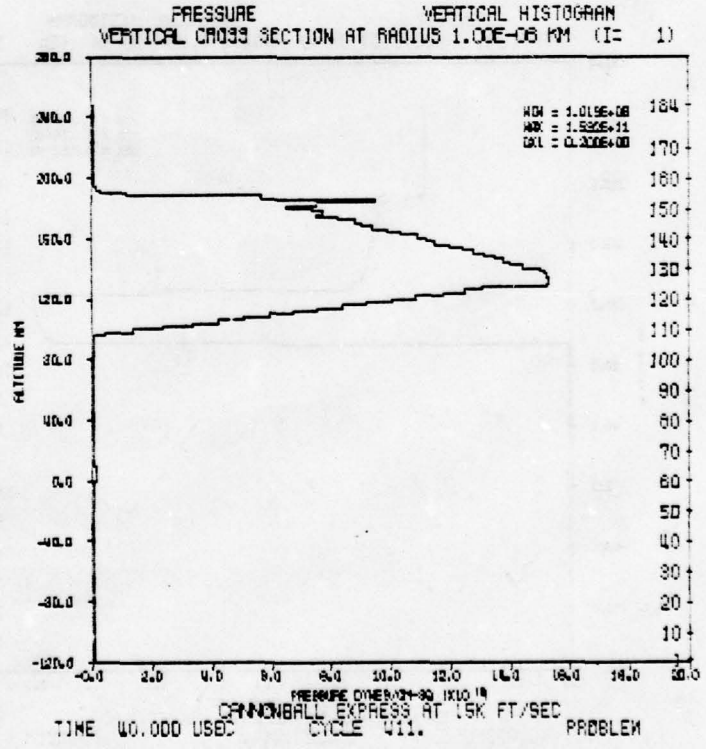

Figure 28. Pressure Histogram at 40 µs

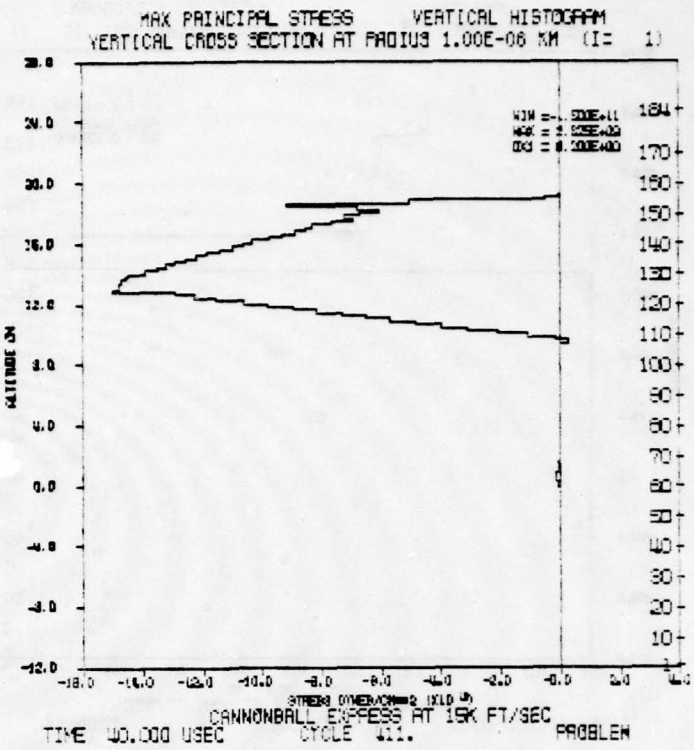

Figure 29. Stress Histogram at 40 μs

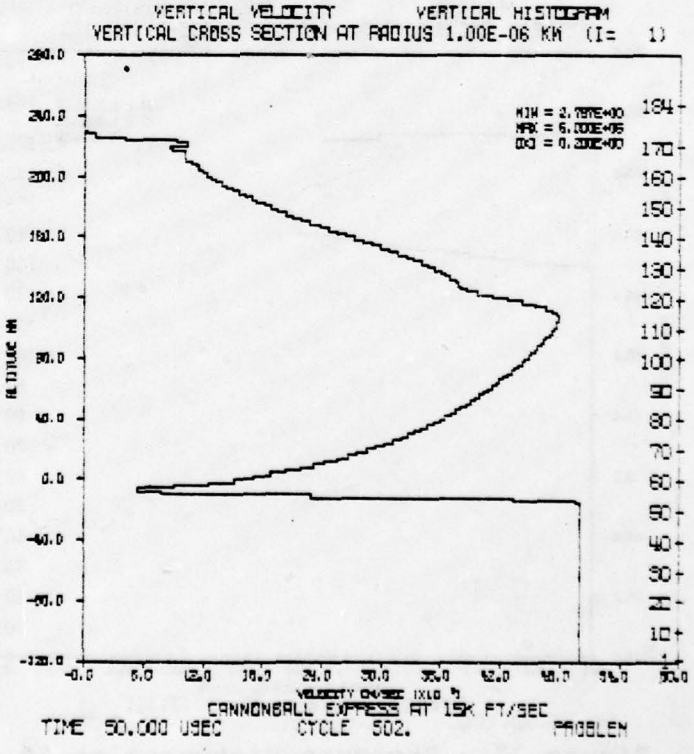

Figure 30. Vertical Velocity Histogram at 5 μs

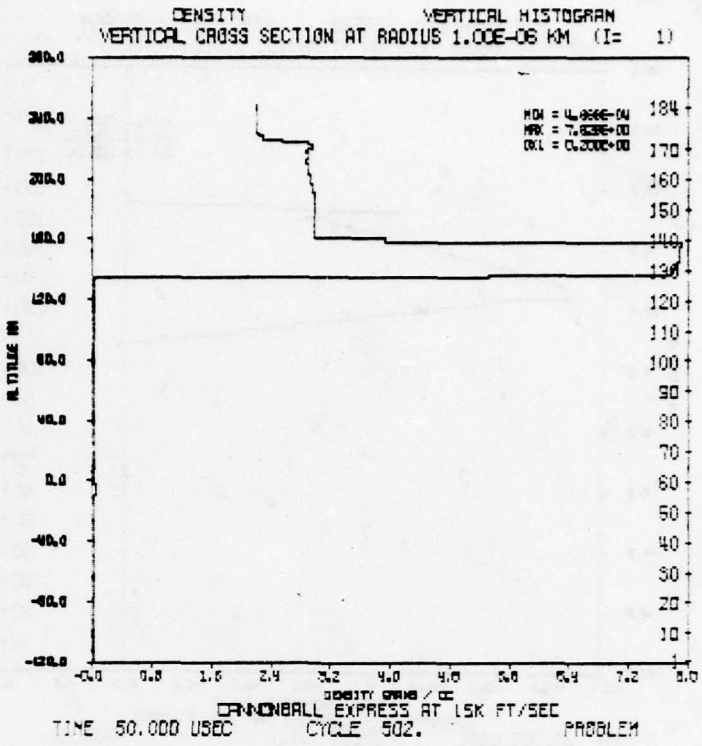

Figure 31. Density Histogram at 50 µs

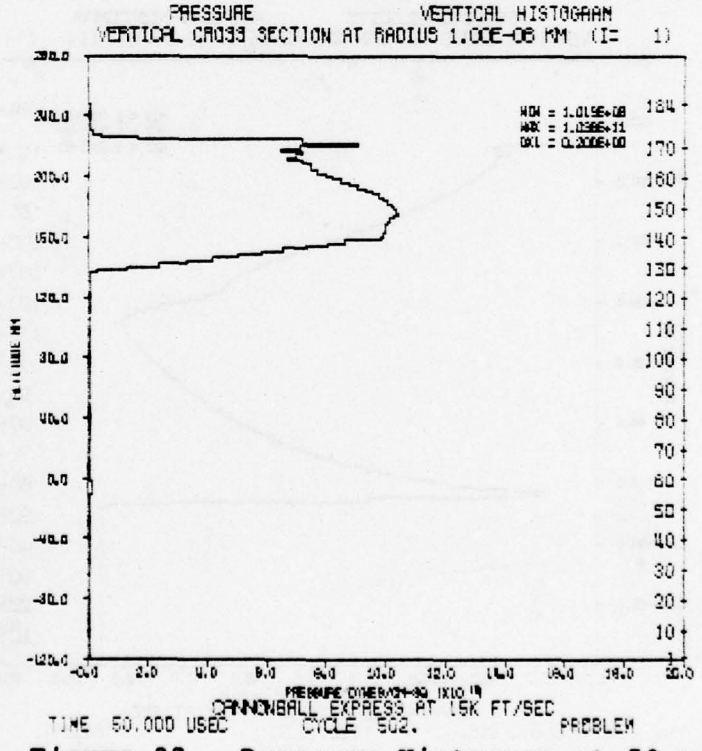

Figure 32. Pressure Histogram at 50 µs

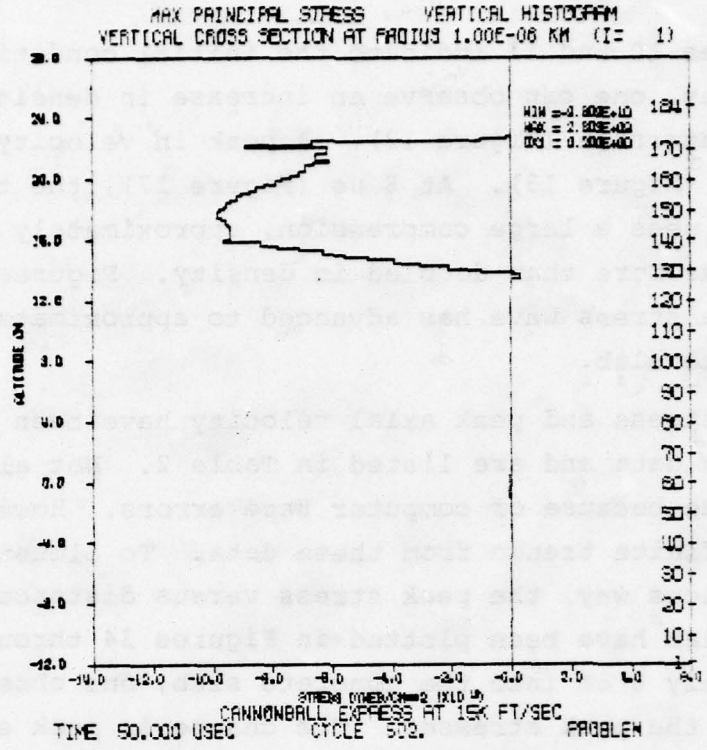

Figure 33. Stress Histogram at 50 µs

Figures 10 and 11 indicate the initial conditions. By the time of 2 μs, one can observe an increase in density at the steel concrete interface (Figure 12). A peak in velocity is also detectable (Figure 13). At 8 μs (Figure 17), the tip of the penetrator sees a large compression, approximately 25%, and the concrete has more than doubled in density. Figures 18 through 21 show the stress wave has advanced to approximately 11 cm into the concrete slab.

Peak stress and peak axial velocity have been obtained from the station data and are listed in Table 2. Not all of the data are complete because of computer tape errors. However, one can observe definite trends from these data. To illustrate this in a more obvious way, the peak stress versus distance into the concrete slab have been plotted in Figures 34 through 36. At approximately 6 cm into the concrete slab, one observes a leveling off of the peak stresses. The change in peak stress versus distance into the concrete slab roughly coincides with the length of the penetrator. In this case, with a length of 10 cm for the penetrator, a transition can be seen beginning at 6 cm and ending at about 10 cm.

In Figure 37, the material motion versus depth into the concrete has been plotted. Again, one can see the change in behavior at 6 cm for the 10,000 and 15,000 ft/s case. For the 25,000 ft/s penetrator, the effect is present but begins at about 10 cm depth.

Table 2. Summary of Steel Into Concrete Data

Station	25,000 ft/s		15,000 ft/s		10,000 ft/s	
	Peak Stress dynes/cm^2	Peak Velocity cm/s	Peak Stress	Peak Velocity	Peak Stress	Peak Velocity
1 cm	1.45×10^{12}	6.16×10^{5}	7.72×10^{11}	4.21×10^{5}	3.30×10^{11}	2.59×10^{5}
2 cm	1.45×10^{12}	6.15×10^{5}	7.26×10^{11}	4.14×10^{5}	2.96×10^{11}	2.50×10^{5}
3 cm	1.16×10^{12}	5.77×10^{5}	5.29×10^{11}	3.68×10^{5}	2.19×10^{11}	2.13×10^{5}
4 cm	8.27×10^{11}	4.91×10^{5}	3.57×10^{11}	3.00×10^{5}	1.70×10^{11}	1.80×10^{5}
6 cm	4.89×10^{11}	4.39×10^{5}	1.99×10^{11}	2.00×10^{5}	1.52×10^{11}	1.67×10^{5}
8 cm	3.82×10^{11}	4.22×10^{5}	1.54×10^{11}	1.80×10^{5}	2.00×10^{10}	6.00×10^{4}
10 cm	3.54×10^{11}	4.04×10^{5}	1.54×10^{11}	1.40×10^{5}	3.50×10^{10}	6.00×10^{4}
12 cm	3.51×10^{11}	2.00×10^{5}	1.53×10^{11}	1.20×10^{5}	3.00×10^{10}	5.00×10^{4}
14 cm	3.33×10^{11}	2.60×10^{5}	1.26×10^{11}	1.20×10^{5}	2.00×10^{10}	
16 cm	3.08×10^{11}	2.40×10^{5}	1.09×10^{11}		1.40×10^{10}	
18 cm	2.90×10^{11}	2.70×10^{5}	9.55×10^{10}		1.30×10^{10}	3.40×10^{4}
20 cm	2.70×10^{11}	2.47×10^{5}	8.50×10^{10}			
22 cm	2.48×10^{11}		8.40×10^{10}			
24 cm	2.17×10^{11}					

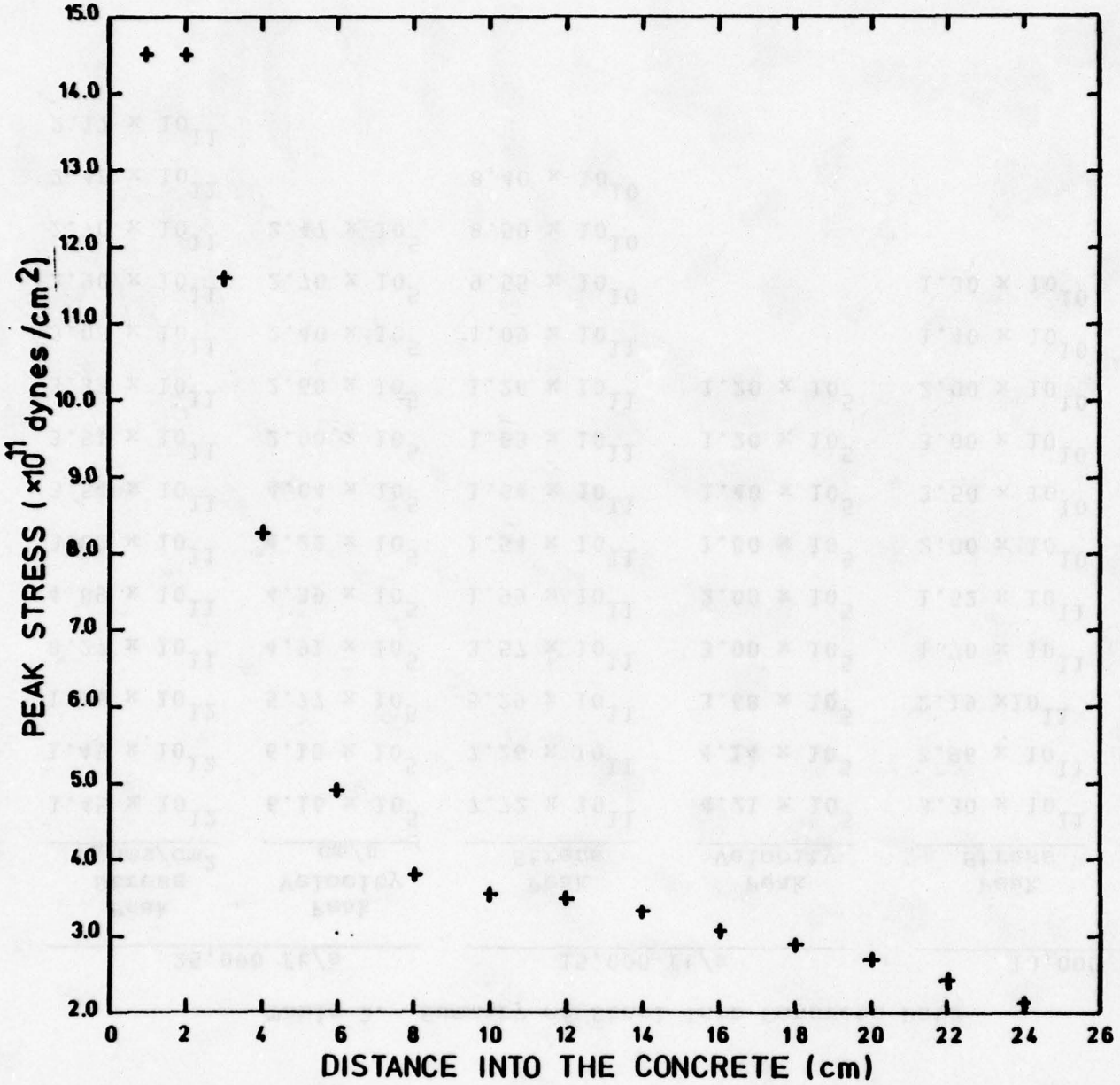

Figure 34. Peak Stress in Concrete (Penetrator Velocity = 25 kft/s)

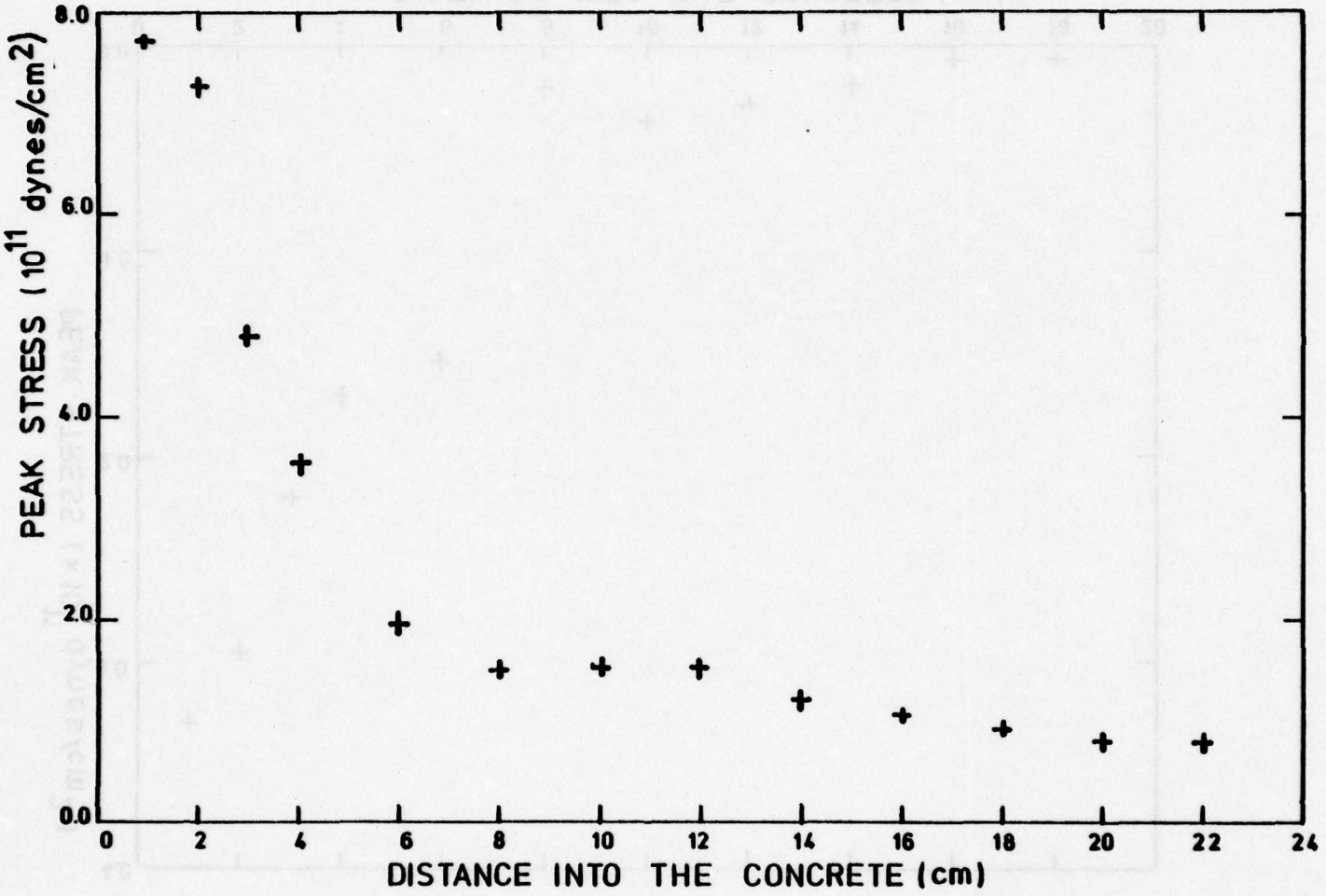

Figure 35. Peak Stress in Concrete (Penetrator Velocity = 15 kft/s)

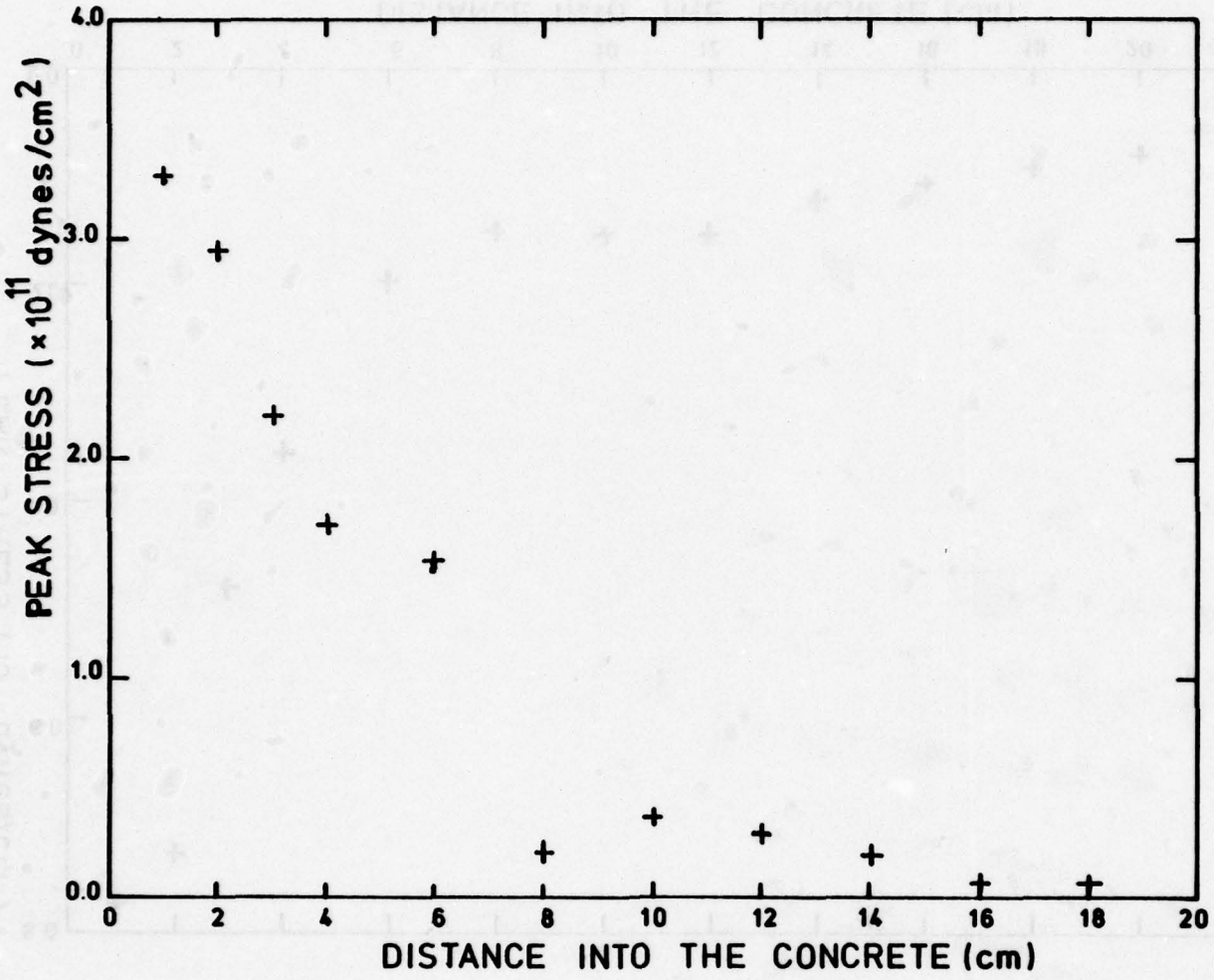

Figure 36. Peak Stress in Concrete (Penetrator Velocity = 10 kft/s)

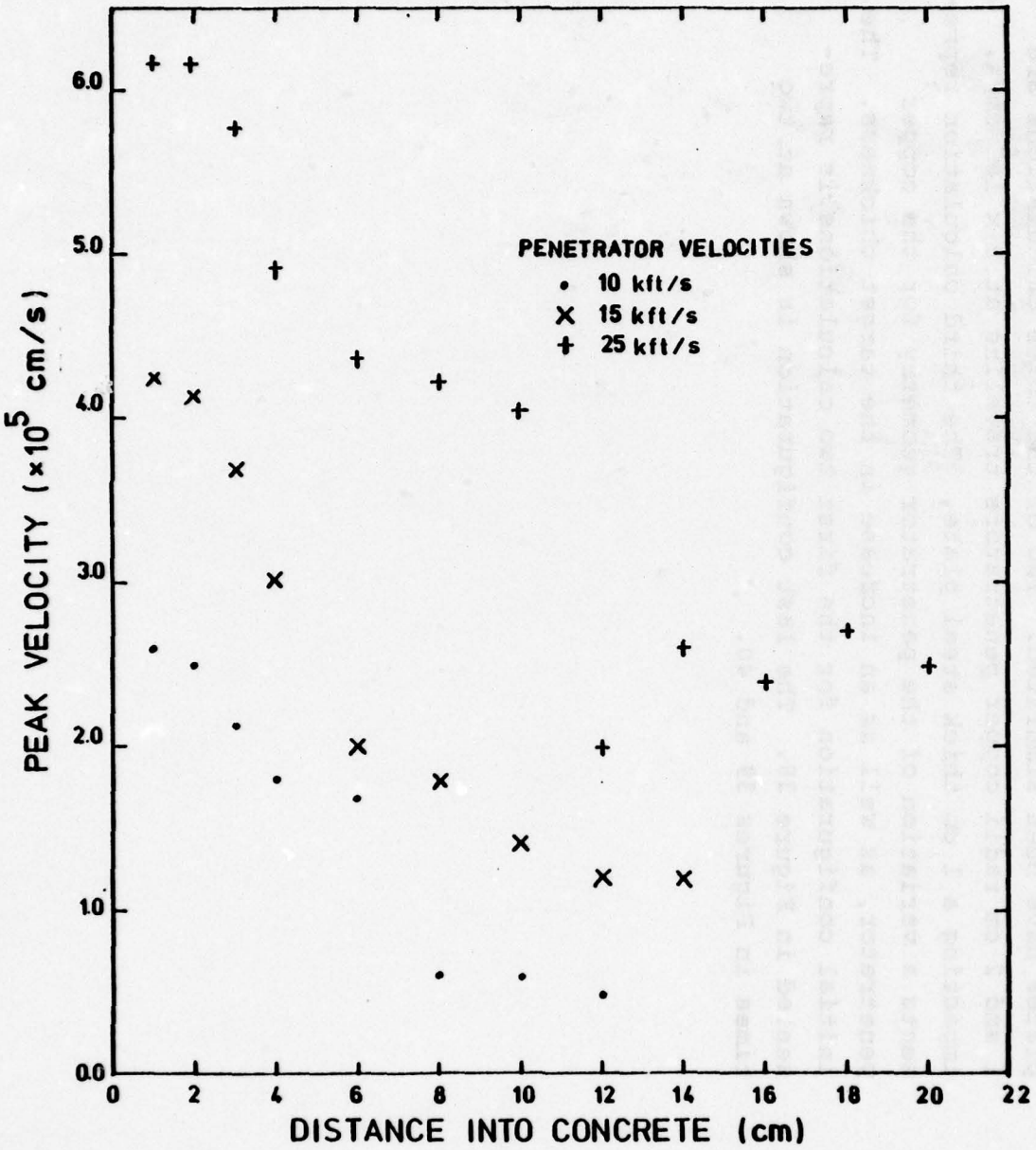

Figure 37. Maximum Material Motion in Concrete

SECTION IV

COPPER PENETRATORS INTO STEEL PLATES

Introduction

Several penetration events involving copper into steel plates have been simulated. Two of the three calculations are 1 and 2 cm radii copper penetrators traveling at 3×10^5 cm/s, impacting a 1 cm thick steel plate. The third calculation represents a variation of the penetrator geometry for the copper penetrator, as well as an increase in the target thickness. The initial configuration for the first two calculations is represented in Figure 38. The last configuration is shown at two times in Figures 39 and 40.

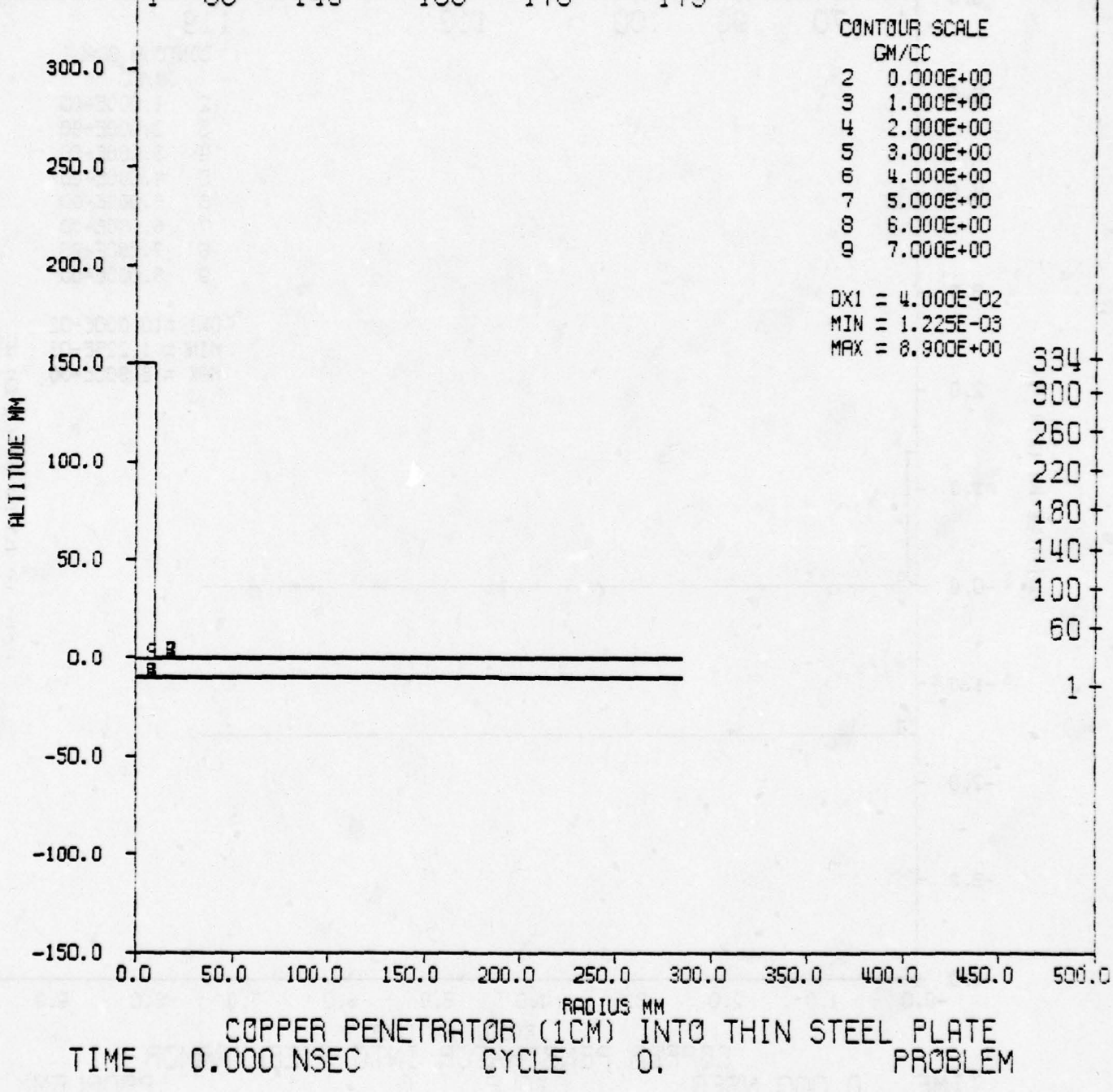

Figure 38. Initial Density Configuration for Thin Plate Calculations

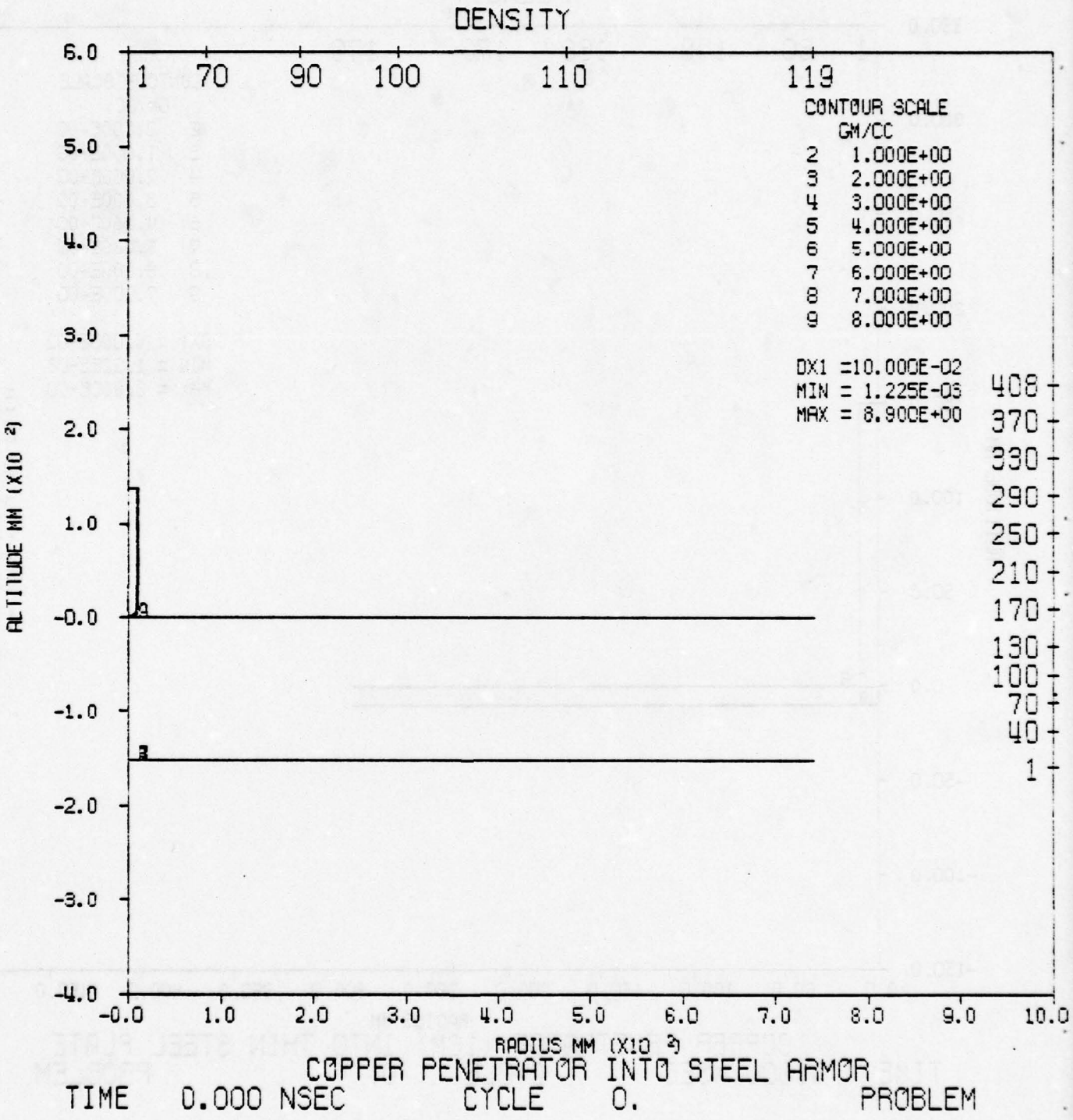

Figure 39. Initial Density Configuration for Thick Plate Calculations

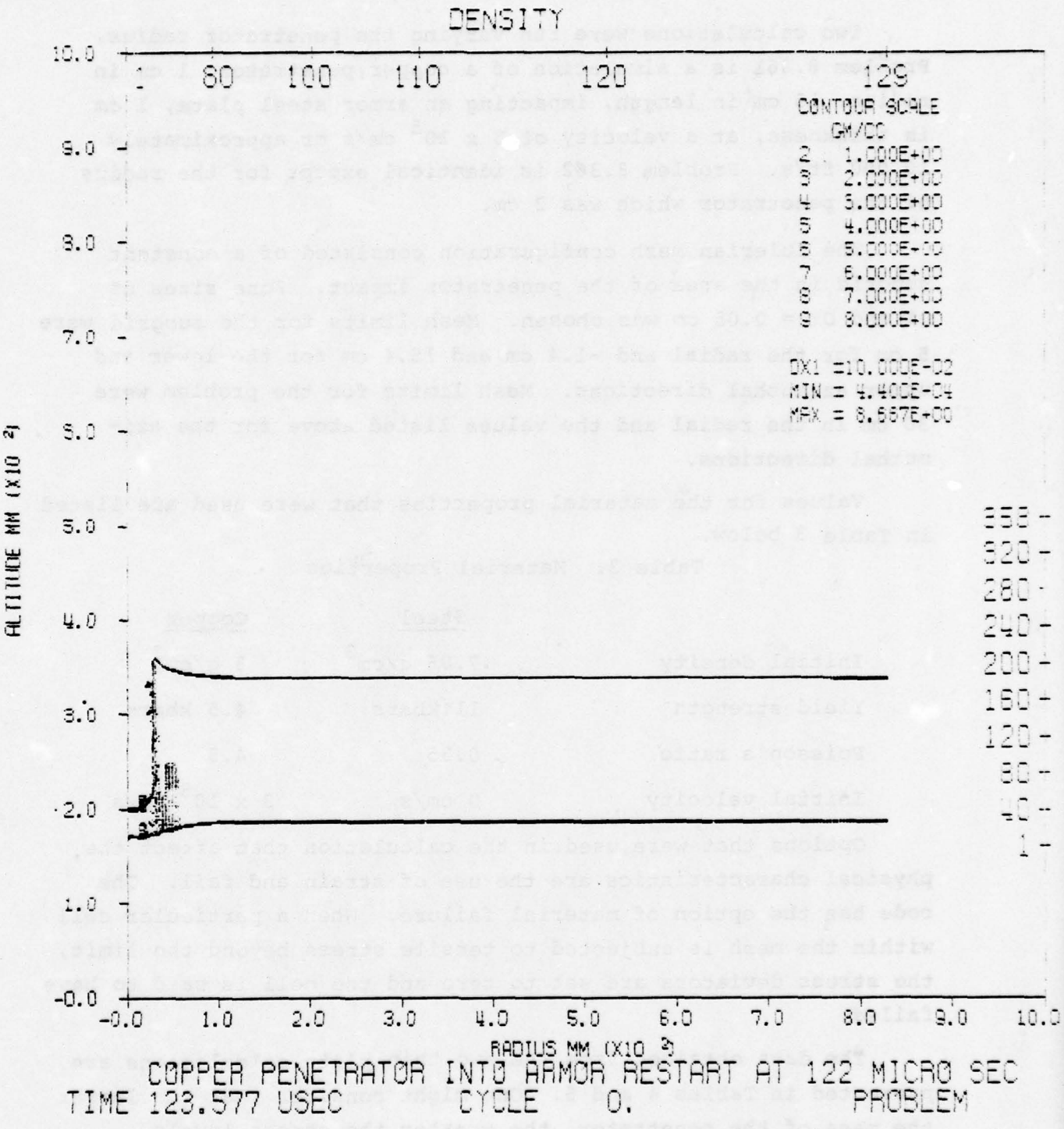

Figure 40. Initial Configuration for Thick Plate Restart

Thin Plate Calculations

Two calculations were run varying the penetrator radius. Problem 8.361 is a simulation of a copper penetrator, 1 cm in radius, 15 cm in length, impacting an armor steel plate, 1 cm in thickness, at a velocity of 3×10^5 cm/s or approximately 10,000 ft/s. Problem 8.362 is identical except for the radius of the penetrator which was 2 cm.

The Eulerian mesh configuration consisted of a constant subgrid in the area of the penetrator impact. Zone sizes of DX and DY = 0.05 cm was chosen. Mesh limits for the subgrid were 5 cm for the radial and -1.4 cm and 15.4 cm for the lower and upper azimuthal directions. Mesh limits for the problem were 30 cm in the radial and the values listed above for the azimuthal directions.

Values for the material properties that were used are listed in Table 3 below.

Table 3. Material Properties

	Steel	Copper
Initial density	7.86 g/cm^3	8 g/cm^3
Yield strength	11 kbars	4.5 kbars
Poisson's ratio	0.35	4.5
Initial velocity	0 cm/s	3×10^5 cm/s

Options that were used in the calculation that affect the physical characteristics are the use of strain and fail. The code has the option of material failure. When a particular cell within the mesh is subjected to tensile stress beyond the limit, the stress deviators are set to zero and the cell is said to have failed.

The data obtained from the two thin plate calculations are presented in Tables 4 and 5. One might consider that the larger the mass of the penetrator, the greater the stress levels.

Table 4. Thin Plate Summary (1 cm)

Distance from Penetrator Impact (cm)	Pressure (dynes/cm^2)	Velocity (cm/s)
INSIDE PENETRATOR		
1	9.23×10^{11}	1.65×10^{5}
2	3.71×10^{11}	8.61×10^{4}
3	1.53×10^{11}	4.06×10^{4}
4	6.43×10^{10}	1.87×10^{4}
6	4.82×10^{9}	1.84×10^{3}
INSIDE TARGET		
0	1.17×10^{12}	
-0.25	9.06×10^{11}	1.3×10^{5}
-0.5	8.76×10^{11}	1.1×10^{5}
-0.75	8.79×10^{11}	9.0×10^{4}
-1	2.26×10^{11}	1.15×10^{4}

Table 5. Thin Plate Summary (2 cm)

INSIDE PENETRATOR

Distance from Penetrator Target Interface (cm)	Pressure (dynes/cm^2)	Velocity (cm/s)
1	9.89×10^{11}	1.71×10^5
2	9.66×10^{11}	1.70×10^5
3	7.5×10^{11}	1.42×10^5
4	4.4×10^{11}	9.6×10^4

INSIDE TARGET

0	1.17×10^{12}
-.25	9.10×10^{11}
-.5	8.75×10^{11}
-.75	8.84×10^{11}
-1	2.43×10^{11}

However, as pointed out by Westmoreland and Day (Ref. 4), momentum must be conserved across the discontinuity of target and penetrators.

$$\phi = \rho D u$$

where D is the shock velocity,
ϕ the density,
and u is the particle velocity.

At initial impact, the particle velocity becomes the impact speed of the projectile. The above relation indicates that the mass of the penetrator does not initially play a role.

By examining Tables 4 and 5 closely, it can be seen that at zero distance inside the penetrator (at the target-penetrator interface), the resultant peak stresses are exactly identical. Proceeding away from the interface, the phenomenology follows a surface area effect. The peak stresses running back through the target are very much similar. Both the 1 and 2 cm radii penetrators have experienced the same peak at their interface with the target. That stress energy is propagated back along the length in essentially a one-dimensional fashion. However, inside the penetrator, the two cases do not agree at equal distances from impact point. What one sees here are edge effects from the outer radius of the penetrator. Some type of scaling should be in order, and this will be addressed in Section VI.

In Figures 41 through 44, the data found in Tables 4 and 5 have been plotted. The peak stress data are plotted for either side of the penetrator-target interface. Comparison of Figures 41 and 42 shows a dramatic difference in the behavior of the stress wave as it propagates through the penetrator. The larger

---

4. Westmoreland, C., and W. Day, Antiarmor Penetration Analysis, "Thermal Softening Effects," AFATL TR-77-18, Vol. II, p. 6, Air Force Armament Laboratory, Eglin AFB, Fl., 1977.

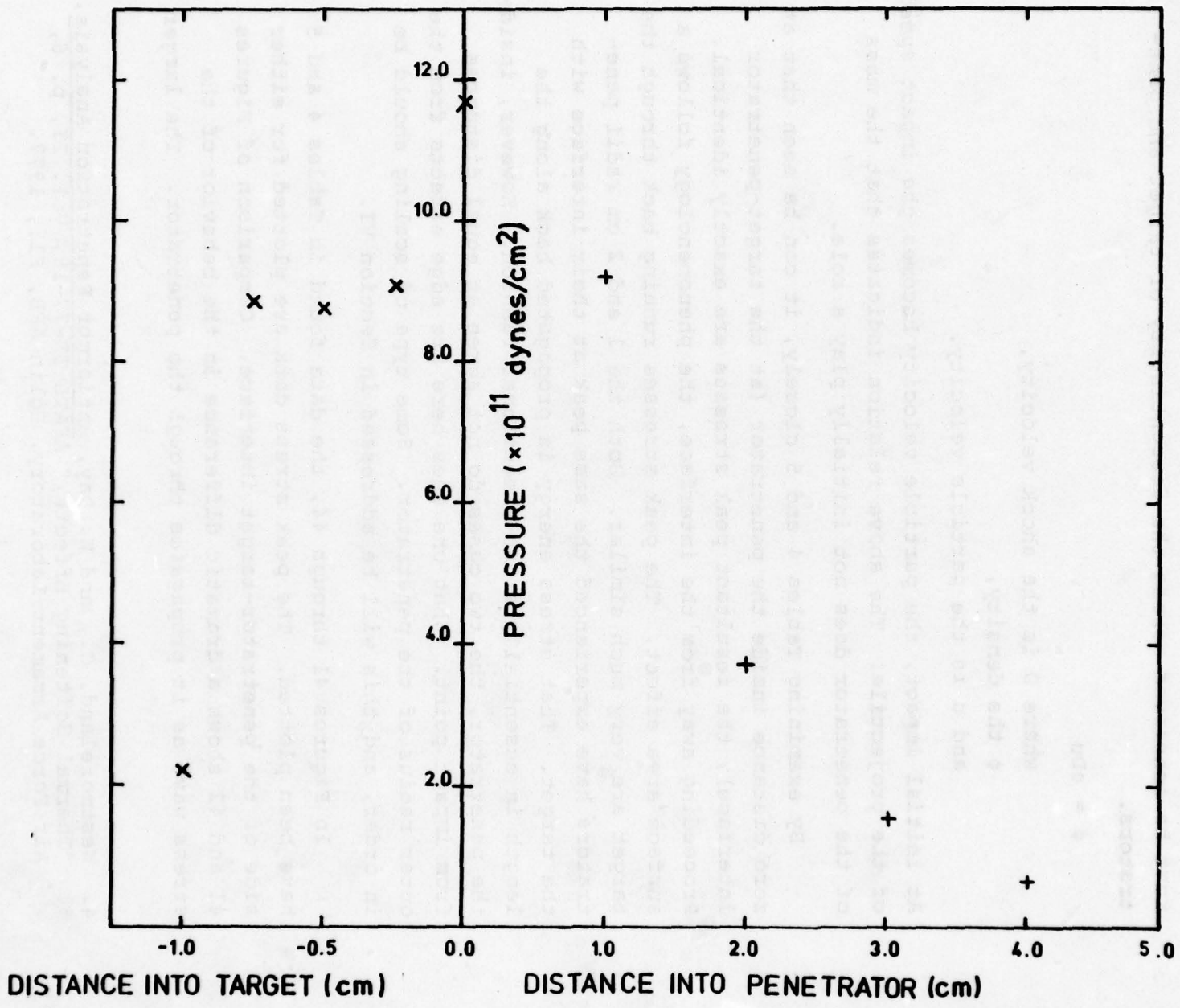

Figure 41. 1 cm Thin Plate Maximum Pressure

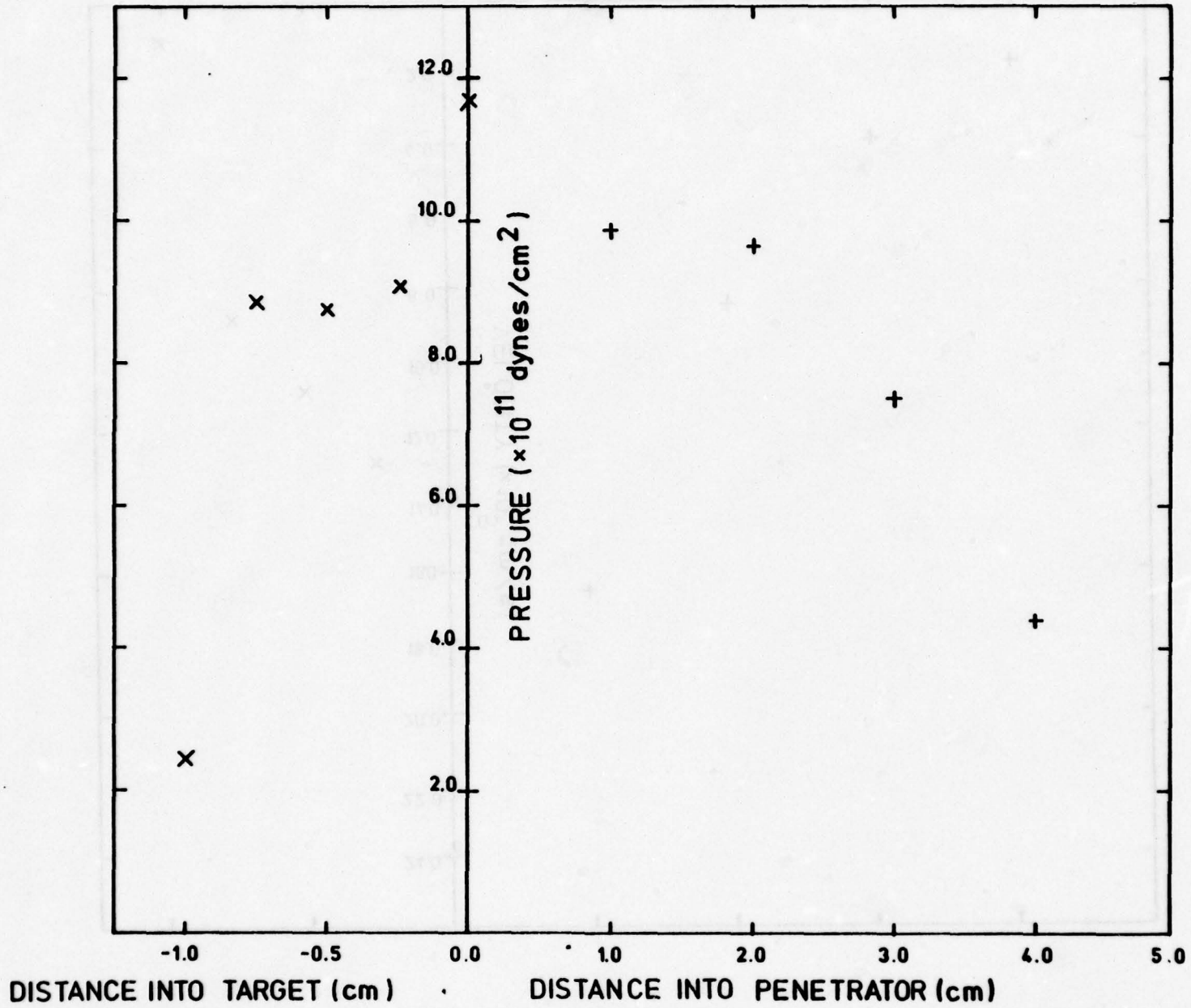

Figure 42. 2 cm Thin Plate Maximum Pressure

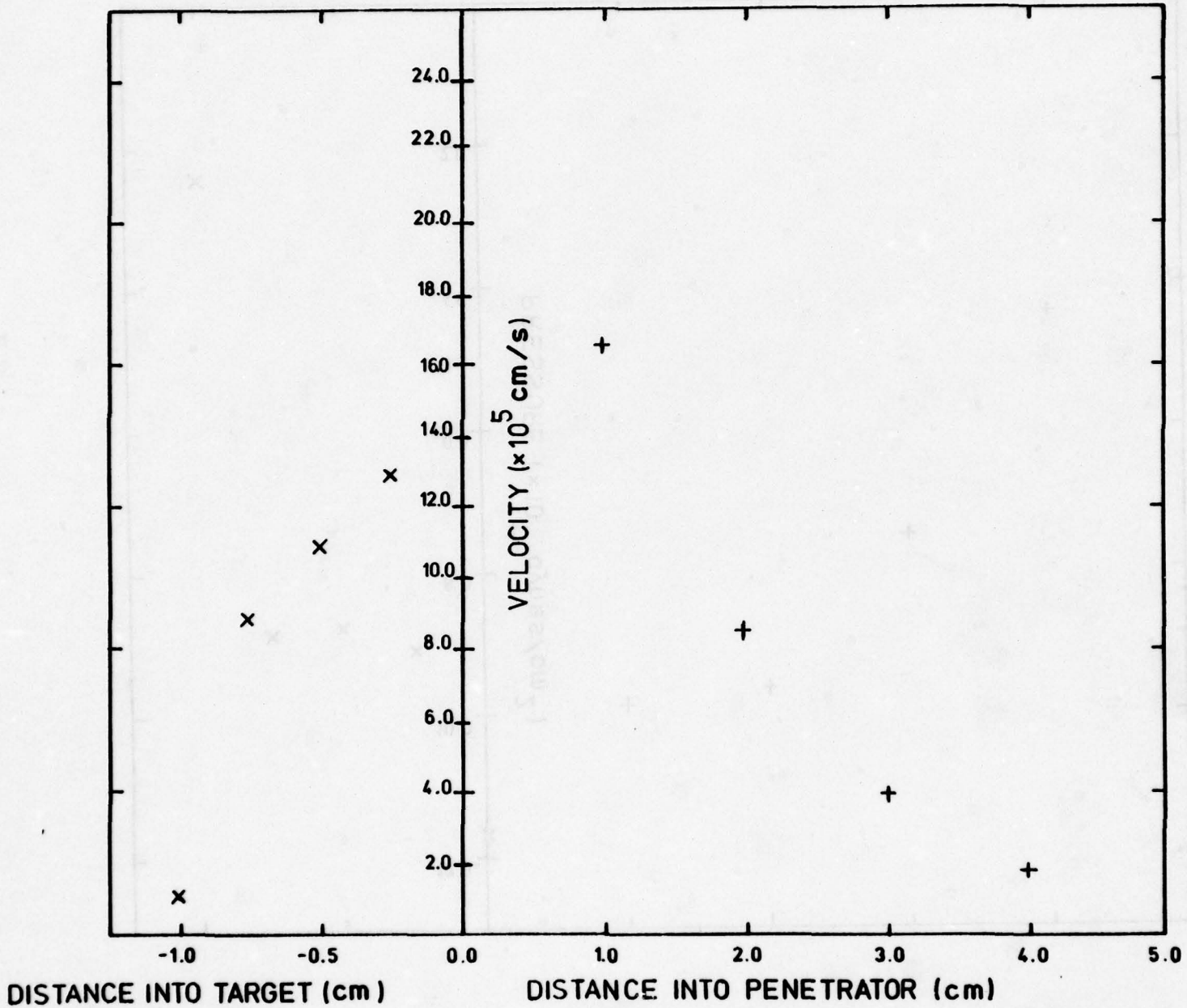

Figure 43. 1 cm Thin Plate Maximum Velocity

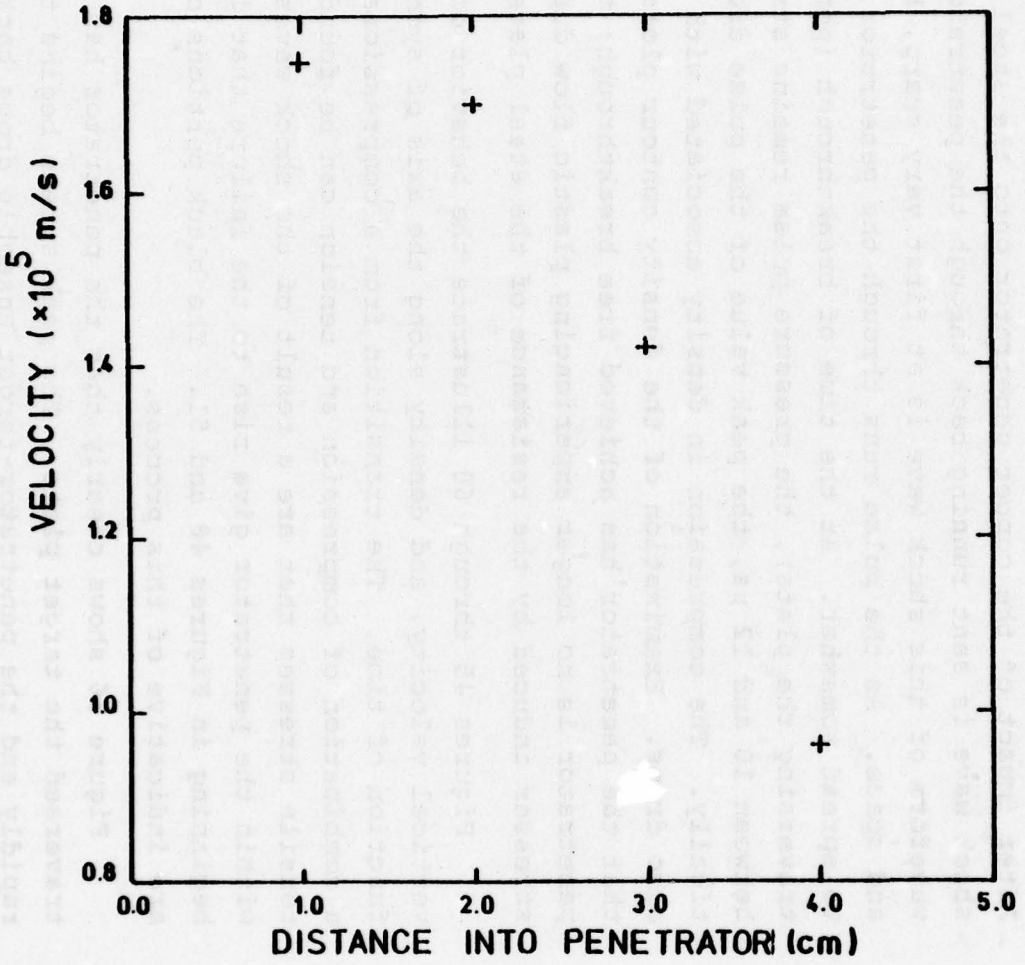

Figure 44. 2 cm Thin Plate Maximum Velocity

diameter penetrator exhibits a plateau effect between 1 and 2 cm from the interface. The plots of the maximum velocity also reflect this behavior. The data for maximum velocity inside the target were not available for the 2 cm radius case.

By next examining the calculations in more detail, one can try to characterize the time dependence of the phenomenology. After impact of the copper penetrator onto the steel plate, a shock wave is sent running back through the penetrator. The waveform of this shock wave is at first very sharp, both in time and space. As the pulse runs through the penetrator, it begins to spread somewhat. At the time of breakthrough (penetrator traversing the plate), the pressure pulse remains strong, but between 10 and 12 μs, the peak value of the pulse drops dramatically. The compression in density associated with this pulse also drops. Examination of the density contour plots indicates that the penetrator has achieved free breakthrough; that is, the penetrator is no longer experiencing plastic flow due to high stresses induced by the resistance of the steel plate.

Figures 45 through 60 illustrate the behavior of pressure, vertical velocity, and density along the axis of symmetry as a function of time. The transition from a compressional state to a combination of compression and tension can be found. These tensile stresses that are a result of the shock waves interacting within the penetrator give rise to the failure that is seen beginning in Figures 48 and 51. The black portions of Figure 48 are indicative of this process.

Figure 56 shows clearly that the penetrator has completely traversed the target plate. The peak stress begins to drop rapidly and the penetrator-target ensemble drops back into an elastic region.

The shape of the pulse is characteristically simple. Because the penetrator experiences resistance for only a short time due to the small thickness of the plate, the stress pulse

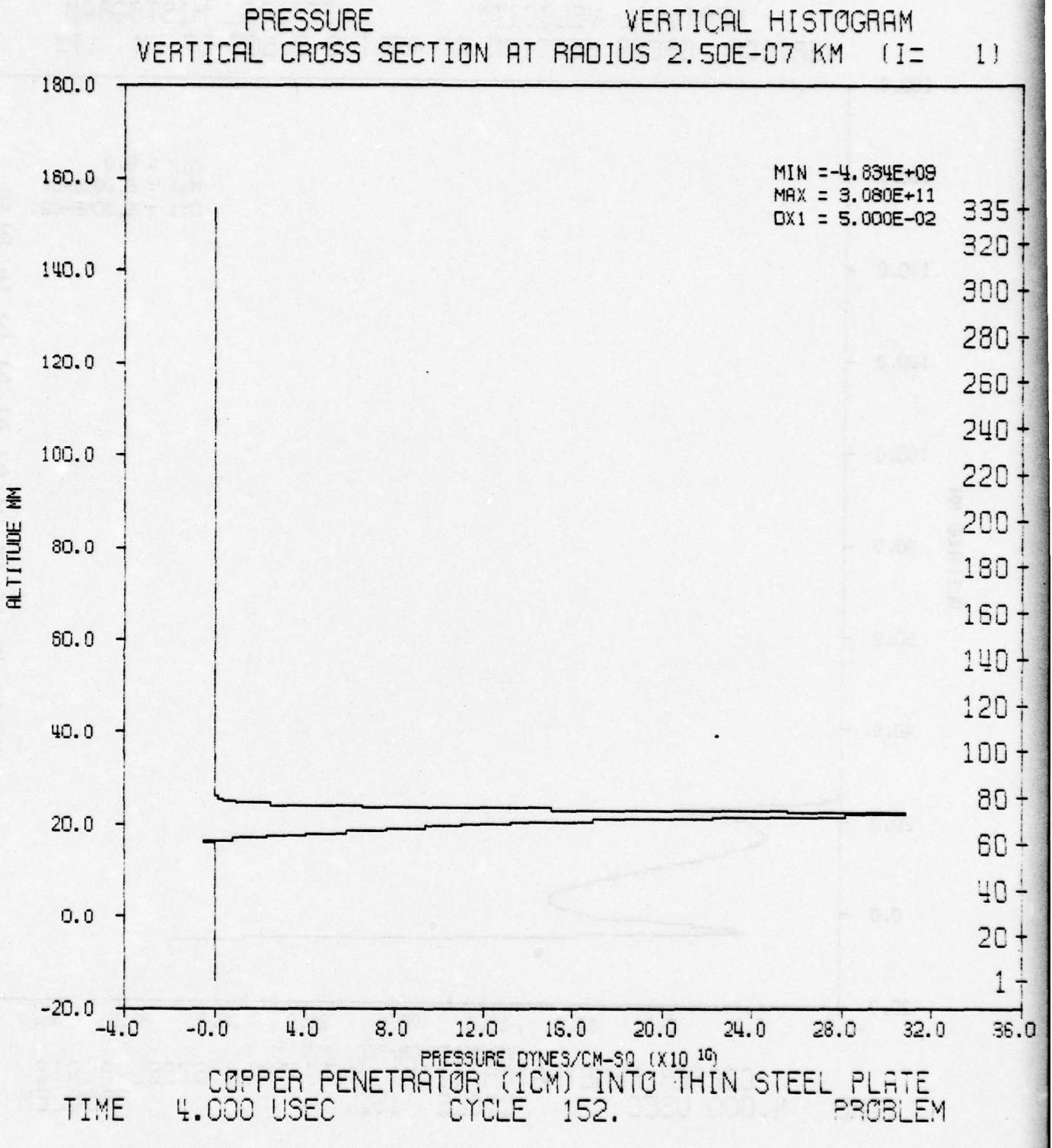

Figure 45. Pressure Histogram at 4.0 μs

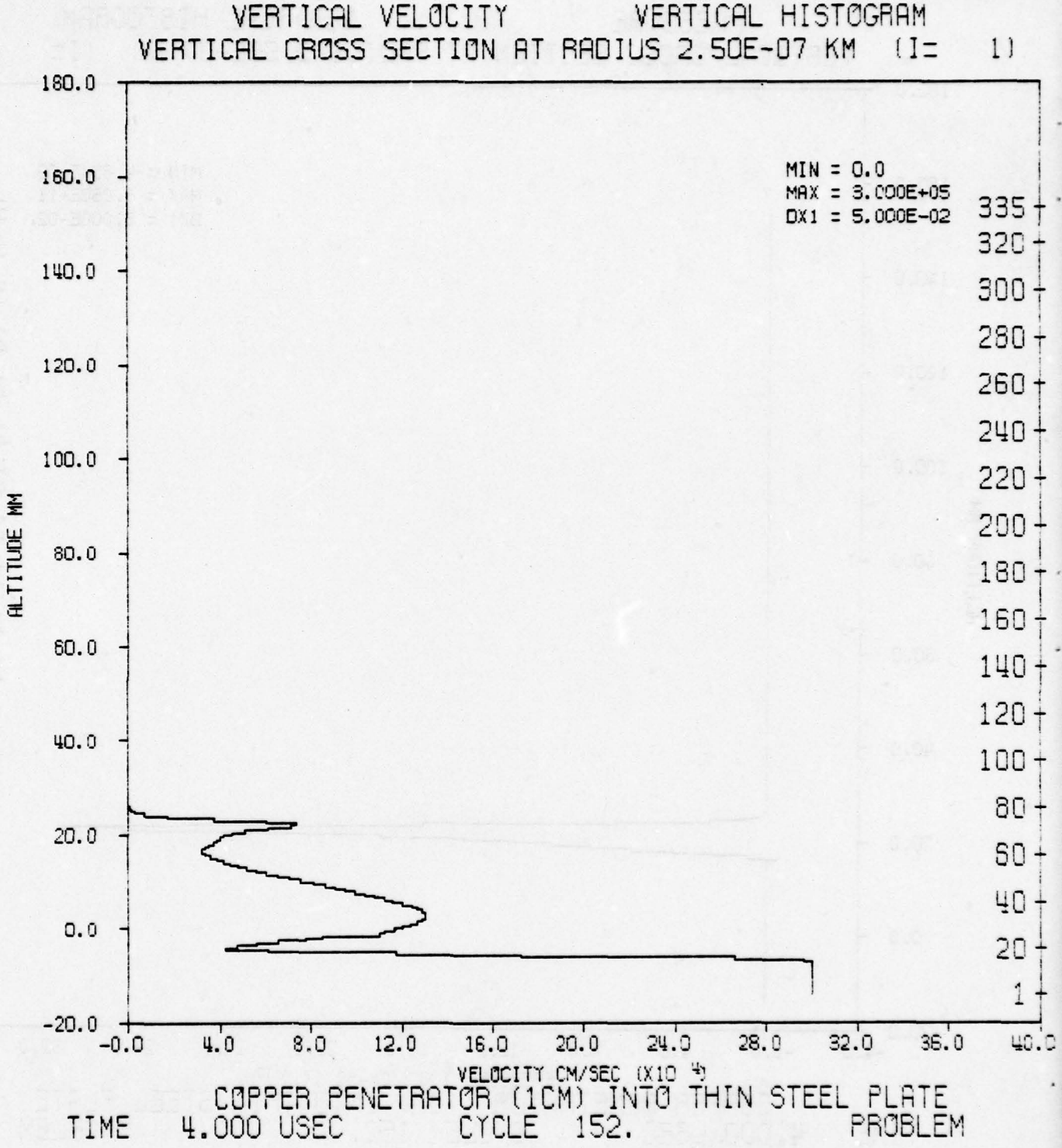

Figure 46. Vertical Velocity Histogram at 4.0 µs

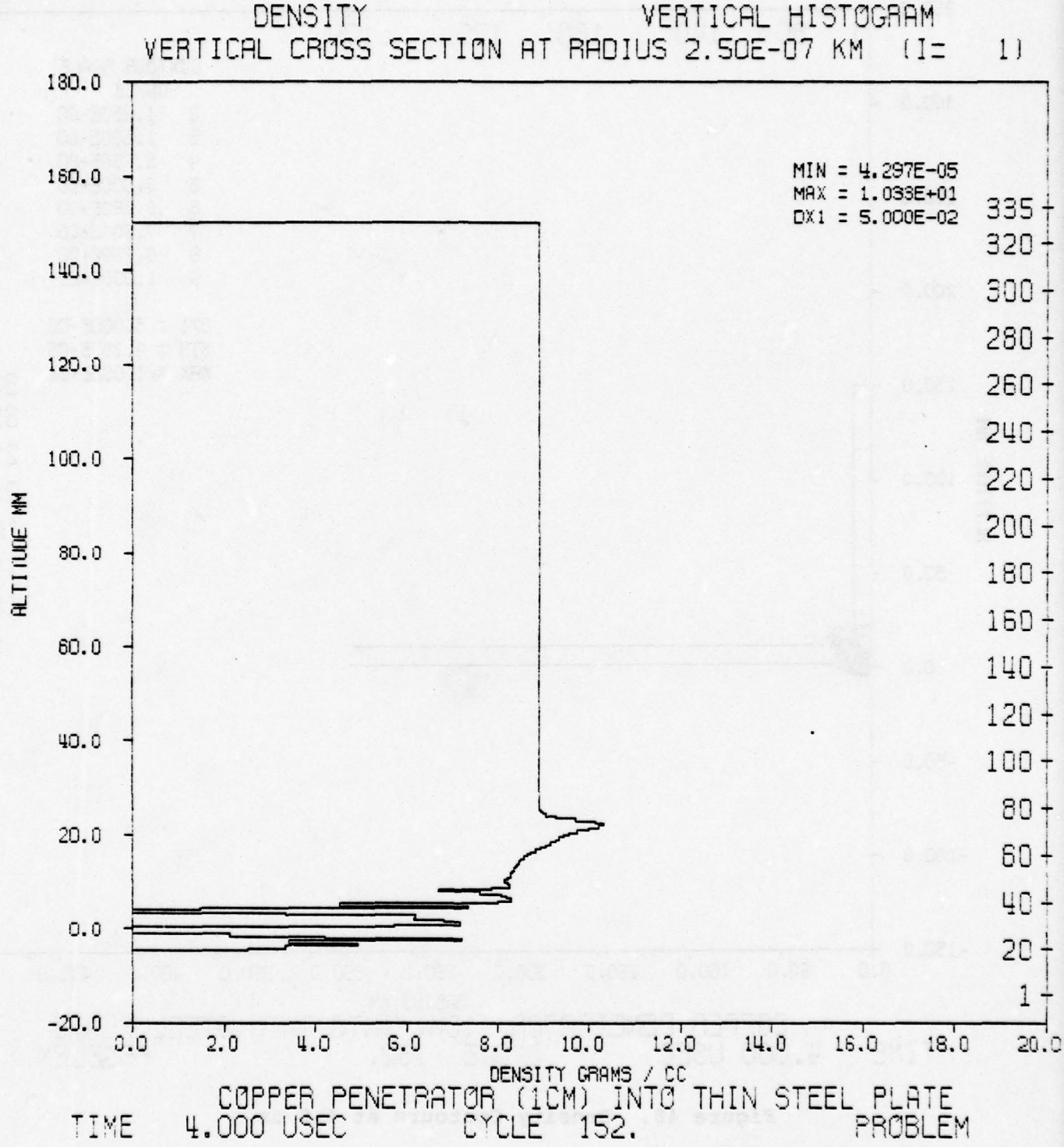

Figure 47. Density Histogram at 4.0 μs

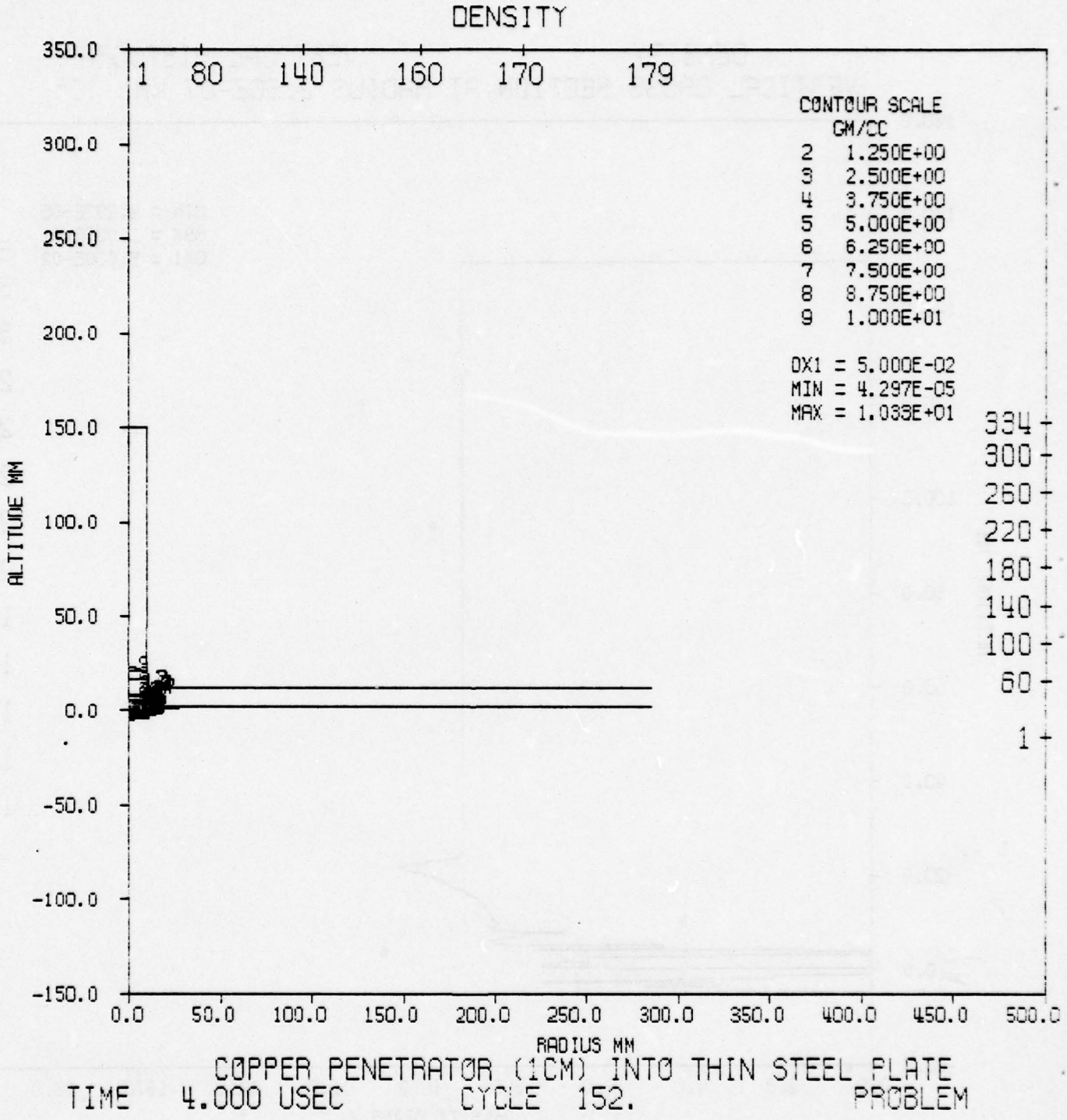

Figure 48. Density Contours at 4.0 µs

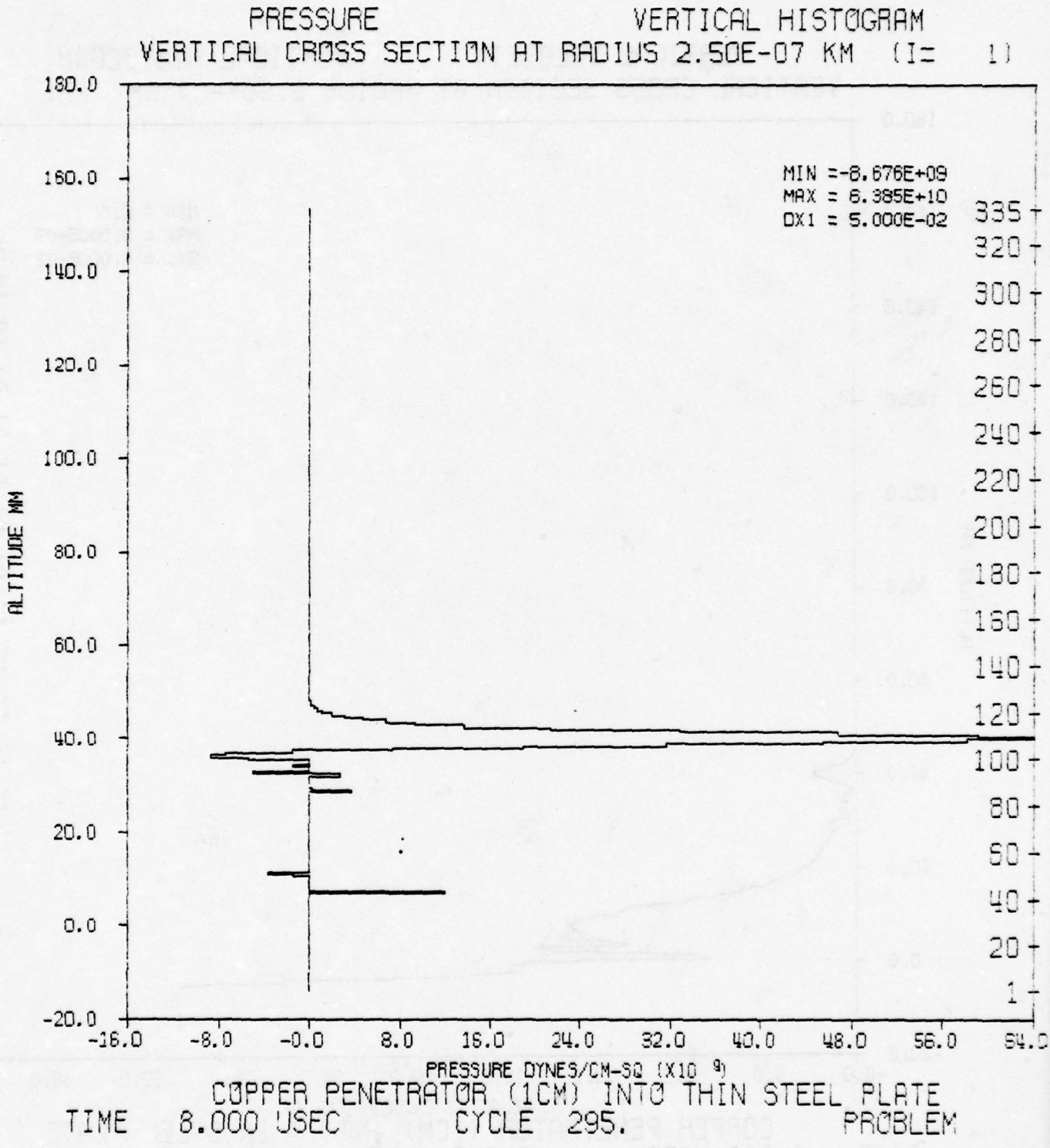

Figure 49. Pressure Histogram for 8 μs

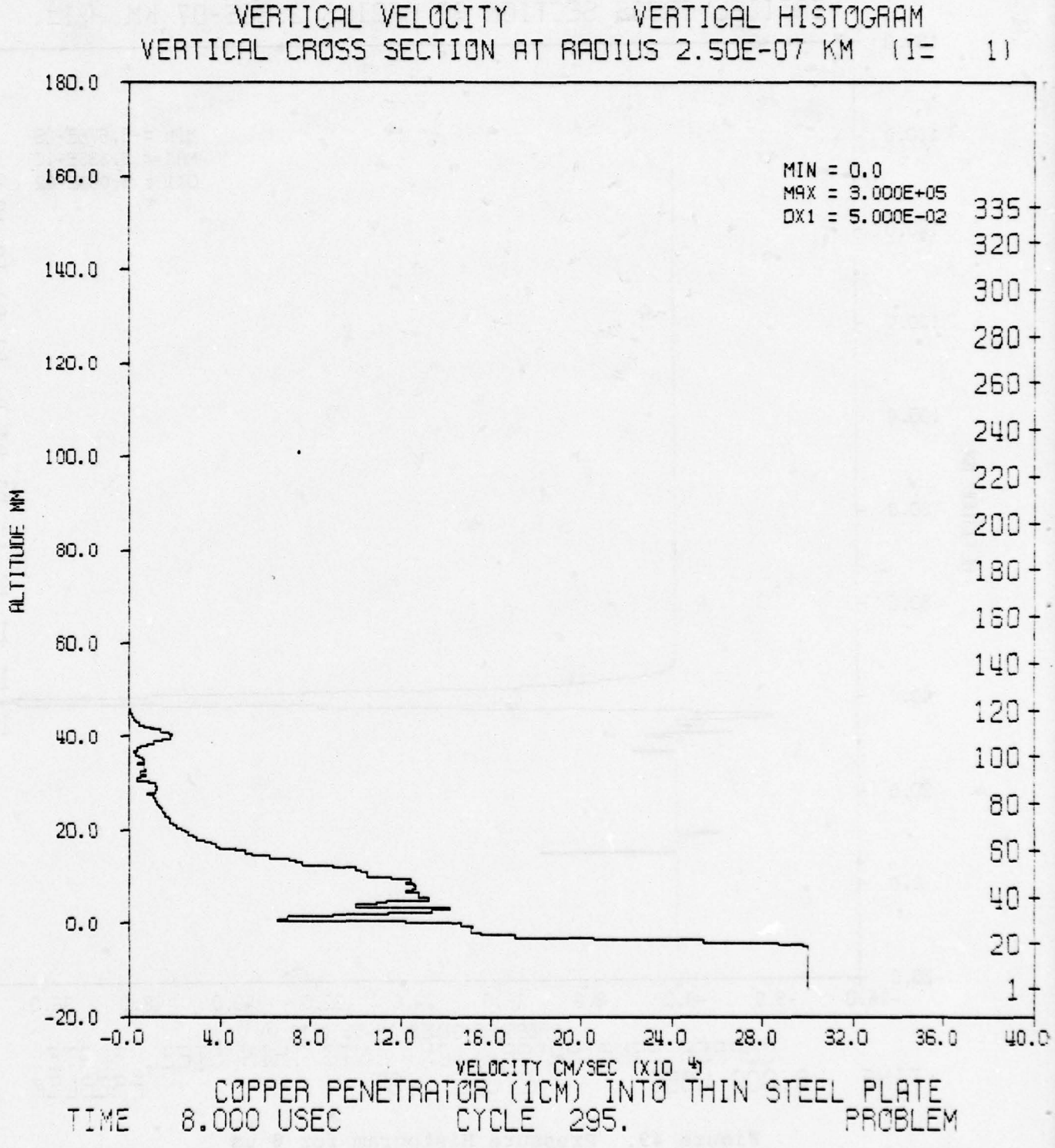

Figure 50. Vertical Velocity Histogram at 8 μs

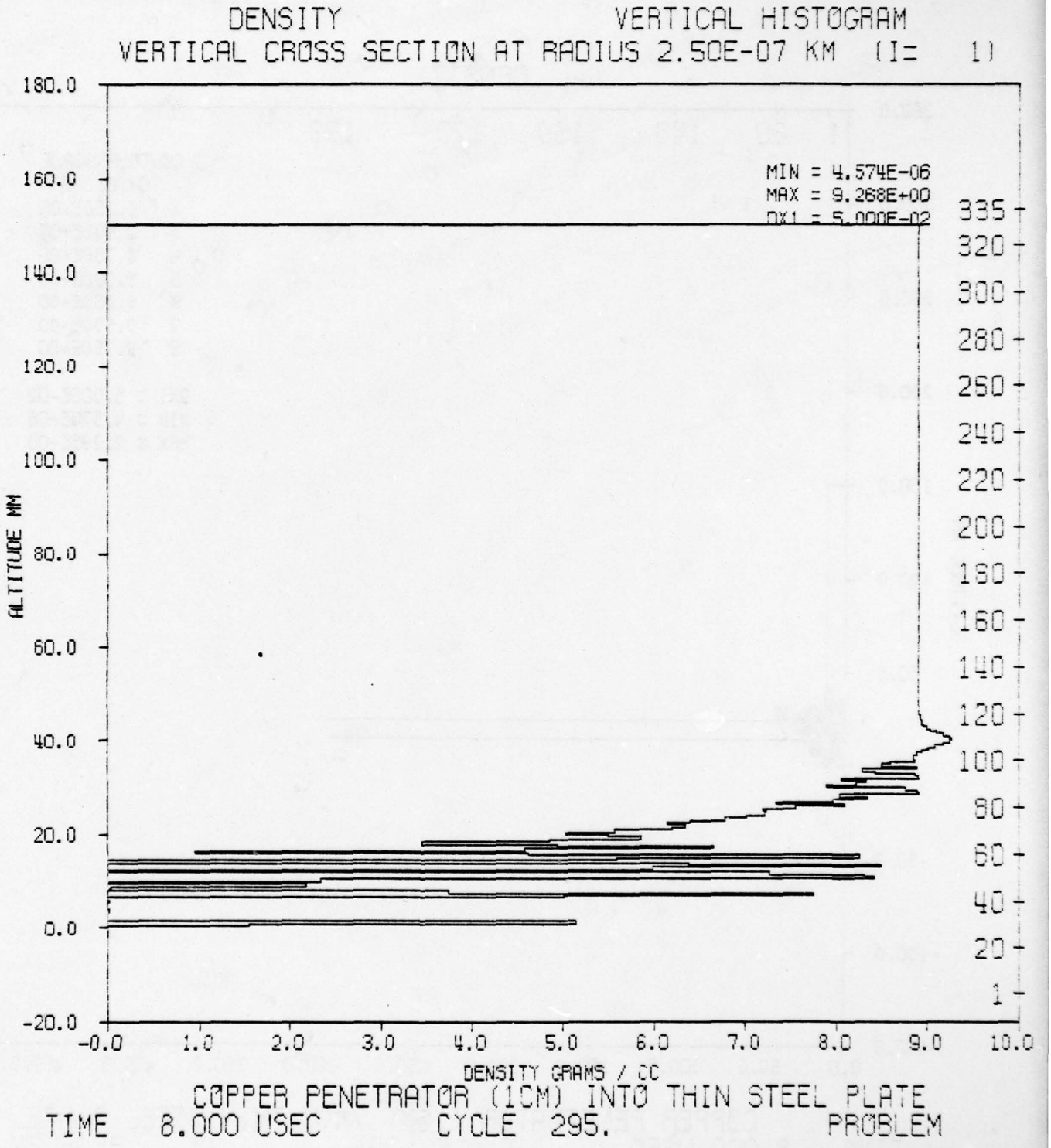

Figure 51. Density Histogram at 8 µs

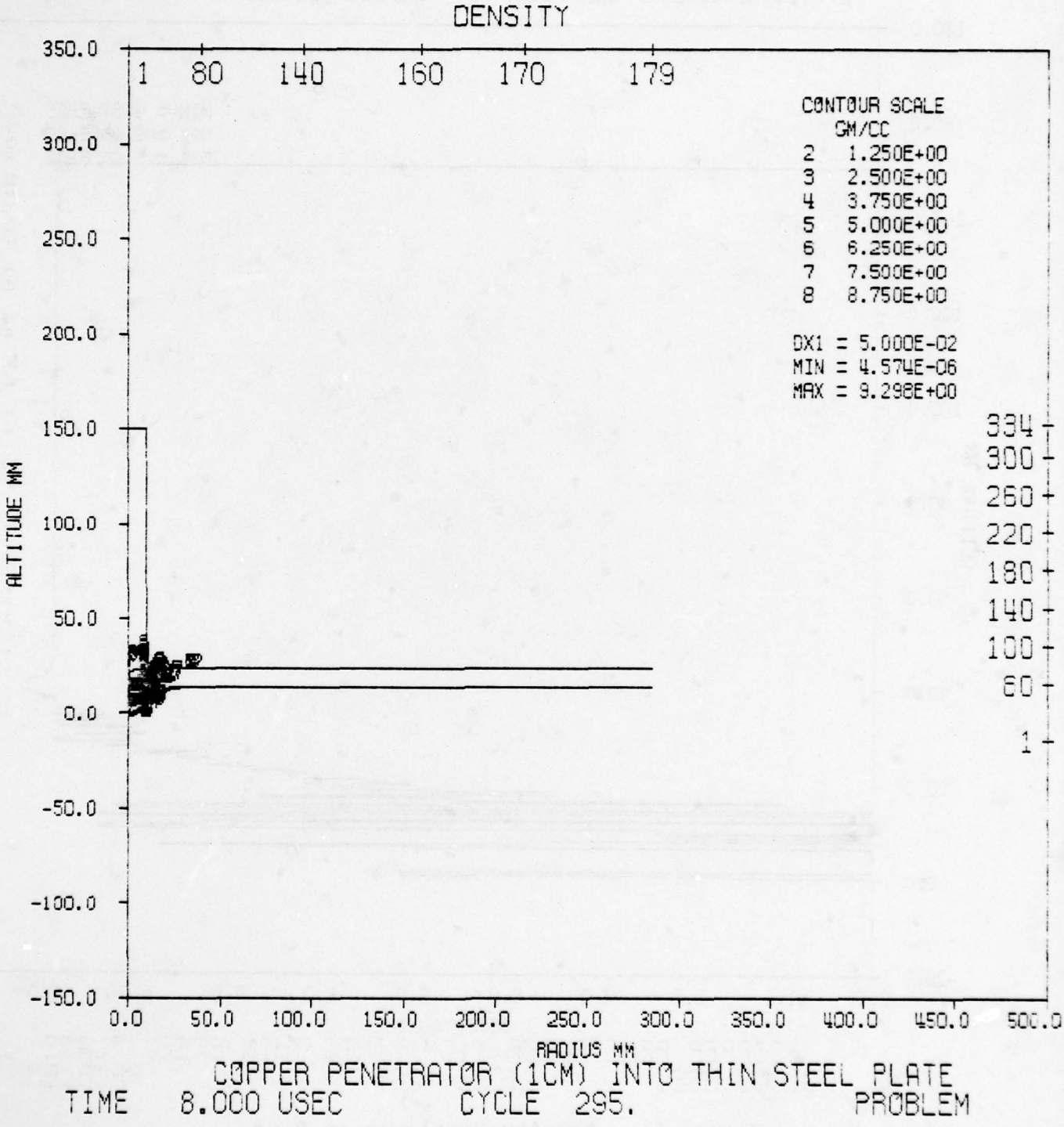

Figure 52. Density Contours at 8 μs

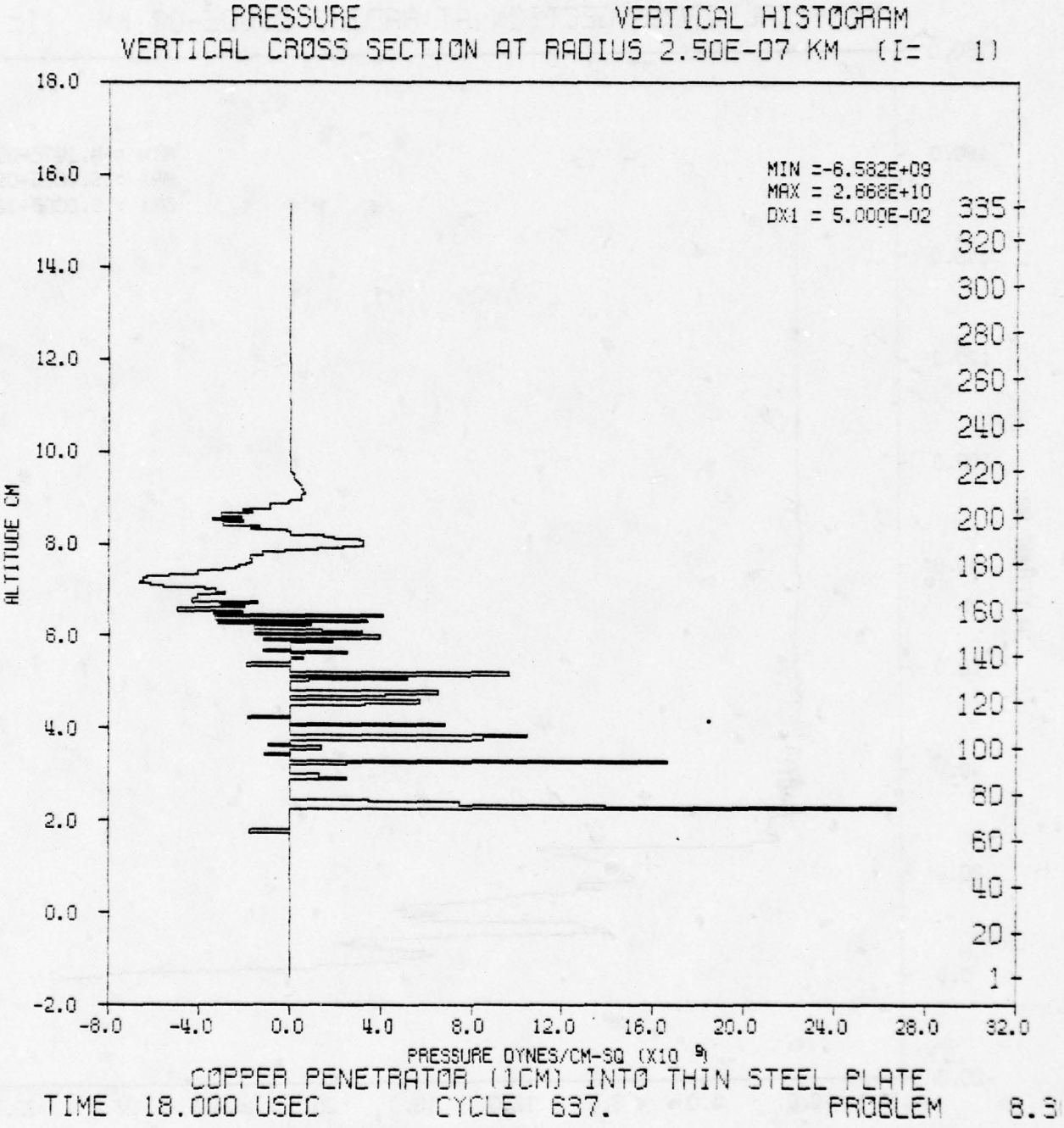

Figure 53. Pressure Histogram at 18 μs

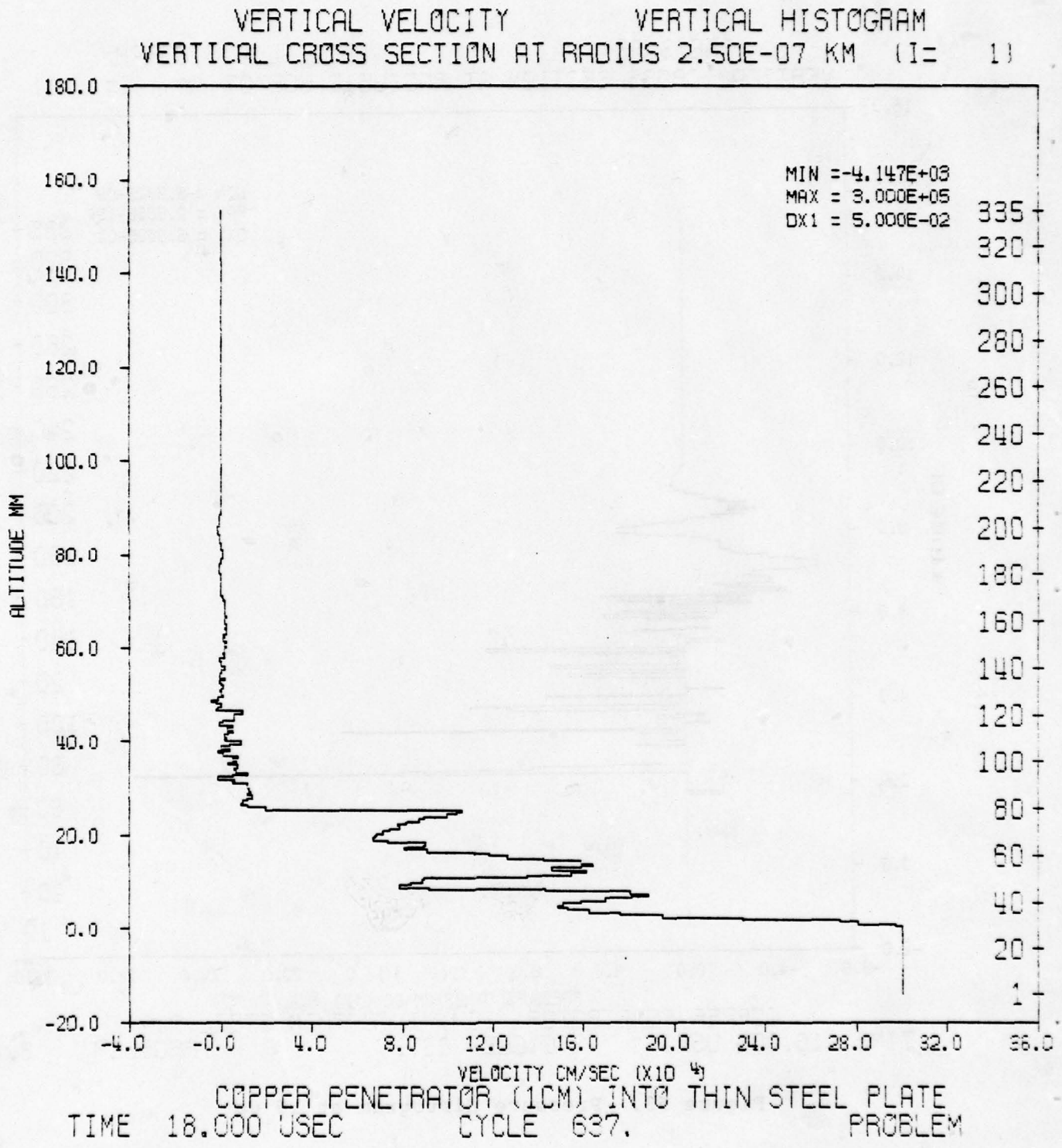

Figure 54. Vertical Velocity Histogram at 18 µs

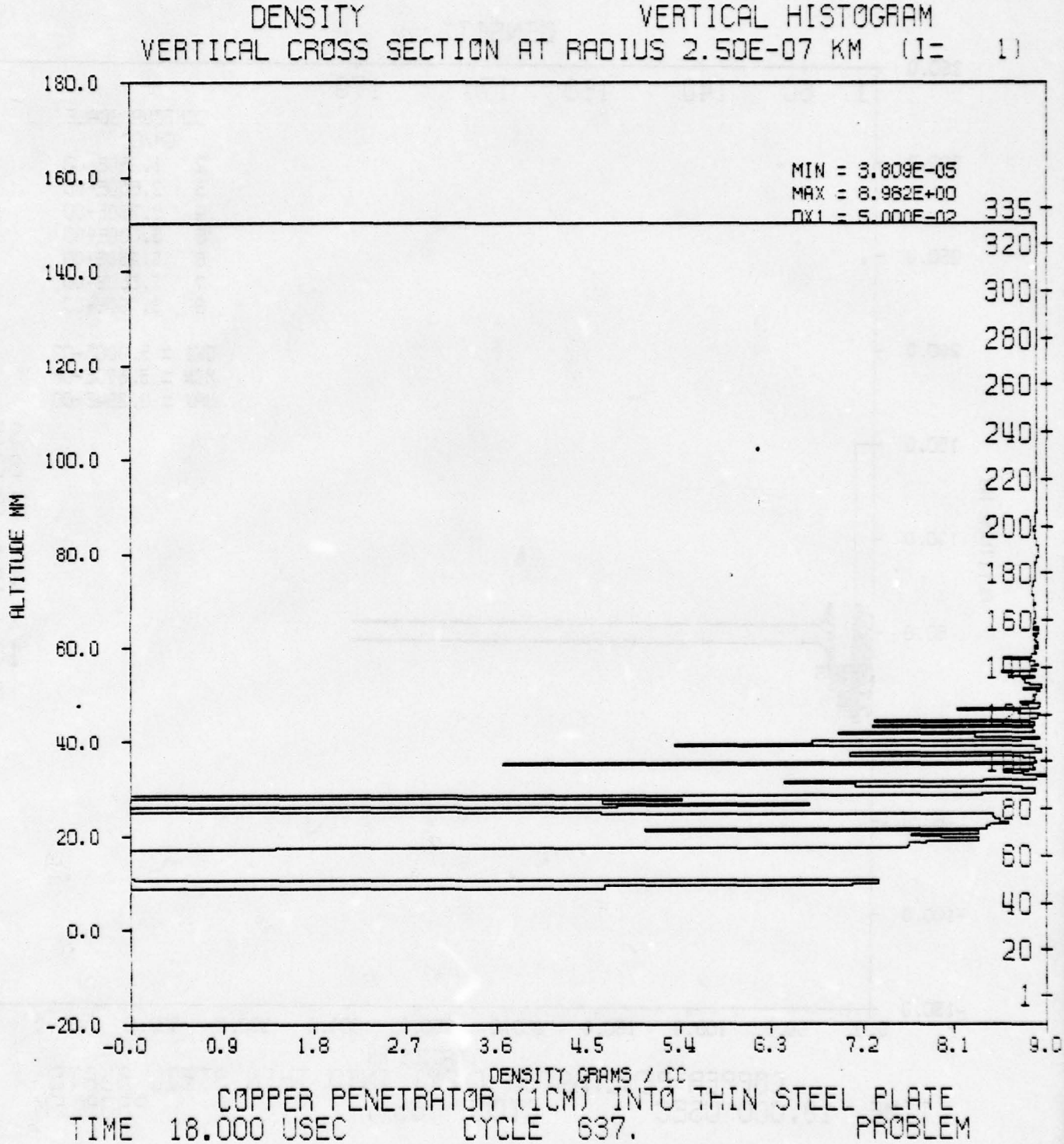

Figure 55. Density Histogram at 18 μs

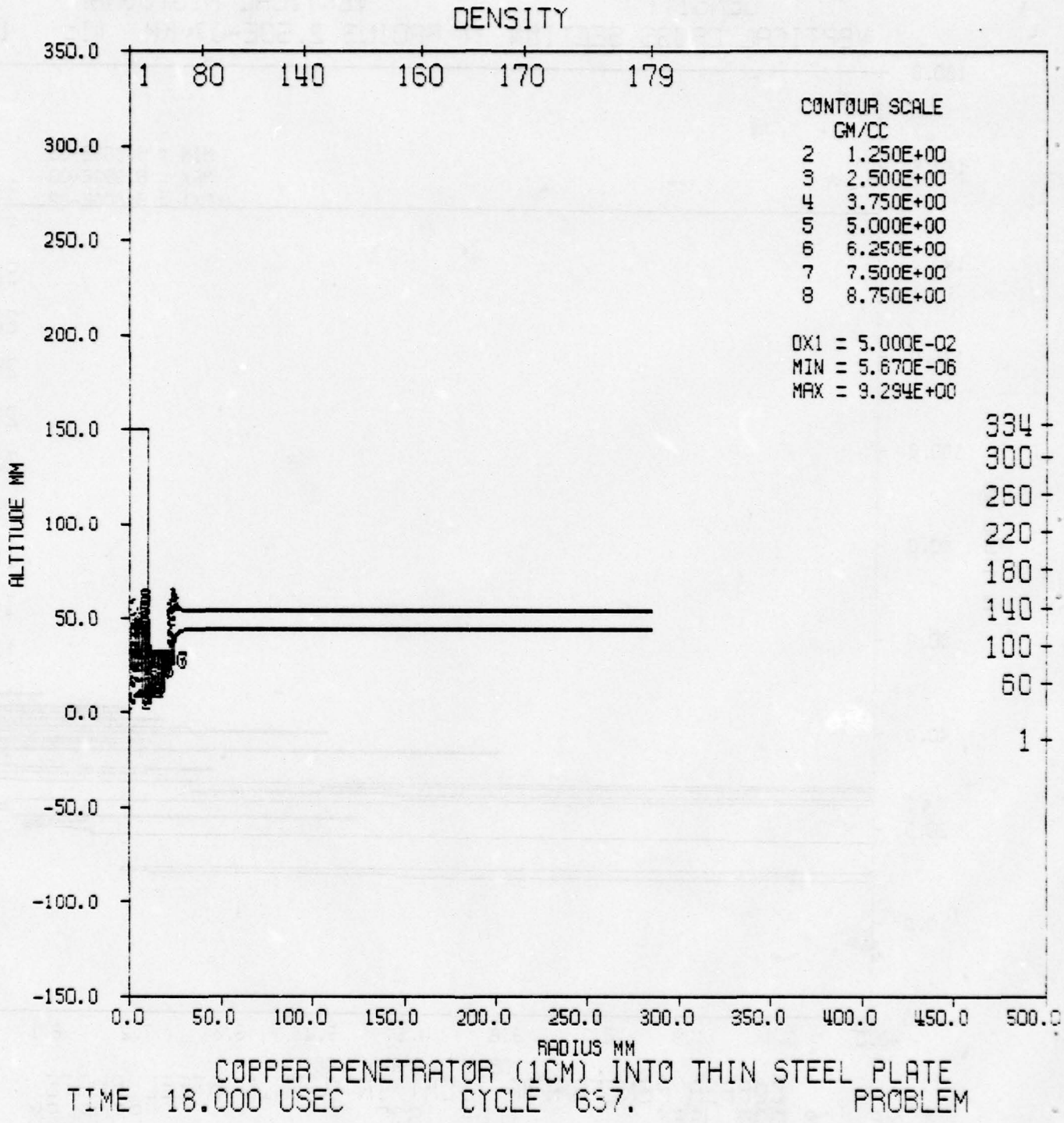

Figure 56. Density Contours at 18 μs

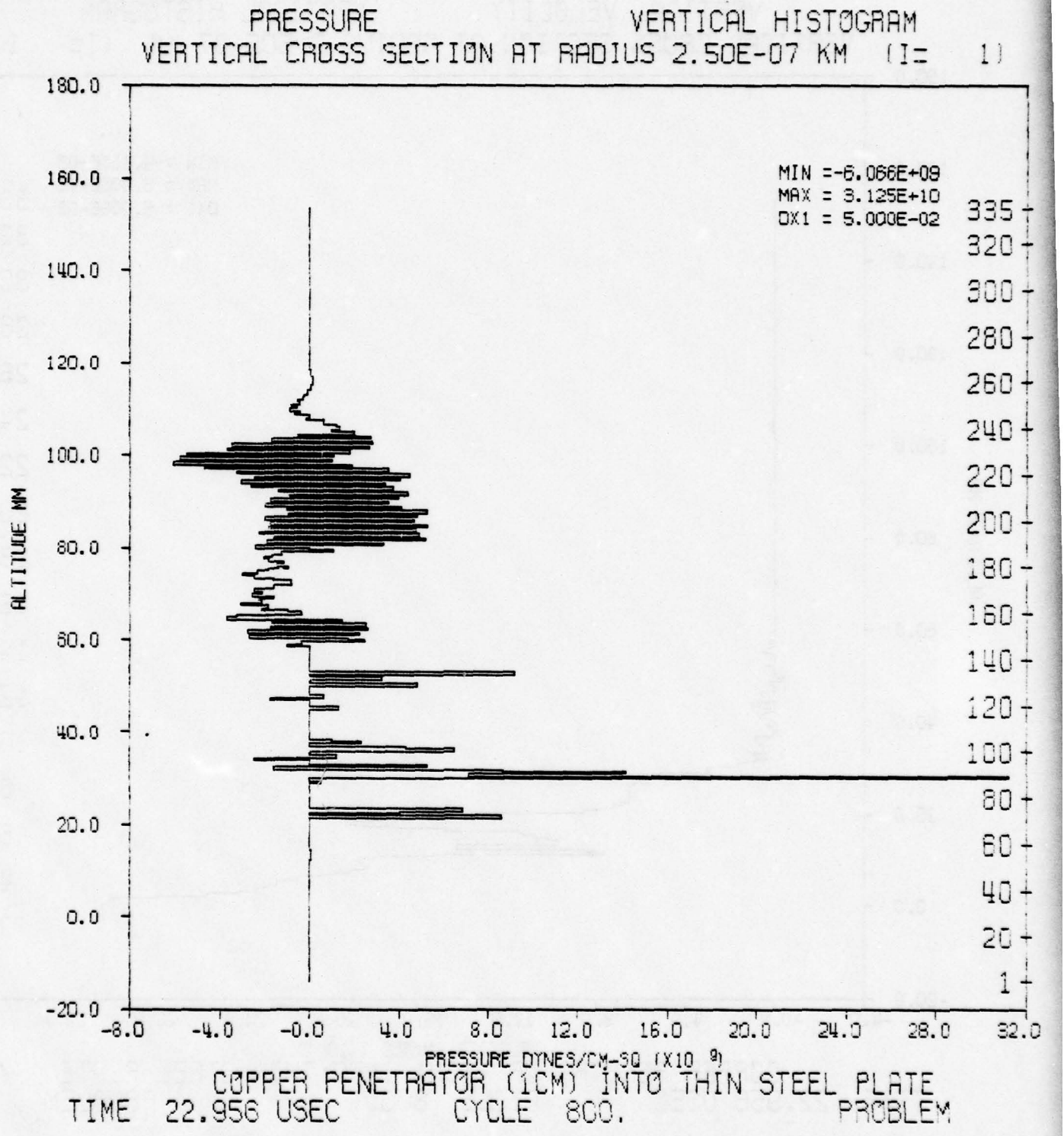

Figure 57. Pressure Histogram at 22.956 µs

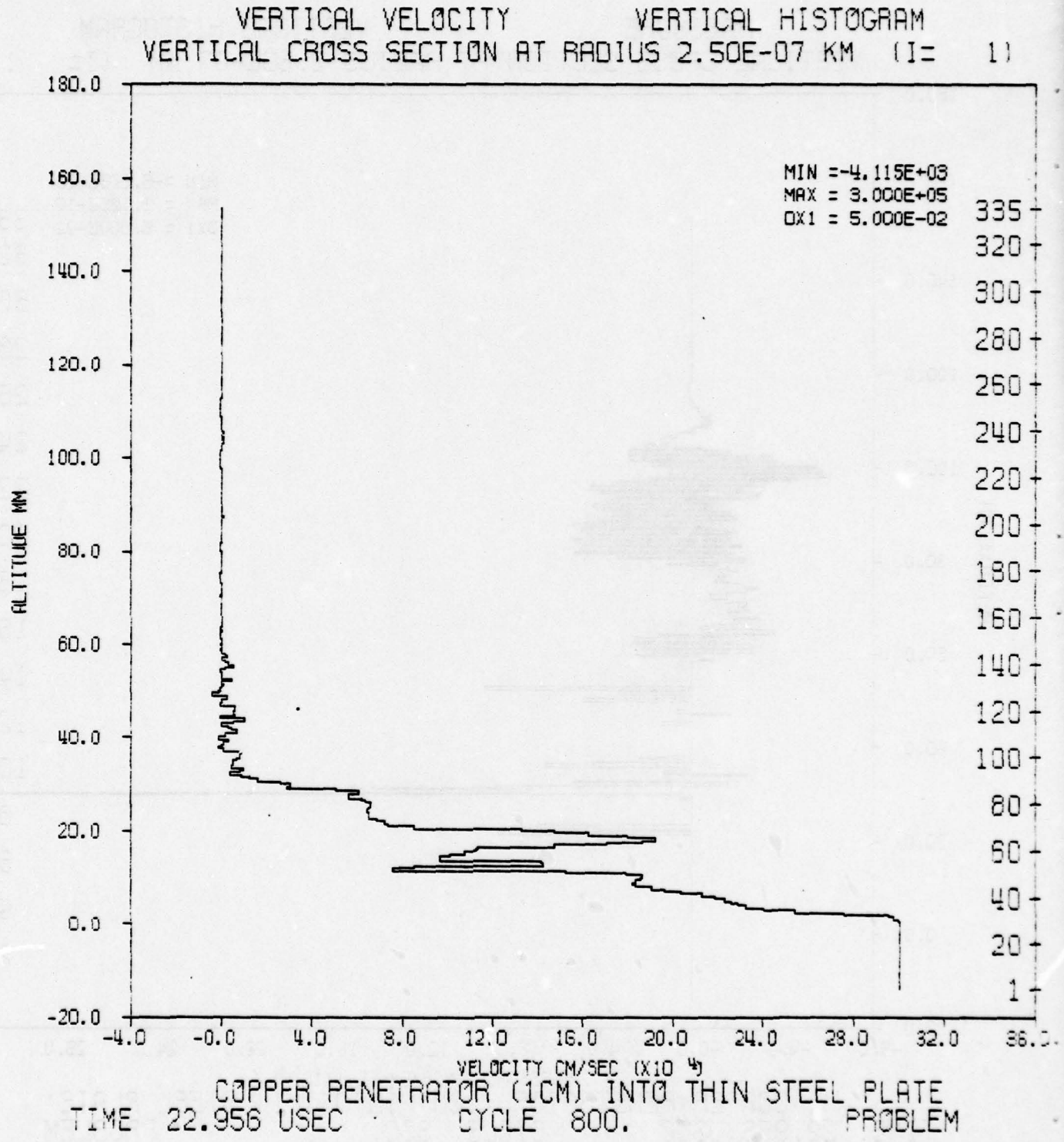

Figure 58. Vertical Velocity Histogram at 22.956 µs

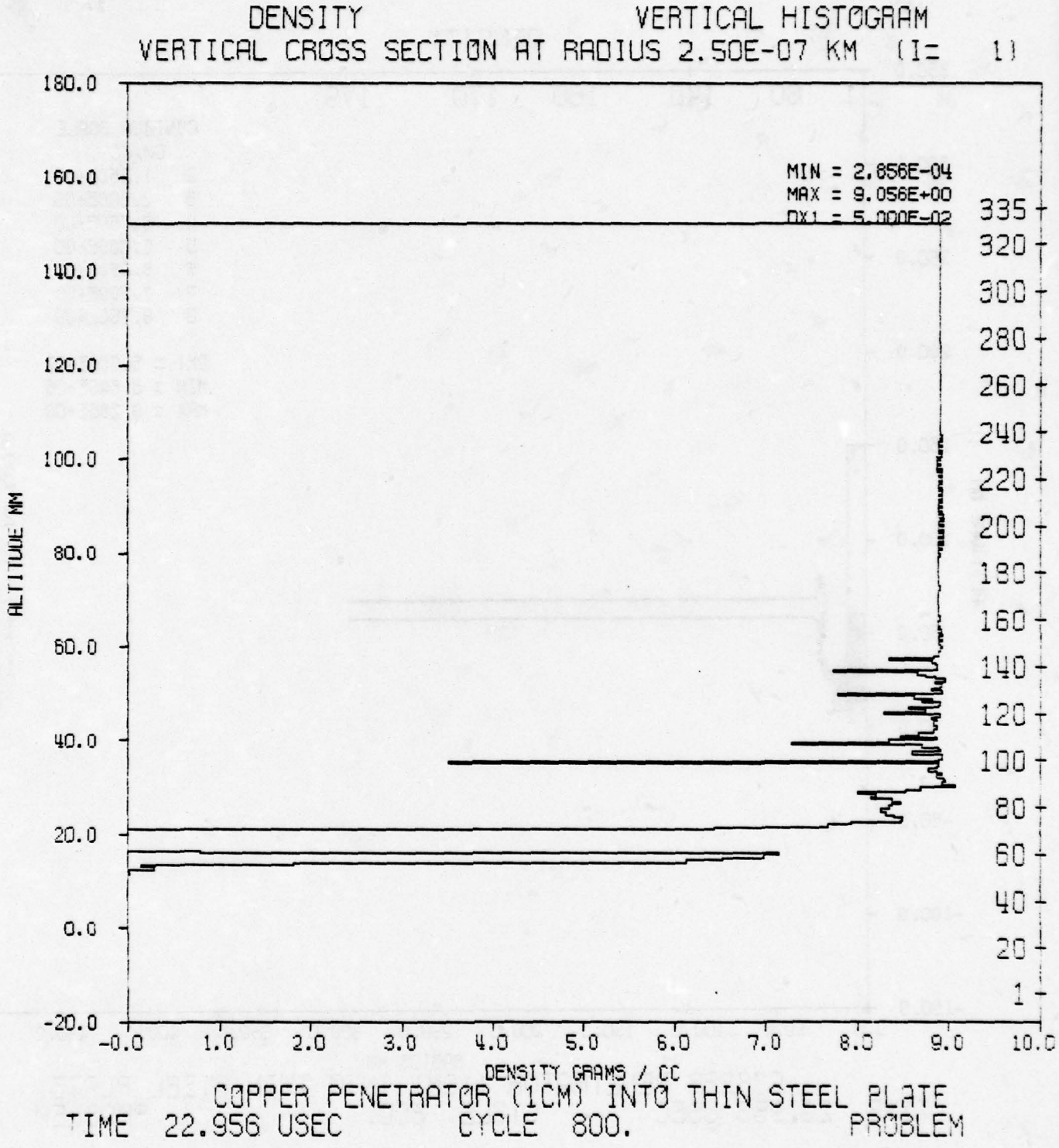

Figure 59. Density Histogram at 22.956 µs

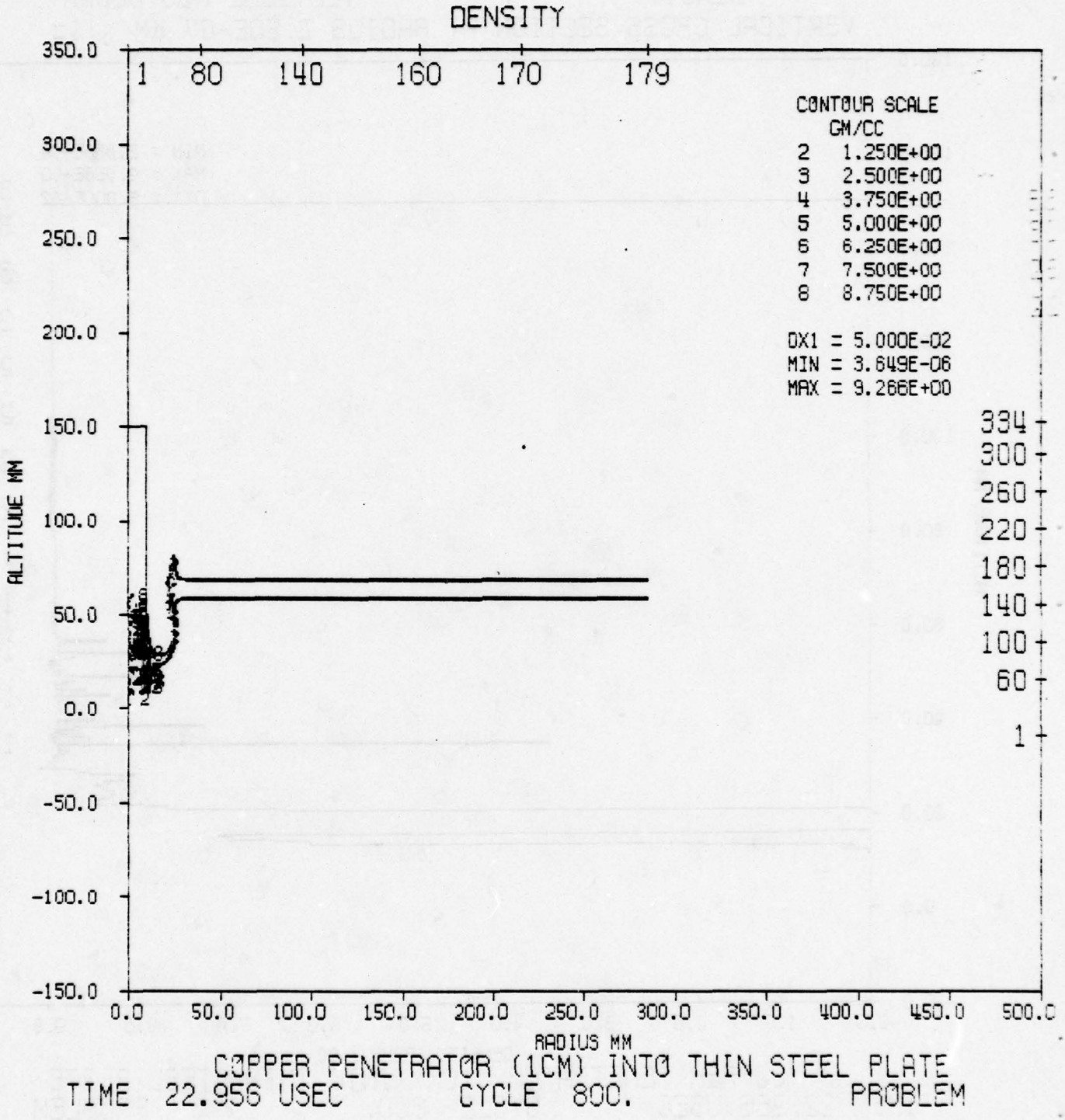

Figure 60. Density Contours at 22.956 μs

must rise rapidly to some peak value and then decline very quickly. For example, Figure 61 presents the stress pulse for a station located midway in the target plate. The 2 cm case has been used as an example. The stress wave is transmitted at the sound speed of the steel plate from the penetrator-target interface to the station location. In this case, it arrives at approximately 1 μs after impact, implying a sound speed of about 5×10^5 cm/s in the steel.

On the other side of the interface inside the penetrator, a pulse with a sharper peak is found, Figure 62. This station is located 1 cm from the interface. There is an absence of symmetry in the peak values of the stress due to the different materials. The shape of the penetrator which affects the stress waves accounts for the asymmetry.

Figure 63 presents the station data for a point located 6 cm from the interface. The stress wave reaches this point at approximately 10.5 μs. Initially, the material is forced into compression and then tension, and finally cascades into the elastic regime.

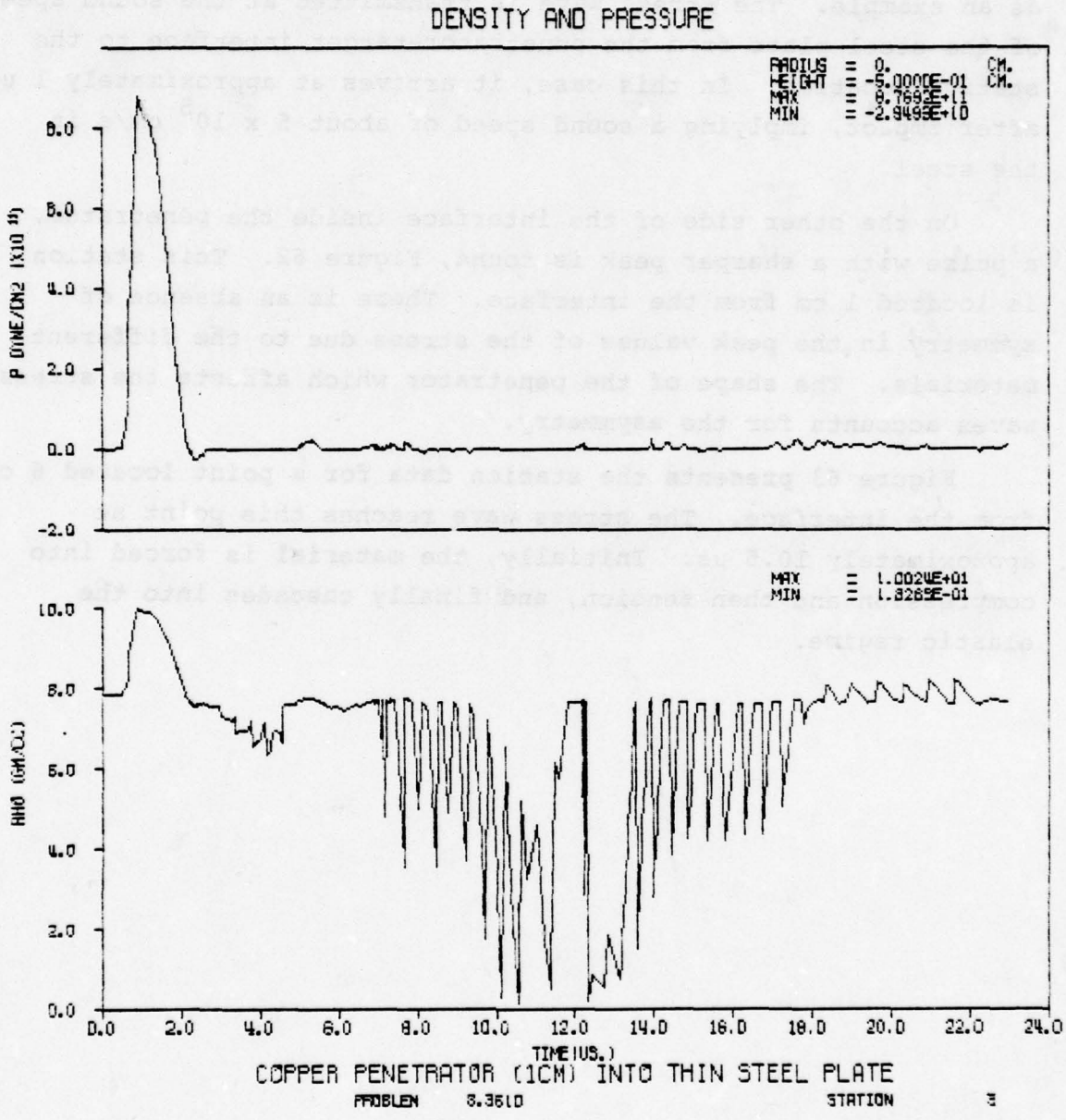

Figure 61. Density and Pressure for Station 3

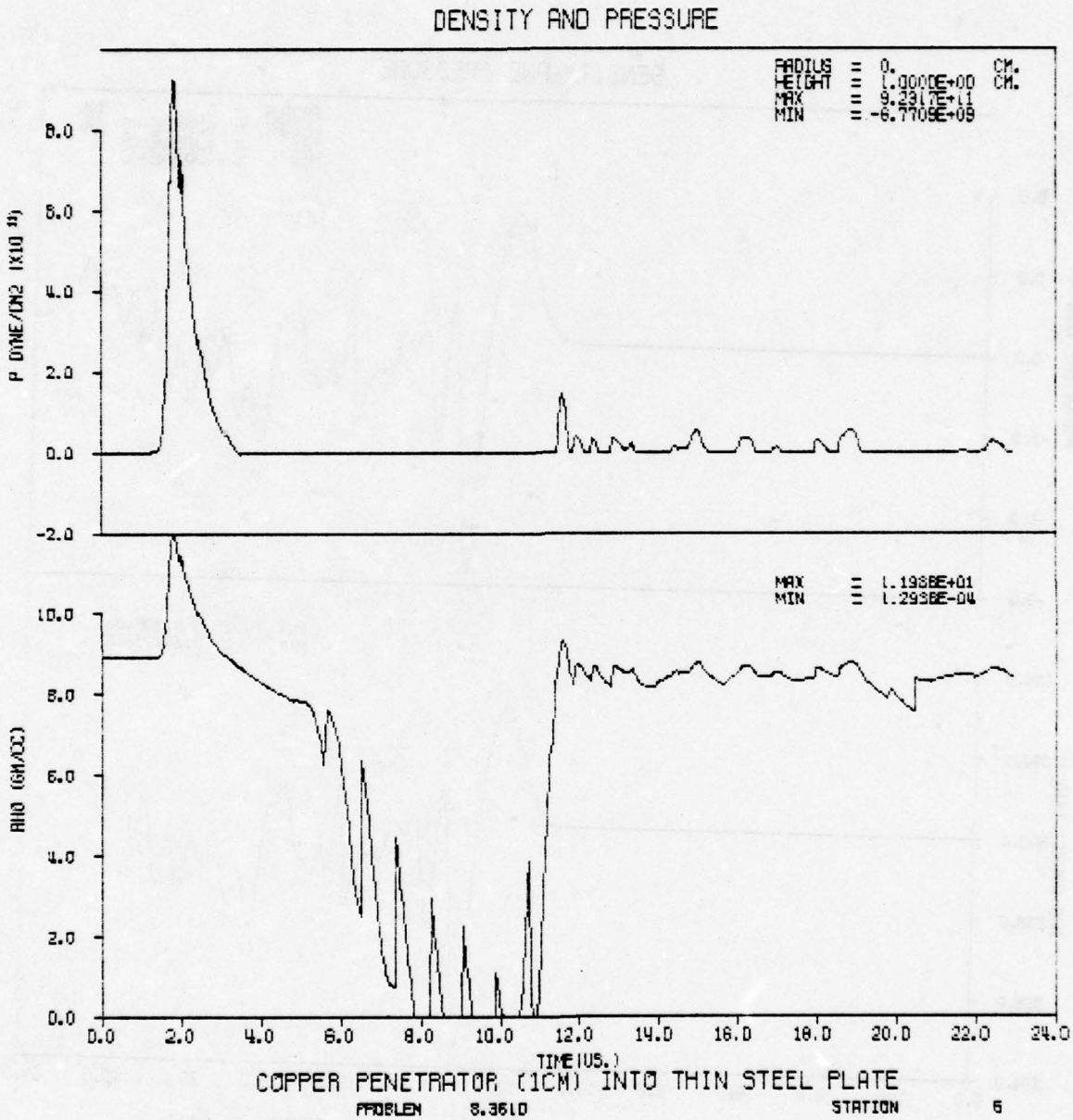

Figure 62. Density and Pressure for Station 6

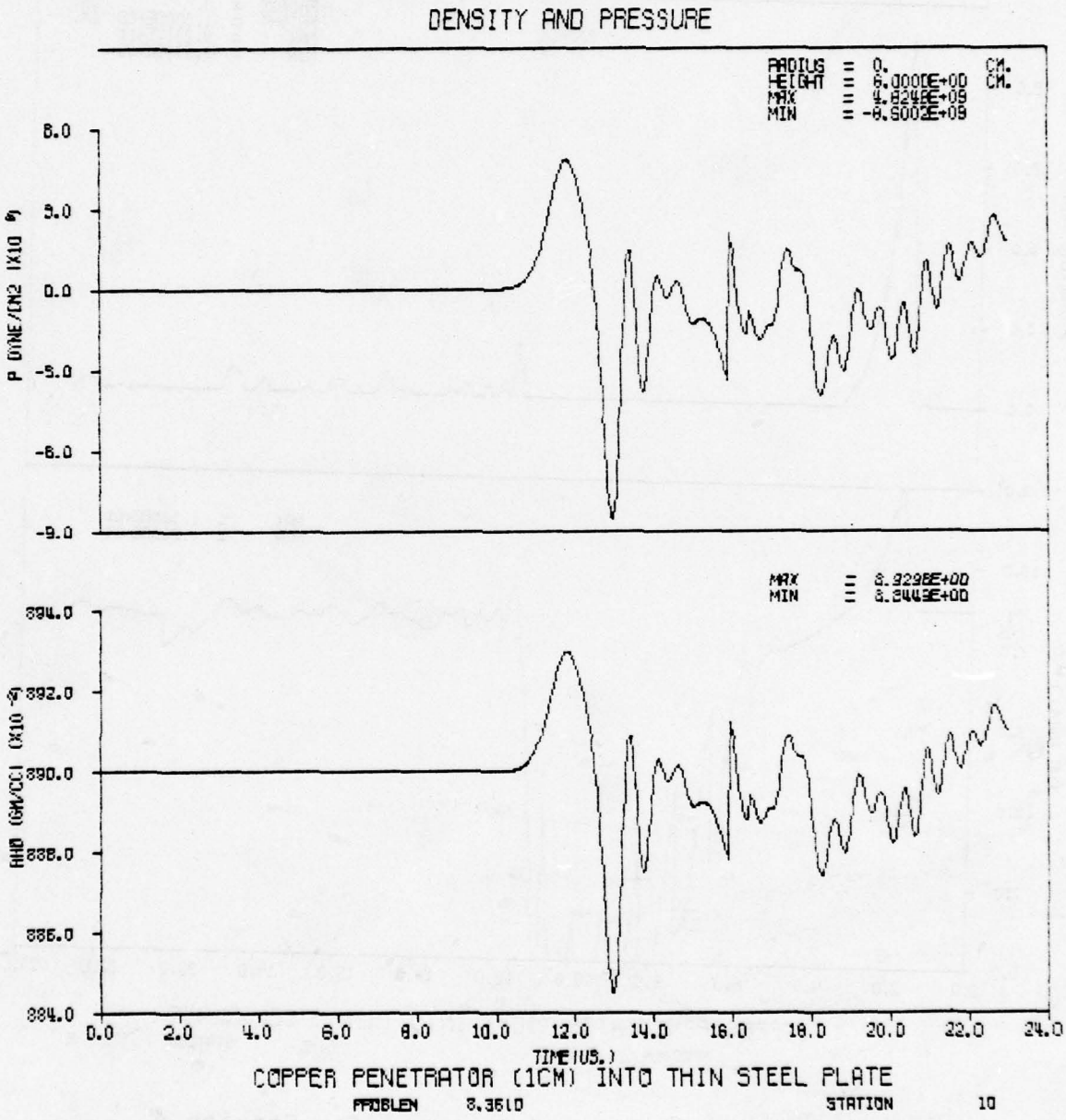

Figure 63. Density and Pressure for Station 10

Thick Plate Calculations

An additional calculation involving copper and steel was completed. Because the target chosen was a steel plate with a thickness of 15.2 cm, this calculation has been designated thick plate.

The geometry of the penetrator was a copper rod 13.7 cm in length and 0.95 cm in radius with a spherical nose. An impact velocity of 2.743×10^5 cm/s was used. Cell sizes of 0.1 cm in both the radial and axial directions were chosen for the constant zone region. Increasing zone sizes in the radial direction were used beginning at 5 cm and ending at 80 cm, with an increase of 10 percent in length over the previous value. Stations were placed along the axis to act as experimental sensors.

Upon examination of the data from the calculation, one finds differences compared to the thin plate calculations. The increased thickness of the plate will contribute to the difference, but also the geometry of the penetrator nose has an affect.

The phenomenology of the penetration process is marked by an initial pulse followed later in time by what could be characterized as a semi-steady-state pulse. The "initial" peak values for this calculation are presented in Table 6 for comparison with the information presented in Tables 4 and 5. Peak value measurements can be misleading as we are about to see. The data for pressure and density for the station located 4 cm from the interface within the target are shown in Figure 64. The first peak value is approximately 400 kbars, although the maximum value for this station is over 900 kbars.

A similar effect is seen inside the penetrator. Initially, the first peak is the maximum as shown in Figure 65. Station 12 was located on the axis of symmetry 1 cm from the penetrator-target interface. Figure 66 shows the data from station 13. At 3 cm along the axis (Figure 67), the first peak is no longer

a maximum value. The initial stress wave has been overcome with the stress waves induced by the shoulder loading effect from the geometry of the penetrator.

Table 6. First Peak Values

Distance cm	Pressure Dynes/cm^2
INSIDE PENETRATOR	
0	6.82×10^{11}
1	3.08×10^{11}
2	1.49×10^{11}
3	5.00×10^{10}
INSIDE TARGET	
-15	0.38×10^{9}
-13	1.77×10^{9}
-11	2.50×10^{9}
- 9	5.00×10^{9}
- 7	7.00×10^{9}
- 5	2.00×10^{10}
- 4	3.50×10^{10}
- 3	5.80×10^{10}
- 2	1.10×10^{11}
- 1	2.02×10^{11}

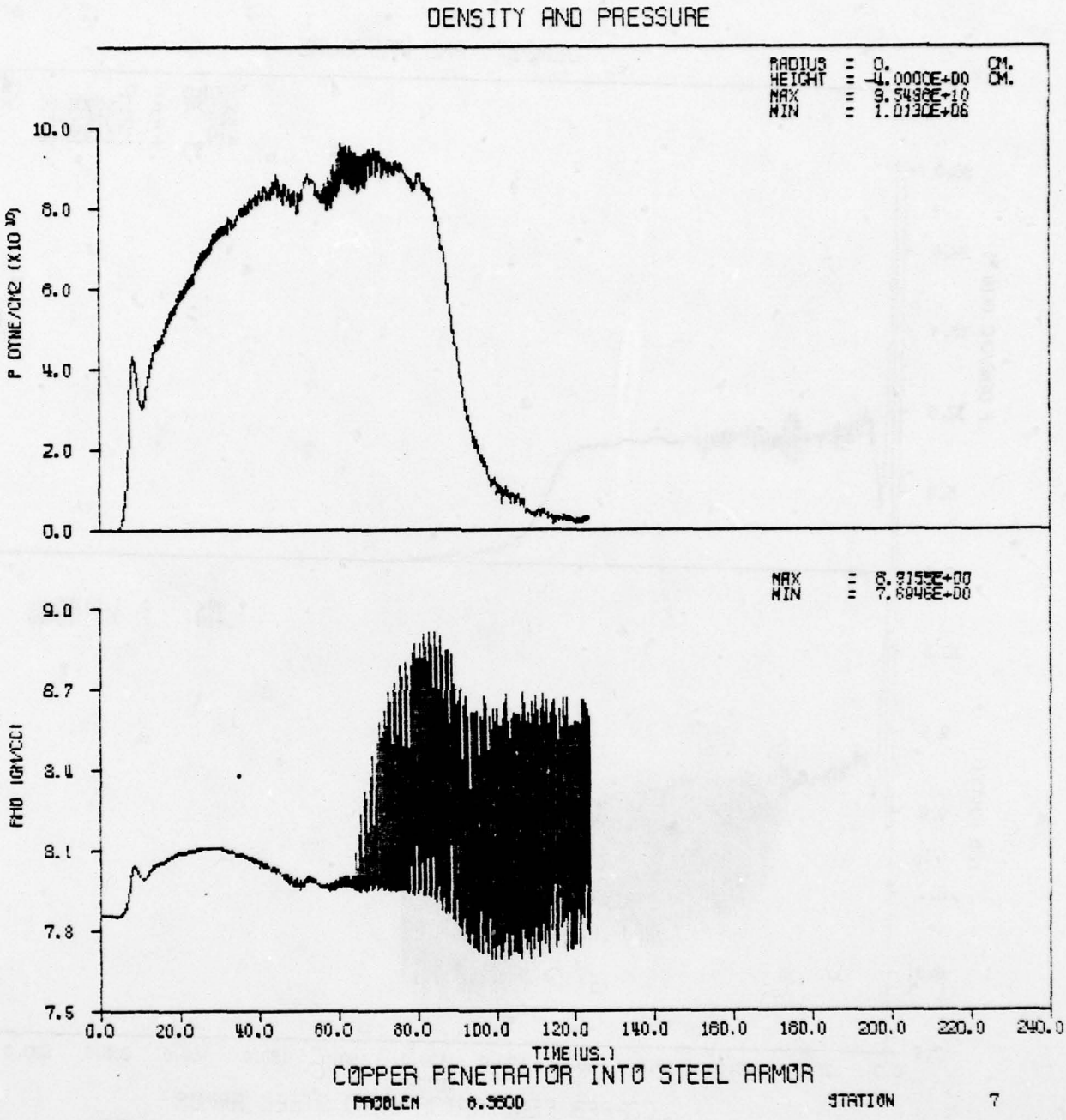

Figure 64. Density and Pressure for Station 7

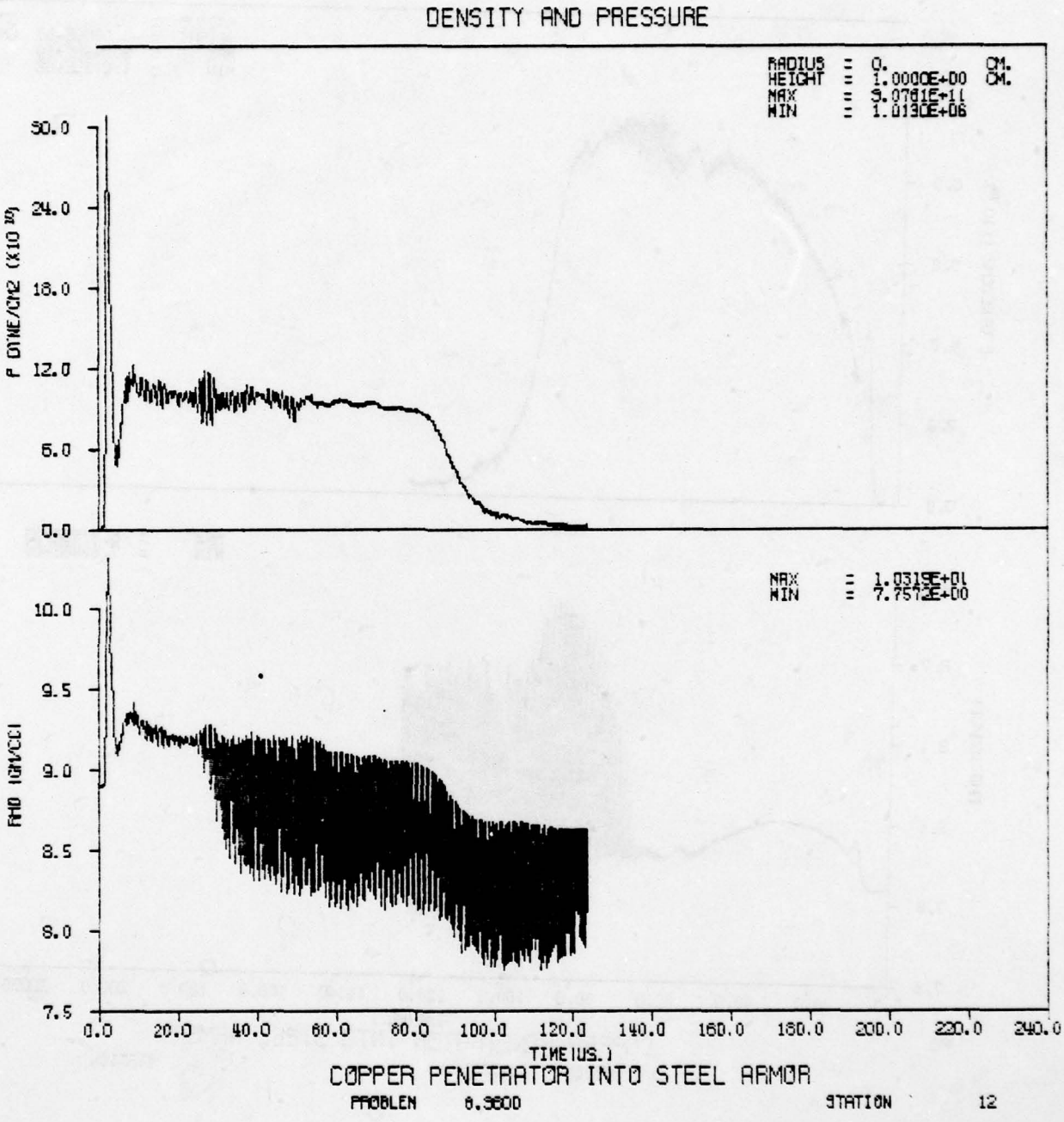

Figure 65. Density and Pressure for Station 12

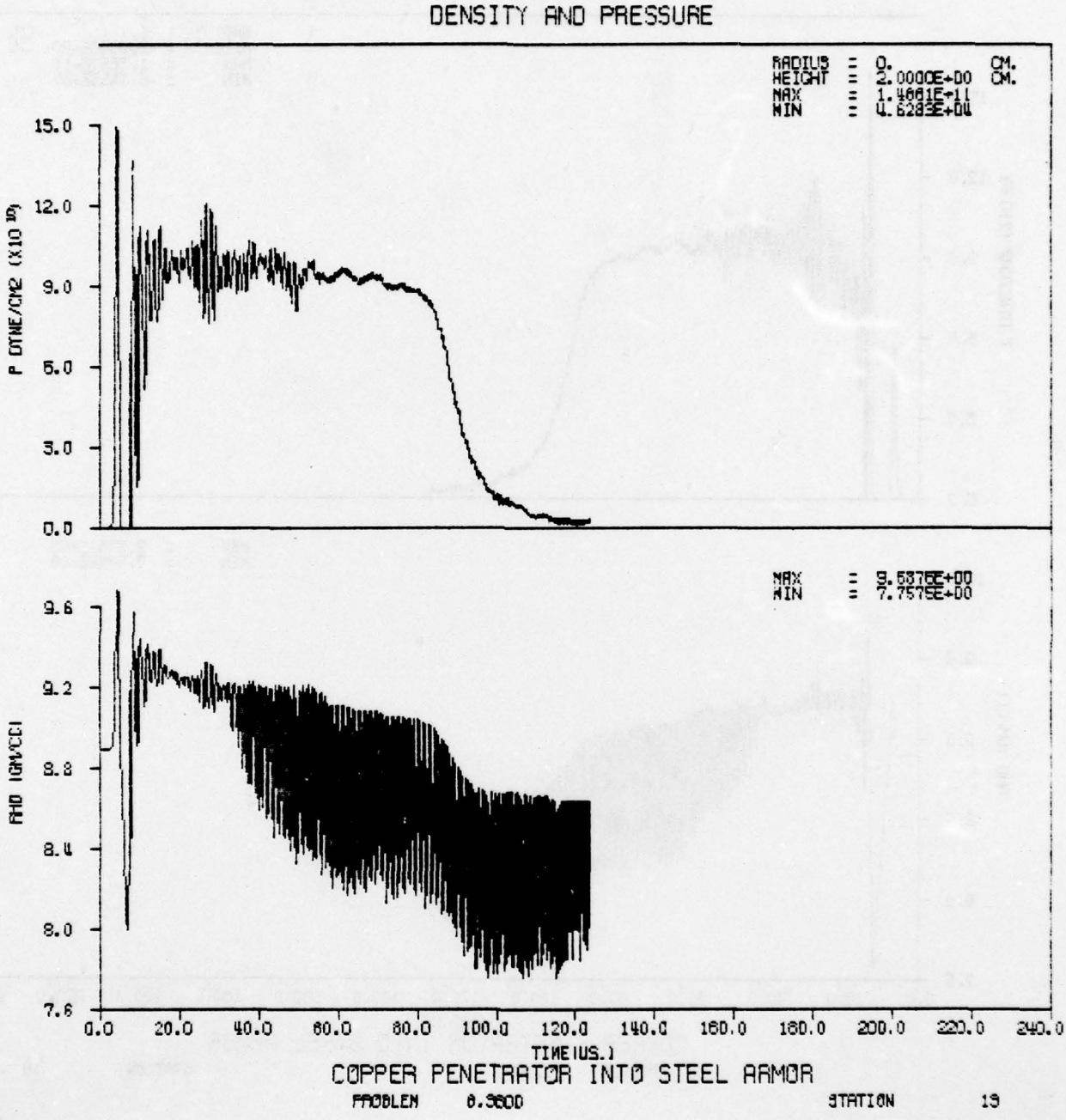

Figure 66. Density and Pressure for Station 13

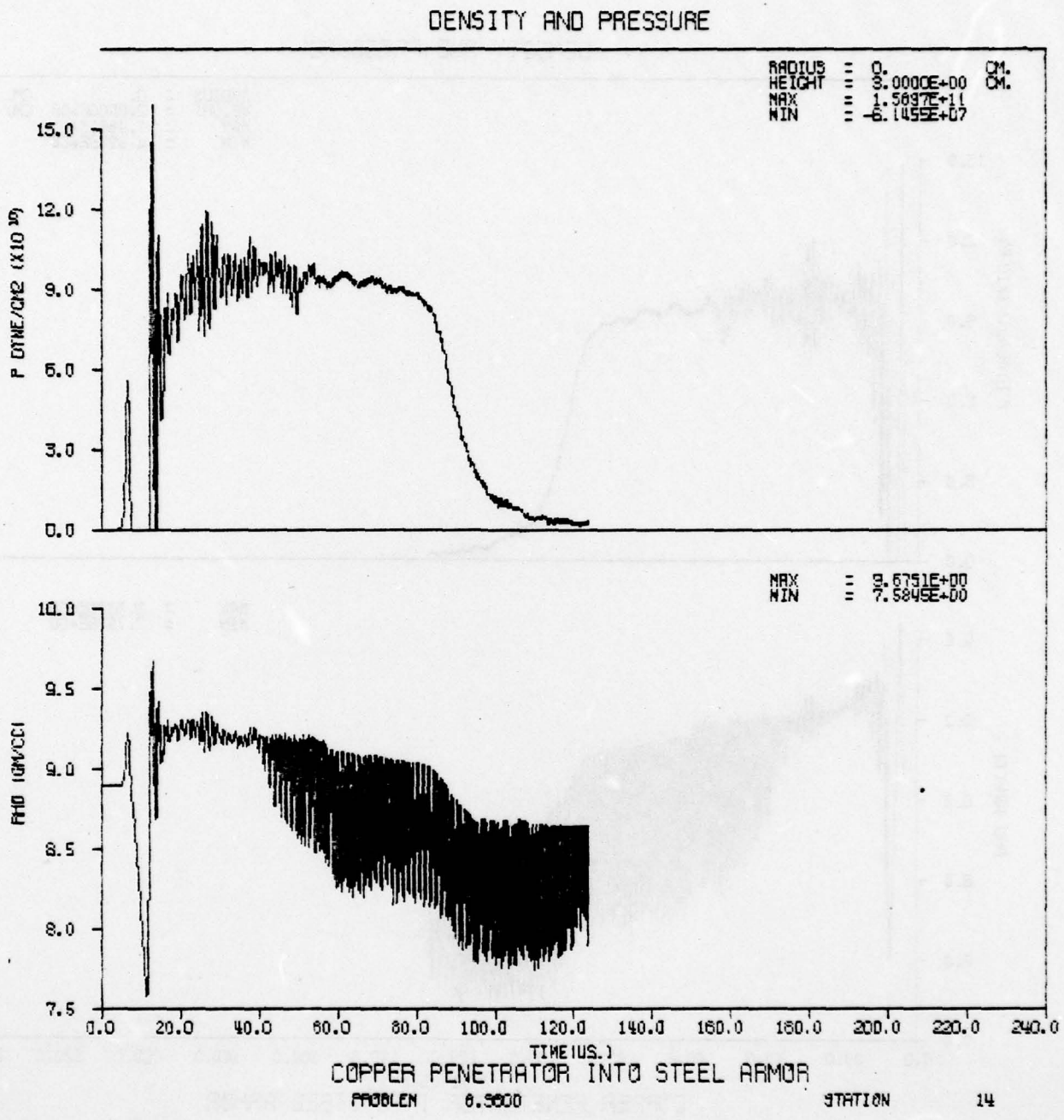

Figure 67. Density and Pressure for Station 14

SECTION V

STEEL PENETRATORS INTO STEEL PLATES

A series of steel into steel penetration events has been computed. An attempt was made to replicate an experiment in which a steel ball traveling at 10,000 ft/s impacts a steel plate. A parameter study in zone size was done to evaluate the possibility of enhancing the computed peak stress. In addition, calculations involving artificial viscosity were completed to examine its affect upon peak stresses. Variations in penetrator geometry were also investigated. A hemispherical nosed penetrator and several right circular cylinders are presented. Figures 68 and 69 indicate the geometries.

A summary of the various calculations that were run is presented in Table 7. All of the calculations were run on the Cyber 176 at Arden Hills, Minnesota, in November 1977.

A steel ball of radius 0.5 cm traveling at 10,000 ft/s was impacted upon a steel plate. Peak stresses were recorded at different locations normal to the plate interface along the line of trajectory and the point of contact. Results from the calculations were obtained from the station data to compare with measured peak stresses. A previous coarse zone calculation had shown peaks to be considerably less than the experimental data. Problem 8.2 improved the zone definition by a factor of two in r and z directions ($\Delta r, \Delta z = 0.0336$ cm). Table 8 compares the experimental data and the results from the stimulation. Problem 8.3 is identical, i.e., mesh size and input, but was completed with a higher yield strength for the steel. However, this change made little difference upon the resultant peak stresses.

Problems 8.4, 8.41, and 8.5 were attempts to study features of the elastic-plastic treatment of the HULL code. All of the above problems simulated a penetrator with the shape of right circular cylinder 6 cm in length and 1.27 cm in radius. Again,

Classes of Problems

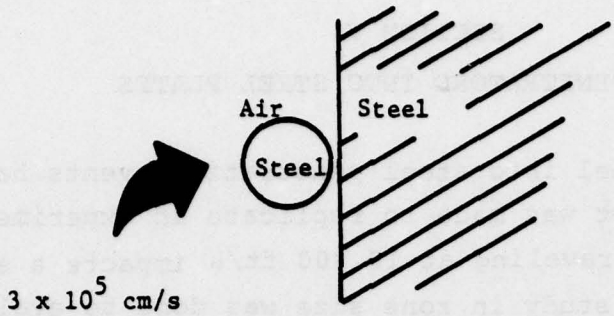

CLASS
1a

Figure 68a. Steel Ball into Semi-Infinite Steel Plate

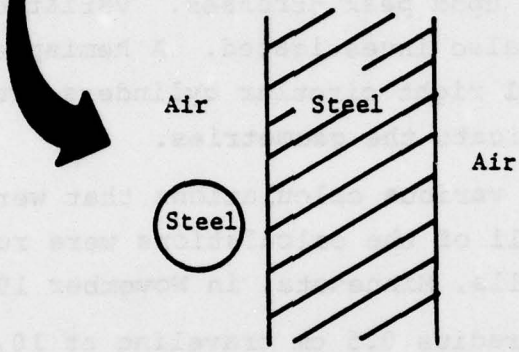

1b

Figure 68b. Steel Ball into Steel Plate

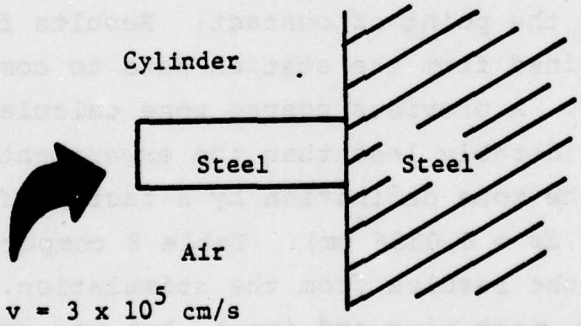

2a

Figure 69a. Steel Cylinder into Semi-Infinite Steel Plate

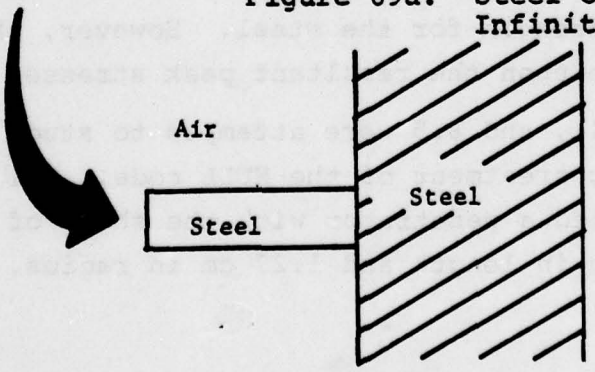

2b

Figure 69b. Steel Cylinder into Steel Plate

Table 7. Description of Problems

Class	Problem Number	Description	Zoning (Square) (radial and axial dimensions in cm)
1a	8.1	Steel ball (0.5 cm) into semi-infinite plate yield viscosity = 0 (no artificial viscosity)	0.0336
1a	8.2	Steel ball (0.5 cm) into semi-infinite plate yield strength = 4.6 kbars, velocity = 3×10^5 cm/s viscosity = 1 (artificial viscosity included)	0.0336
1a	8.3	Steel ball (0.5 cm radius) into semi-infinite plate yield strength = 7.5 kbars (no artificial viscosity)	0.0336
2a	8.4	Right circular cylinder, length 6 cm, radius 1.27 cm, semi-infinite plate (no artificial viscosity)	0.05
2a	8.41	Right circular cylinder, length 6 cm, radius 1.27 cm, semi-infinite plate with strain histories and failure mode included (no artificial viscosity)	0.05
2a	8.5	Right circular cylinder, length 6 cm, radius 1.27 cm, semi-infinite plate (artificial viscosity included)	0.05
1b	9.1	Steel ball (0.5 cm radius) into 6 cm plate, 2 free surfaces (artificial viscosity)	0.05
2b	9.2	Right circular cylinder, length 6 cm, radius 1.27 cm, 2 free surfaces (artificial viscosity)	0.05
2b	9.3	Right circular cylinder, length 6 cm, radius 2 cm, 2 free surfaces (artificial viscosity)	0.05
2b	9.4	Right circular cylinder, length 6 cm, radius 0.75 cm, 2 free surfaces (artificial viscosity)	0.05

All impact velocities are 3×10^5 cm/s. Yield strengths of all problems, unless indicated otherwise, are 4.6 kbars.

Table 8. Steel Ball Study

R(cm)	Fine Zone (Prob. 8.1) Peak Stress (dynes/cm^2)	Experimental Data Peak Stress (dynes/cm^2)	Coarse Zone Peak Stress (dynes/cm^2)	Difference (%) $\left(\frac{F - C}{C}\right) \times 100$
0	6.24×10^{11}		5.46×10^{11}	14
0.5	3.15×10^{11}		2.87×10^{11}	9.8
1.0	1.96×10^{11}		1.81×10^{11}	8.3
1.5	1.31×10^{11}		1.17×10^{11}	12
2.0	9.22×10^{10}	1.3×10^{11}	8.58×10^{10}	7.5
2.5	6.86×10^{10}		6.26×10^{10}	9.6
3.0	5.34×10^{10}	5.0×10^{10}	4.84×10^{10}	10
4.0	3.31×10^{10}	4.0×10^{10}	2.91×10^{10}	14
4.5	2.66×10^{10}		2.26×10^{10}	18
5.0	2.18×10^{10}		1.81×10^{10}	20
5.5	1.80×10^{10}		1.41×10^{10}	28
6.0	1.44×10^{10}	1.5×10^{10}	1.13×10^{10}	27

the penetrator velocity was approximately 10,000 ft/s. For this type of problem, use of the failure mode made little difference at the high stress levels. Explicit viscosity is important and degrades the peak stresses appreciably as Figure 70 indicates. This viscosity is, however, sometimes necessary to use in order to smooth very severe discontinuities.

The above series of problems deals with semi-infinite plates with only one free surface. To investigate free surface effects and breakthrough by a penetrator, another series of problems were run. Each of these contained a steel target plate of 6 cm thickness. These problems were designated as problem set 9. For example, problem 9.1 features a steel ball impacting a steel plate while traveling at 10,000 ft/s. Problems 9.2, 9.3, and 9.4 are parameter studies in radius for a right circular cylinder. The results from these calculations are summarized in Figure 71. There, the peak stress along the axis is plotted as a function of distance from the penetrator-target interface.

The entire series of calculations presented in this section were run to thoroughly shake down the code and test some of the options. The results show that artificial viscosity severely dampens the peak values of stress. Fine zoning enhances the peak values from 10 to 20 percent, but one must pay a considerable price in computing time as the number of zones rises exponentially. Problem 8.31, not shown here, was an attempt to very finely zone (0.01 cm) the interface of the penetrator target. Little change was achieved by zones smaller than 0.03 cm. The variation of radius of penetrator has a significant affect upon the value of the peak stress at equidistant points from the penetrator-target interface.

Because the phase transition for iron (steel) is not treated in the equation of state, a calculation was completed that addressed this feature. The phase transition at a pressure of 130 kbar was added to the equation of state routine. The calculation was

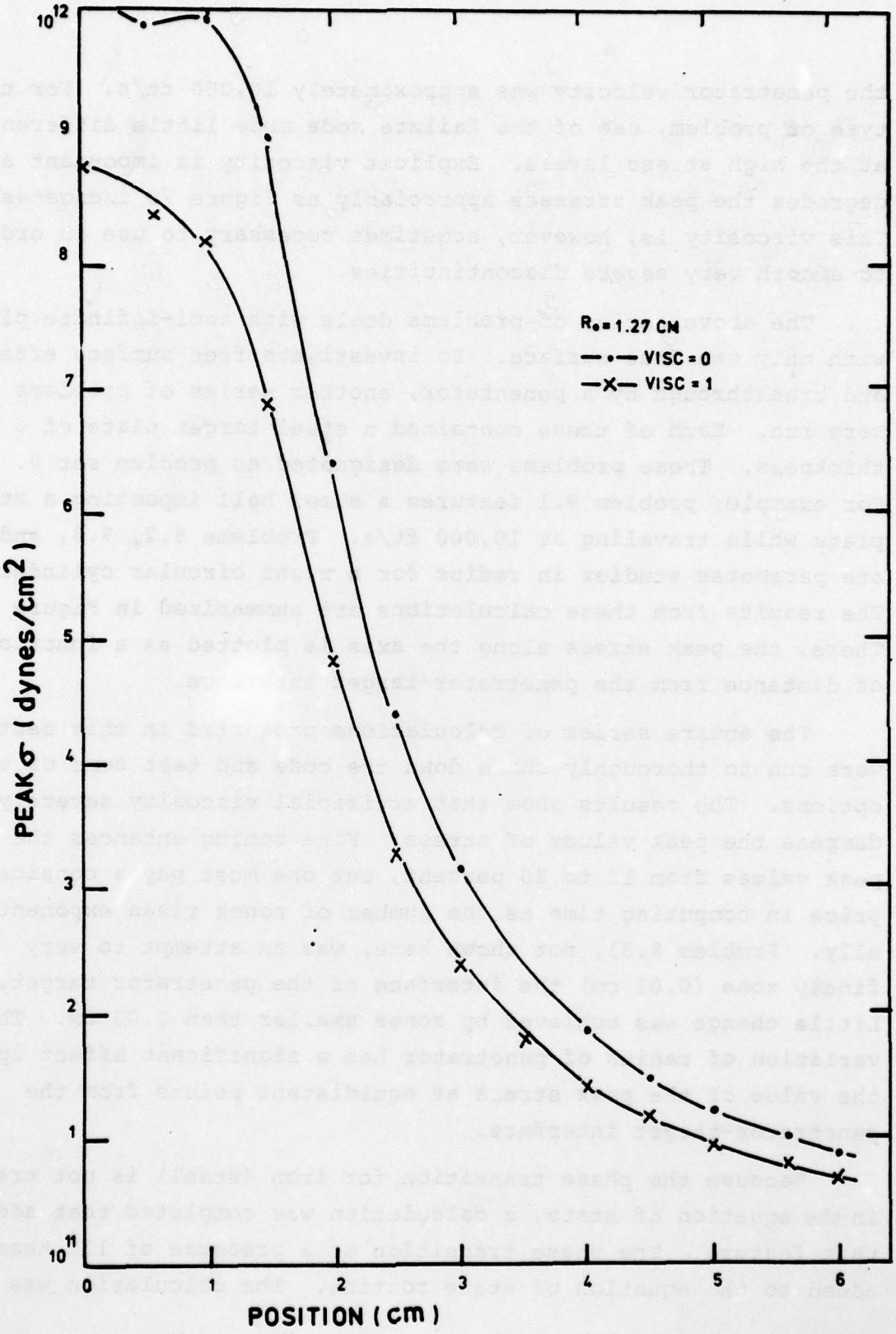

Figure 70. Peak Stress versus Position

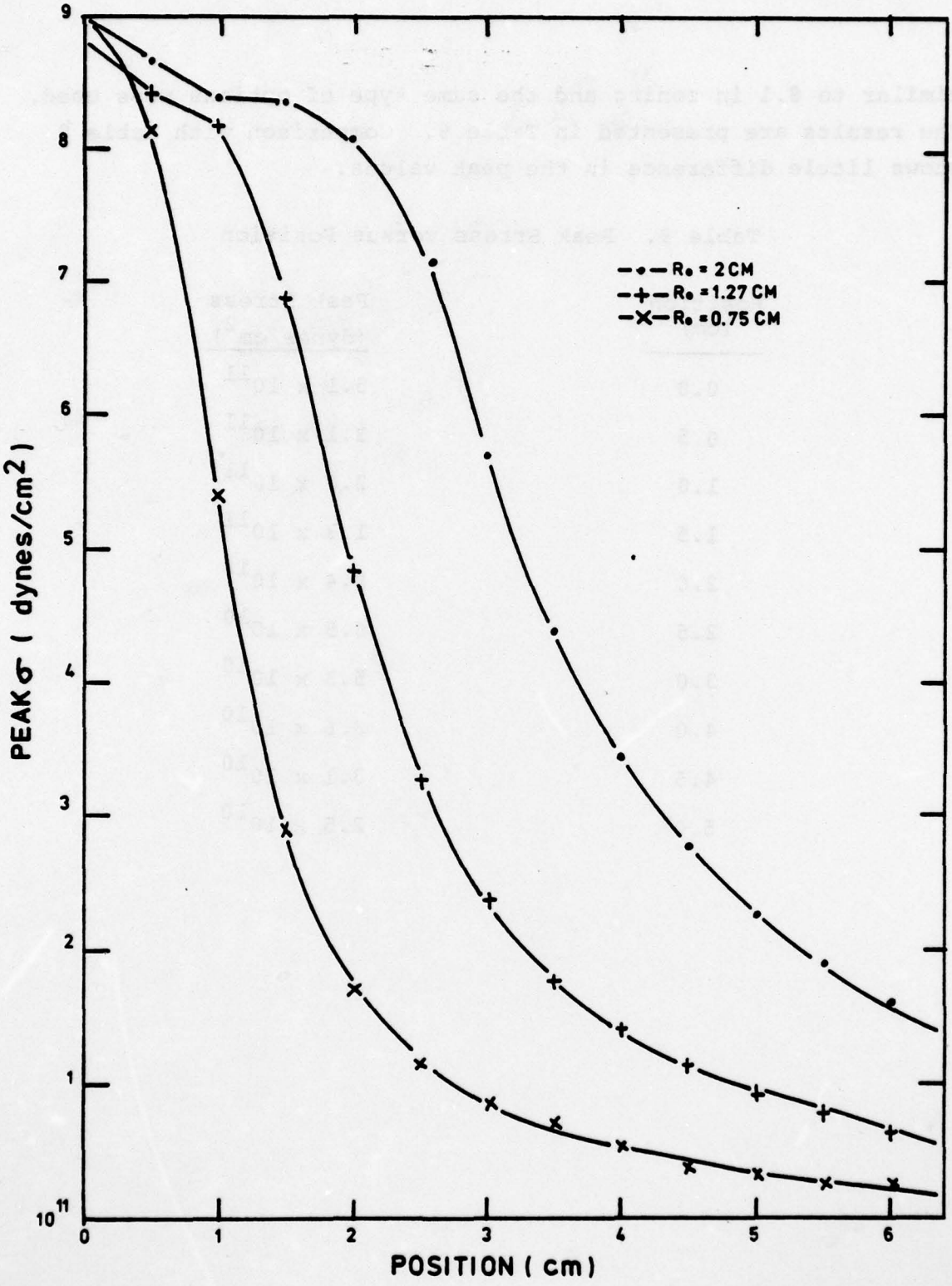

Figure 71. Peak Stress vs. Position with Explicit Viscosity

similar to 8.1 in zoning and the same type of options were used. The results are presented in Table 9. Comparison with Table 8 shows little difference in the peak values.

Table 9. Peak Stress versus Position

Position (cm)	Peak Stress (dynes/cm^2)
0.0	5.1×10^{11}
0.5	3.1×10^{11}
1.0	2.0×10^{11}
1.5	1.3×10^{11}
2.0	8.4×10^{10}
2.5	6.5×10^{10}
3.0	5.3×10^{10}
4.0	3.6×10^{10}
4.5	3.1×10^{10}
5.0	2.5×10^{10}

Iron Penetrator with Spherical Nose

This problem utilized zoning compatible, but not equal to, the previous calculations. It is an extension of the steel ball and cylinder cases that have been completed. Examination of the behavior along the axis is needed, as well as phenomenology within the penetrator. Table 10 lists the information.

Table 10. Peak Stress and Velocity versus Distance

Distance into Target (cm)	Peak Stress (dynes/cm^2)	Maximum Velocity (cm/s)
0	9.91×10^{11}	3.0×10^{5}
1	1.73×10^{11}	3.7×10^{4}
2	8.52×10^{10}	1.8×10^{4}
3	4.85×10^{10}	1.4×10^{4}
4	2.99×10^{10}	9.08×10^{3}

The values in Table 10 can be compared to those in Table 8. The peak value at the interface is considerably larger and has to do with placement of the station location. The other values are comparable with the steel ball values.

The following figures (Figures 72 through 76) demonstrate the penetration event. They are density contours for every 2.0 μs in time. After the density contours are a series of plots of the station data.

AD-A074 891 COMPUTER SCIENCES CORP ALBUQUERQUE N MEX F/G 19/4
HULL MODELING OF STRESS WAVE PROPAGATION.(U)
JUL 79 M A FRY, L P GABY F29601-78-C-0012
UNCLASSIFIED CSC-C4-C-4083 AFWL-TR-79-17 NL

2 OF 2
AD A074891

END
DATE FILMED
11-79
DDC

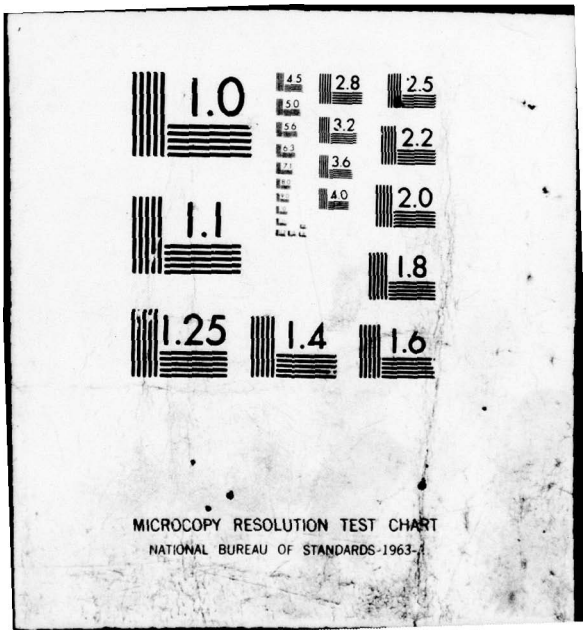
1.0
1.1
1.25
1.4
1.6
1.8
2.0
2.2
2.5
2.8
3.2
3.6
4.0
4.5
5.0
5.6
6.3
7.1
MICROCOPY RESOLUTION TEST CHART
NATIONAL BUREAU OF STANDARDS-1963-A

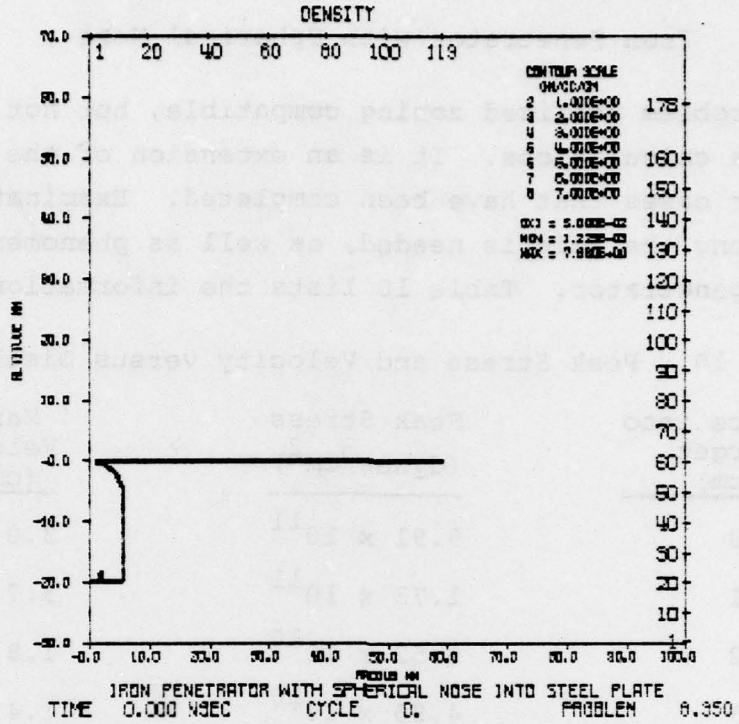

Figure 72. Density Contours at 0.0 μs

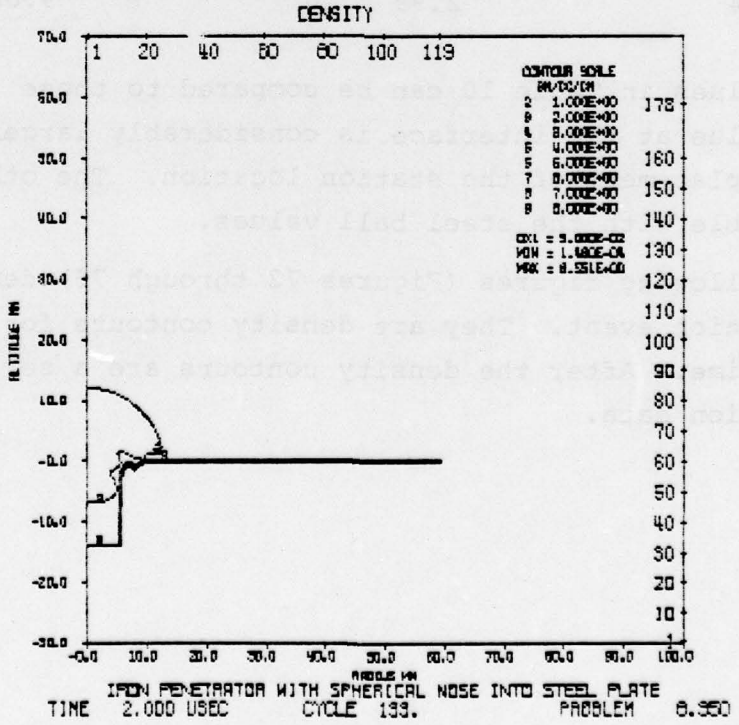

Figure 73. Density Contours at 2.0 μs

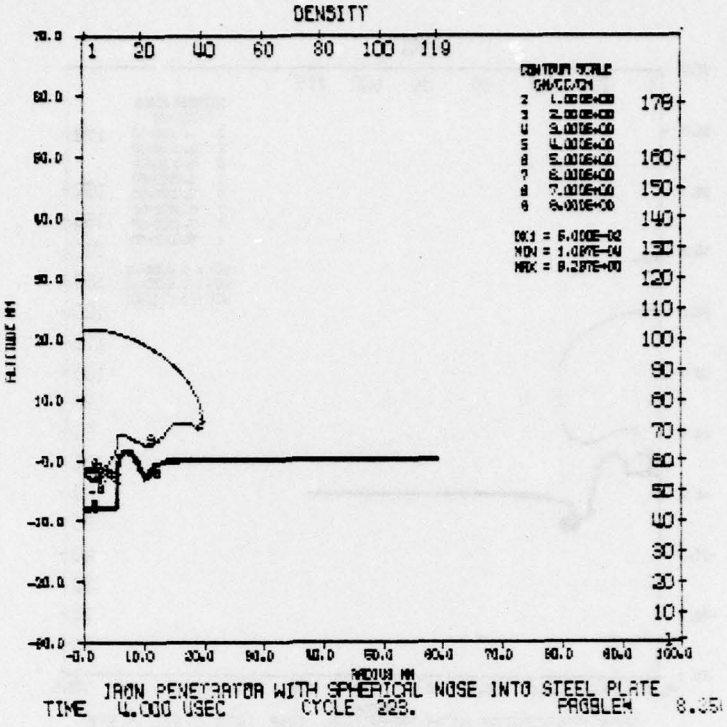

Figure 74. Density Contours at 4.0 µs

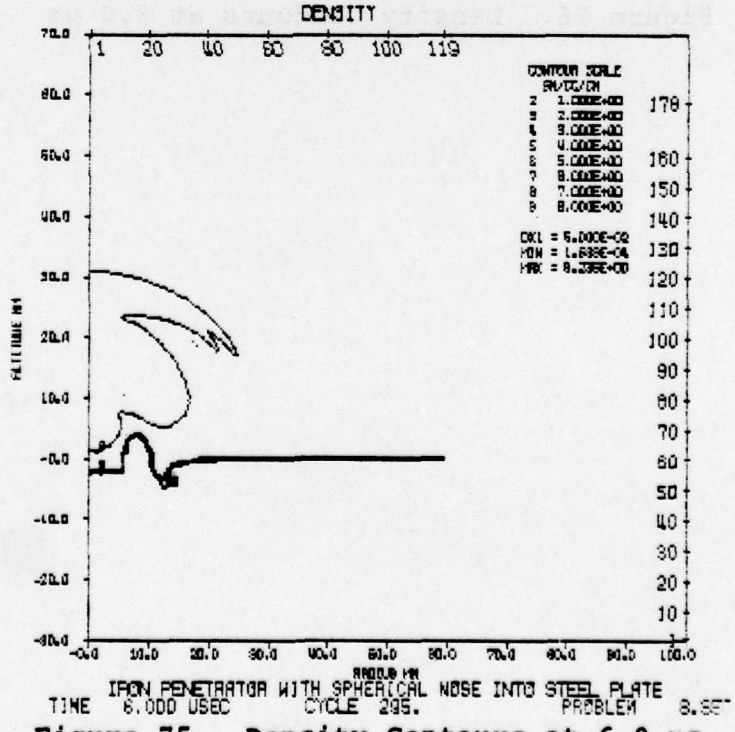

Figure 75. Density Contours at 6.0 µs

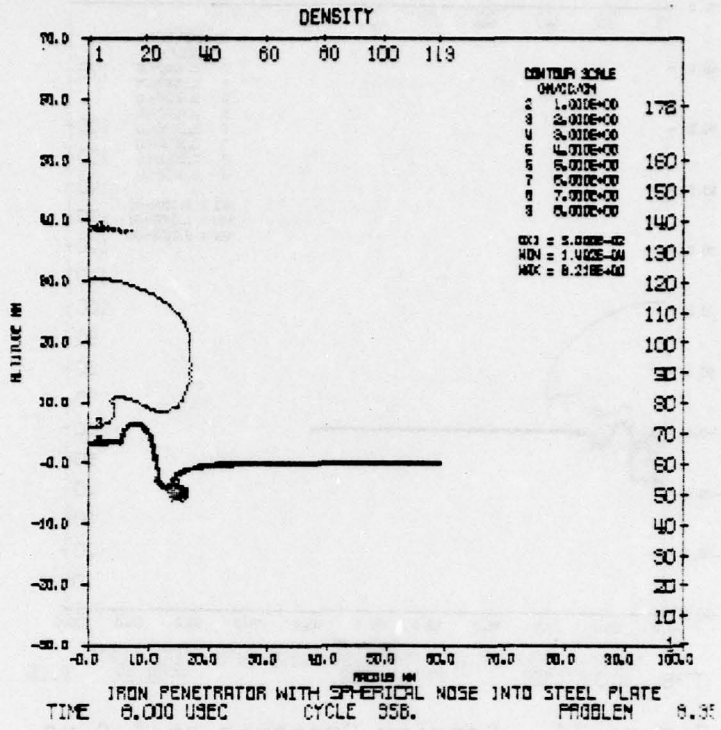

Figure 76. Density Contours at 8.0 µs

The following figures are examples of station plots for this problem. Figures 77 through 94 indicate peak stress, density, total stress, and the material motion, i.e., velocity of the material. Figures 77 through 79 show a station located within the penetrator. Station 2 (Figure 78) indicates that the penetrator does not show any evidence of slowing until the shock wave has rebounded from the interfaces of the target penetration and reaches the midpoint of the penetration. This occurs at approximately 1.2 μs. By that time, the midpoint has moved 1.21 μs x $3 \cdot 10^5$ cm/s, or 0.36 cm closer to the interface. Before the shock rebounds from the back surface of the penetrator and arrives back at midpoint, it encounters an increase in velocity at the same time the midpoint of the penetrator meets the arrival penetrator-target interface about 3 μs.

Figures 80 through 82 are plots of the station data at the penetrator-target interface. A maximum peak stress of almost a megabar in pressure is attained. At the same time, an increase in density to $\rho = 10.1$ is achieved.

Station 4 (Figures 83 through 85) is located 1 cm from the interface inside the target. The stress wave passes that point at approximately 2 μs. That indicates a speed coincident with the sound of speed of the material. The stress wave maintains its basic shape as it propagates through the steel target. No alteration of the main pulse occurs as a result of rebounding waves from the end of the penetrator. Also, since both target and penetrator are steel, there are no waves associated with a density impedance. There are, however, secondary waves that can be attributed to reflections from the interface and the end of the penetrator. Station 5 is located 2 cm from the interface, and stations 6 and 7 are at 3 and 4 cm, respectively.

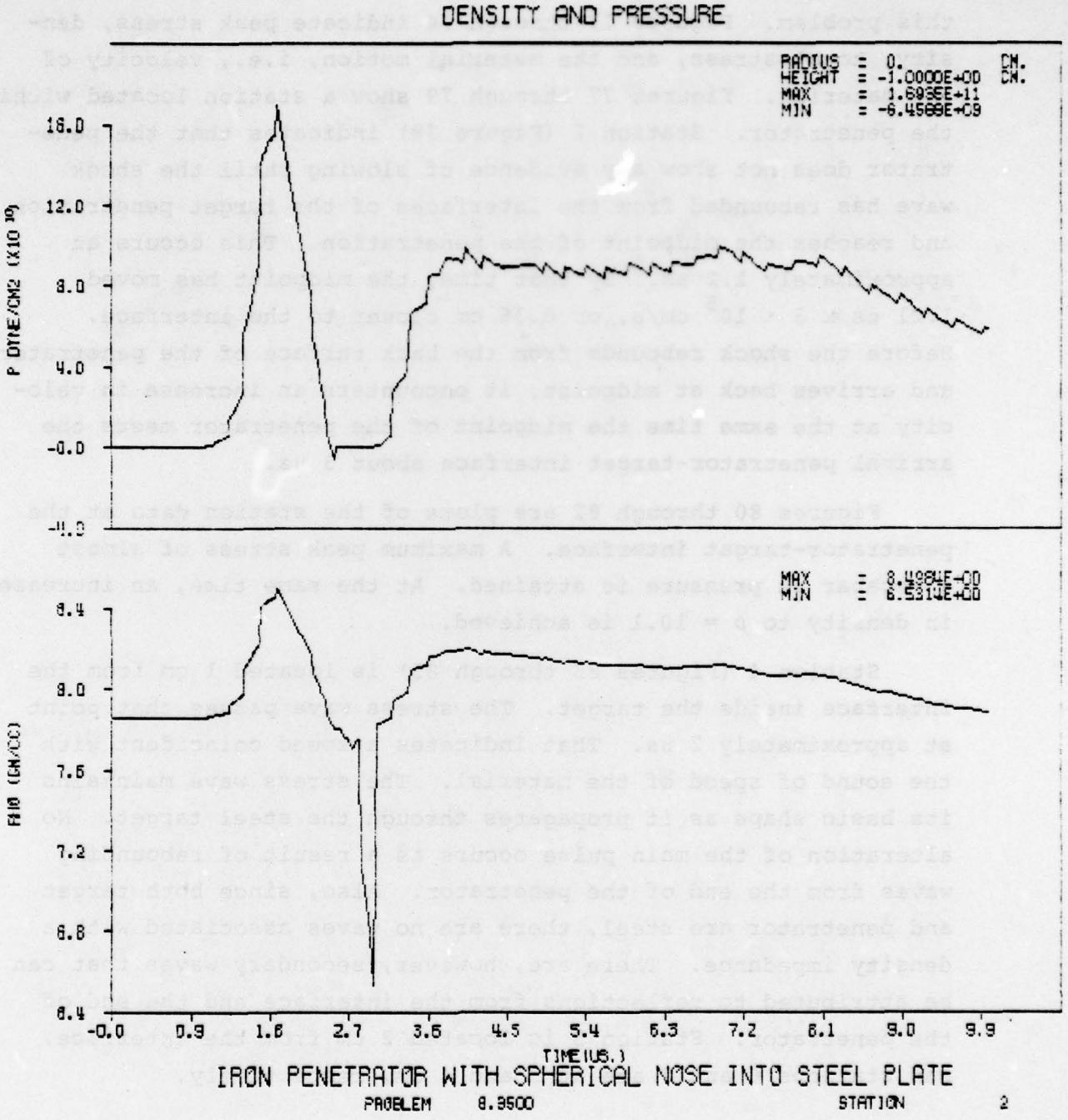

Figure 77. Density and Pressure Histograms for Station 2

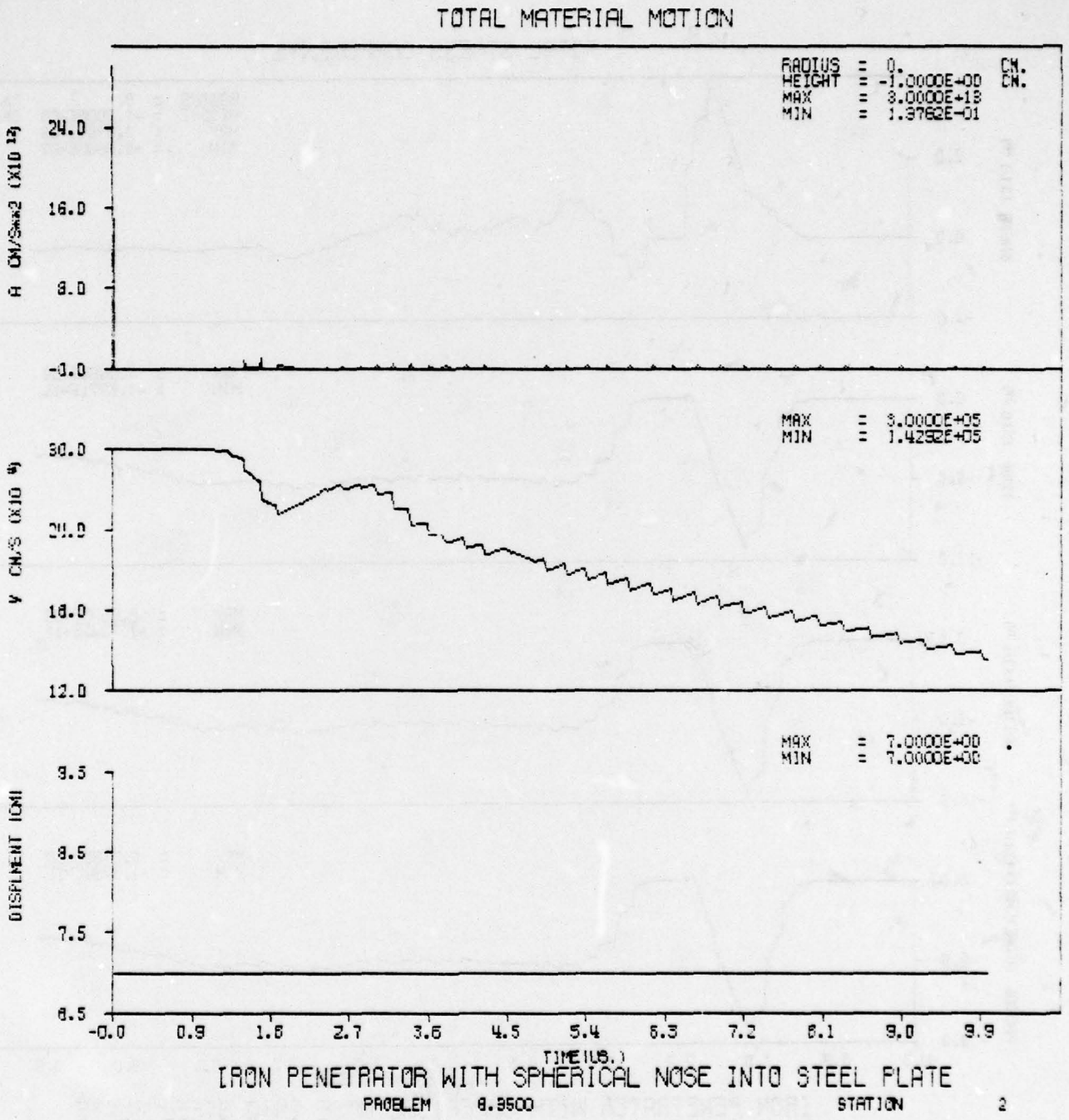

Figure 78. Material Motion Histograms for Station 2

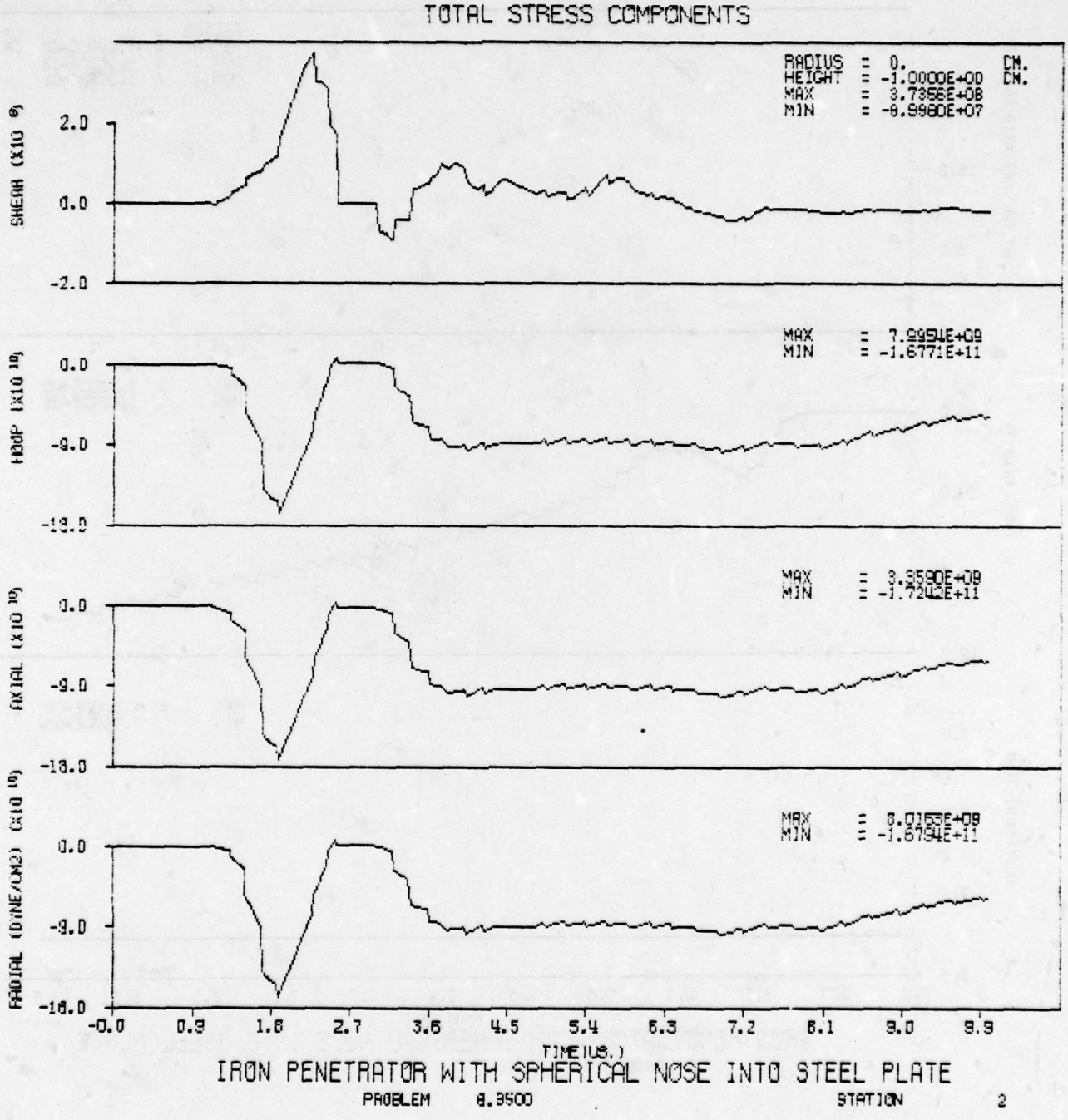

Figure 79. Stress Histograms for Station 2

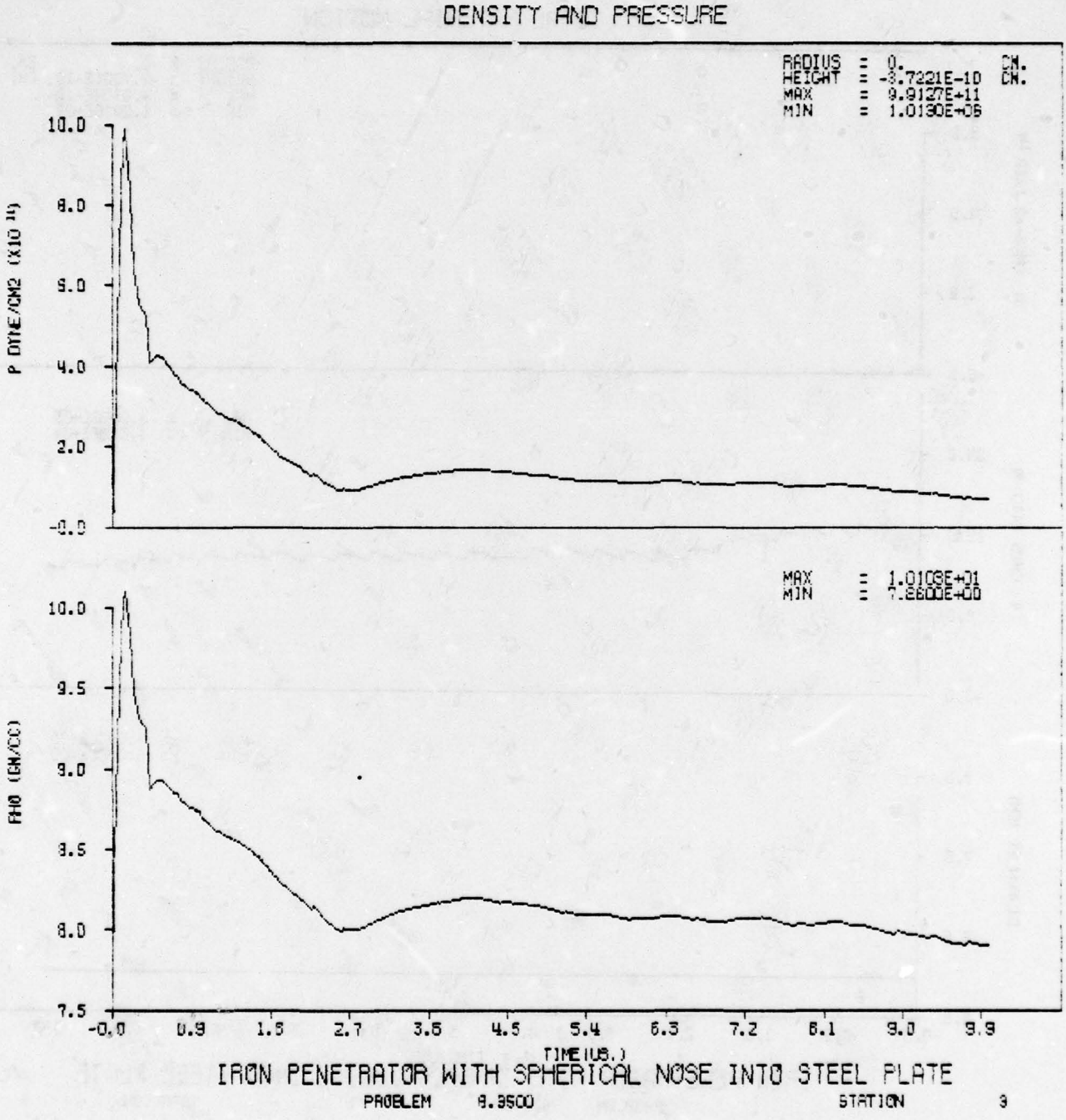

Figure 80. Density and Pressure Histograms for Station 3

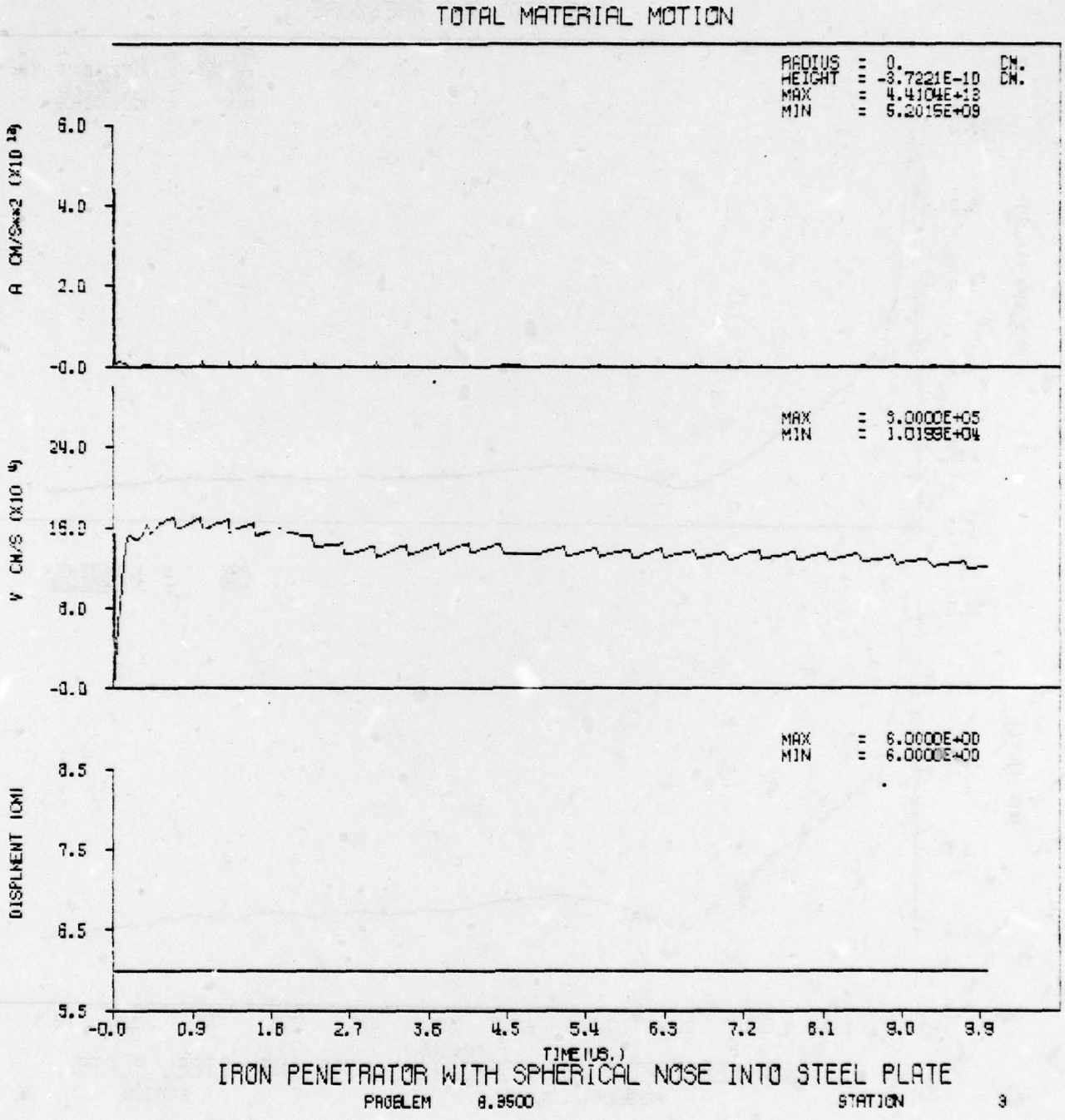

Figure 81. Total Motion Histograms for Station 3

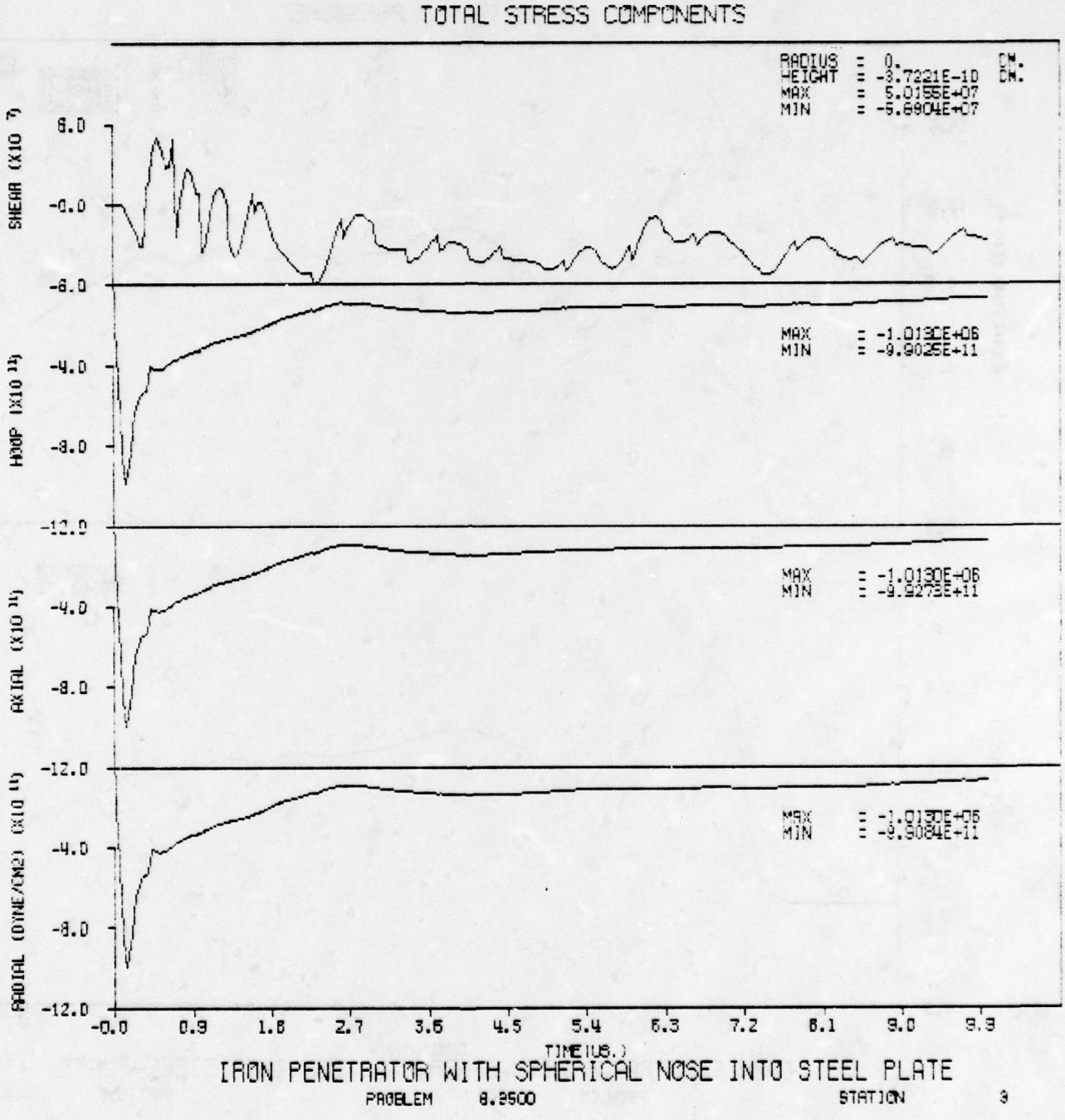

Figure 82. Stress Histograms for Station 3

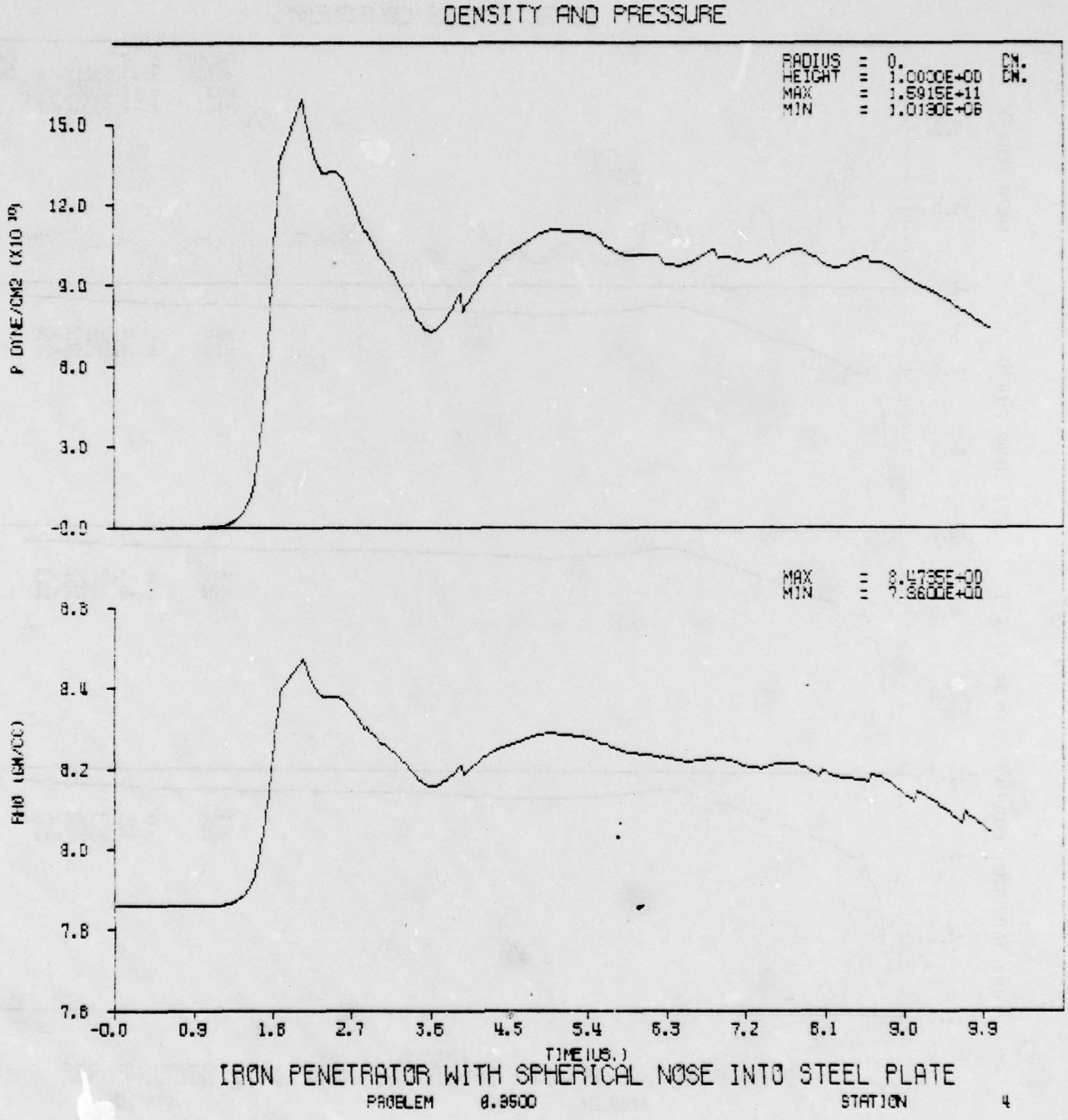

Figure 83. Density and Pressure Histograms for Station 4

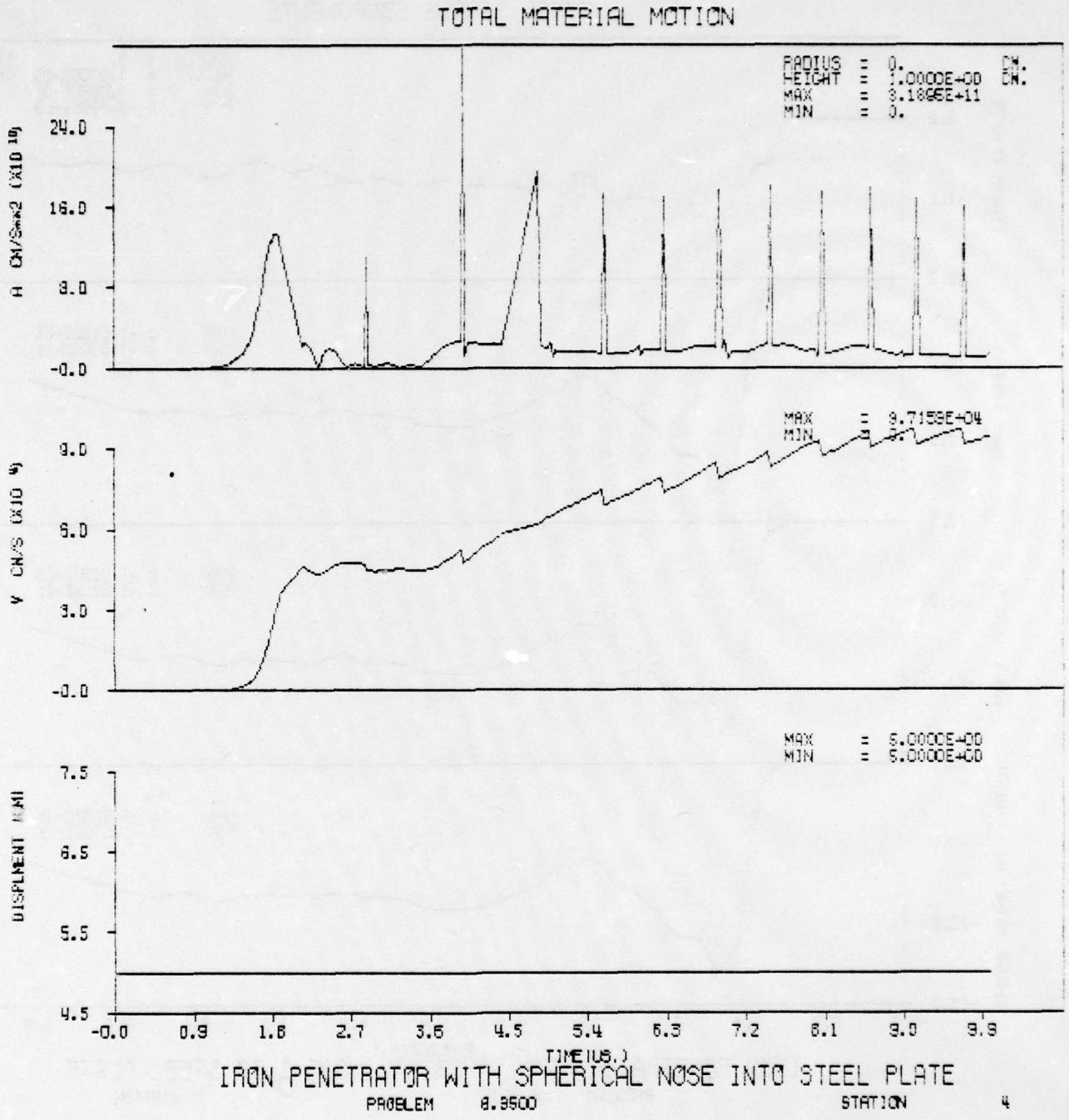

Figure 84. Total Motion Histograms for Station 4

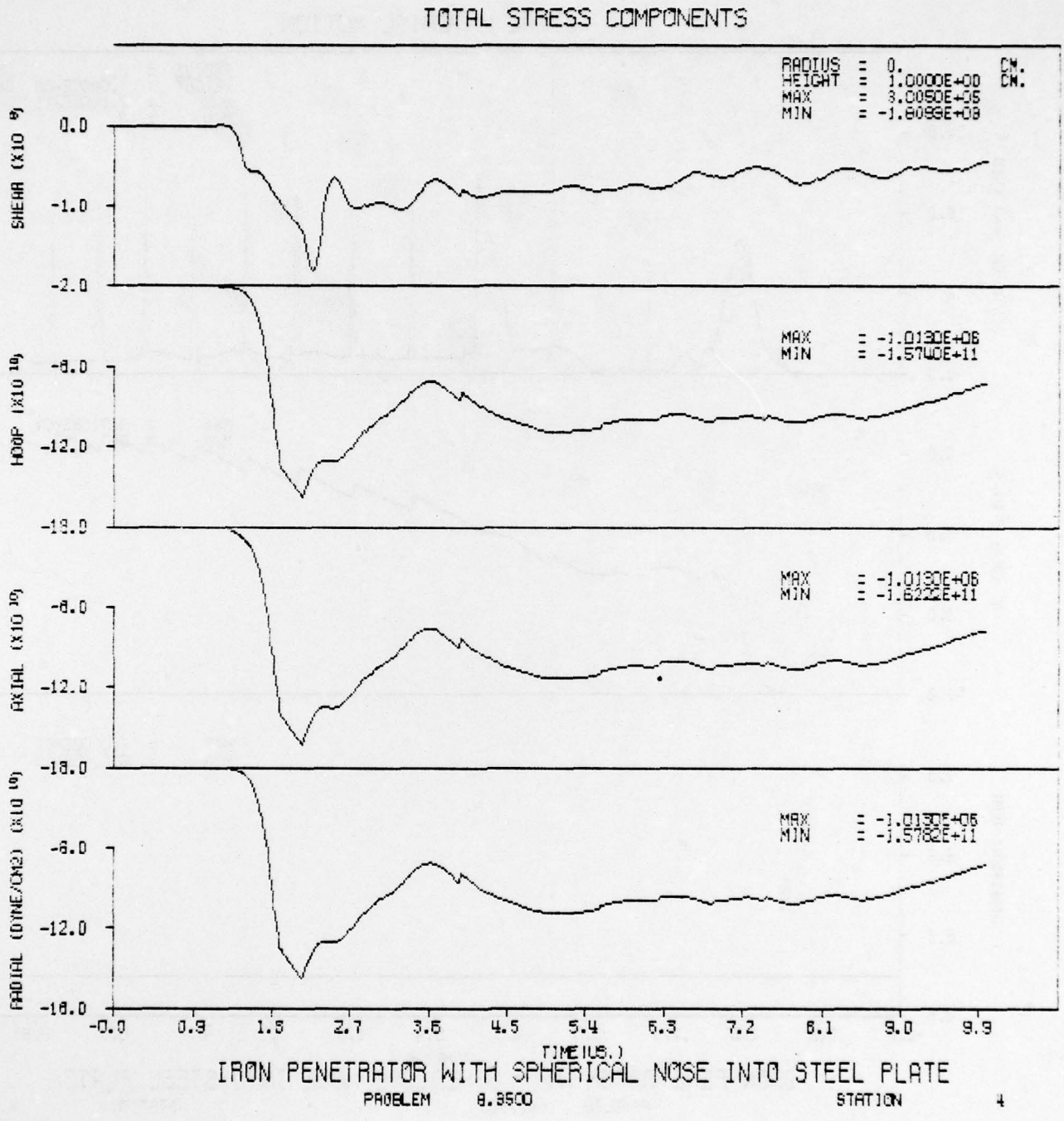

Figure 85. Stress Histograms for Station 4

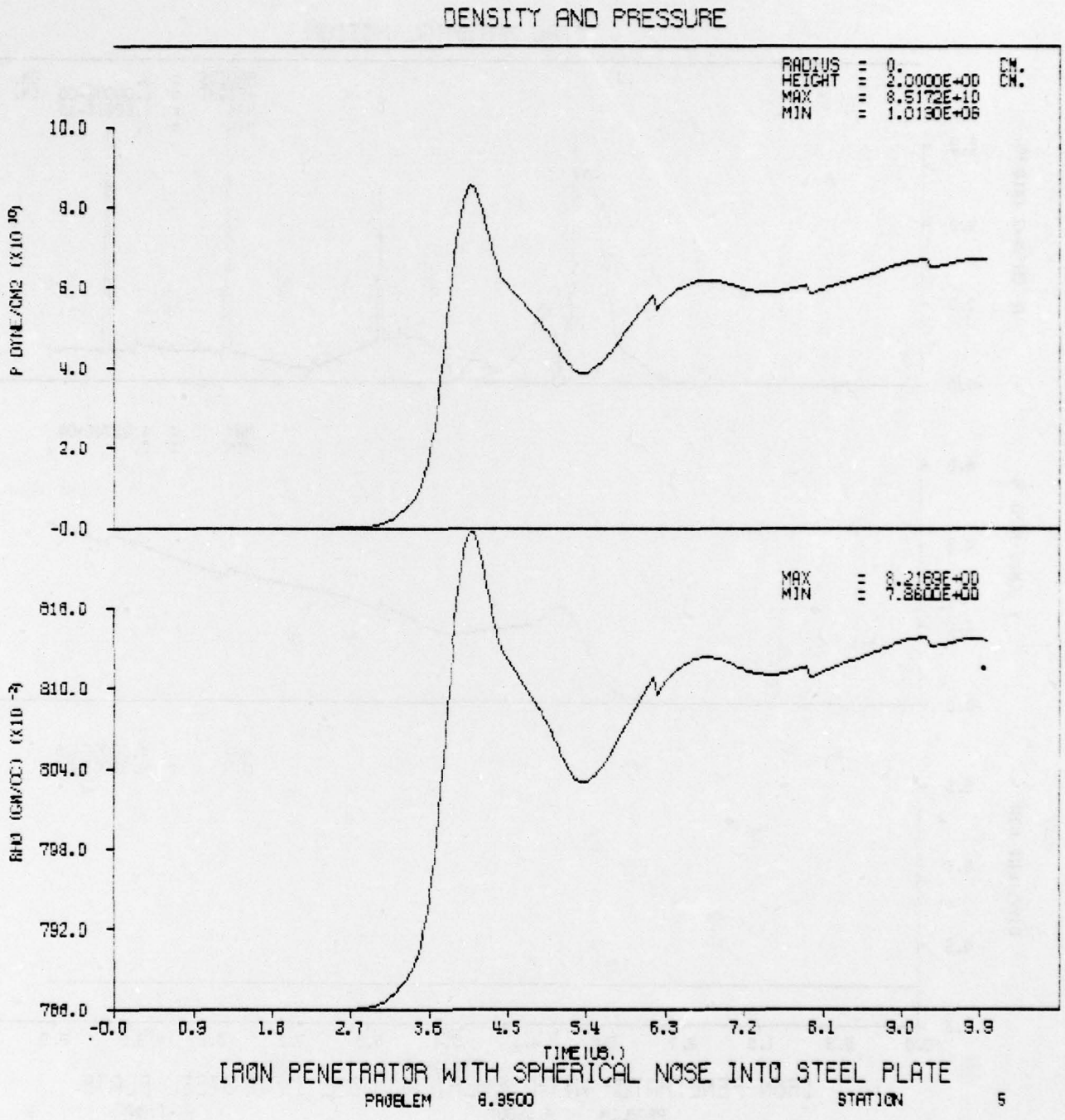

Figure 86. Density and Pressure Histograms for Station 5

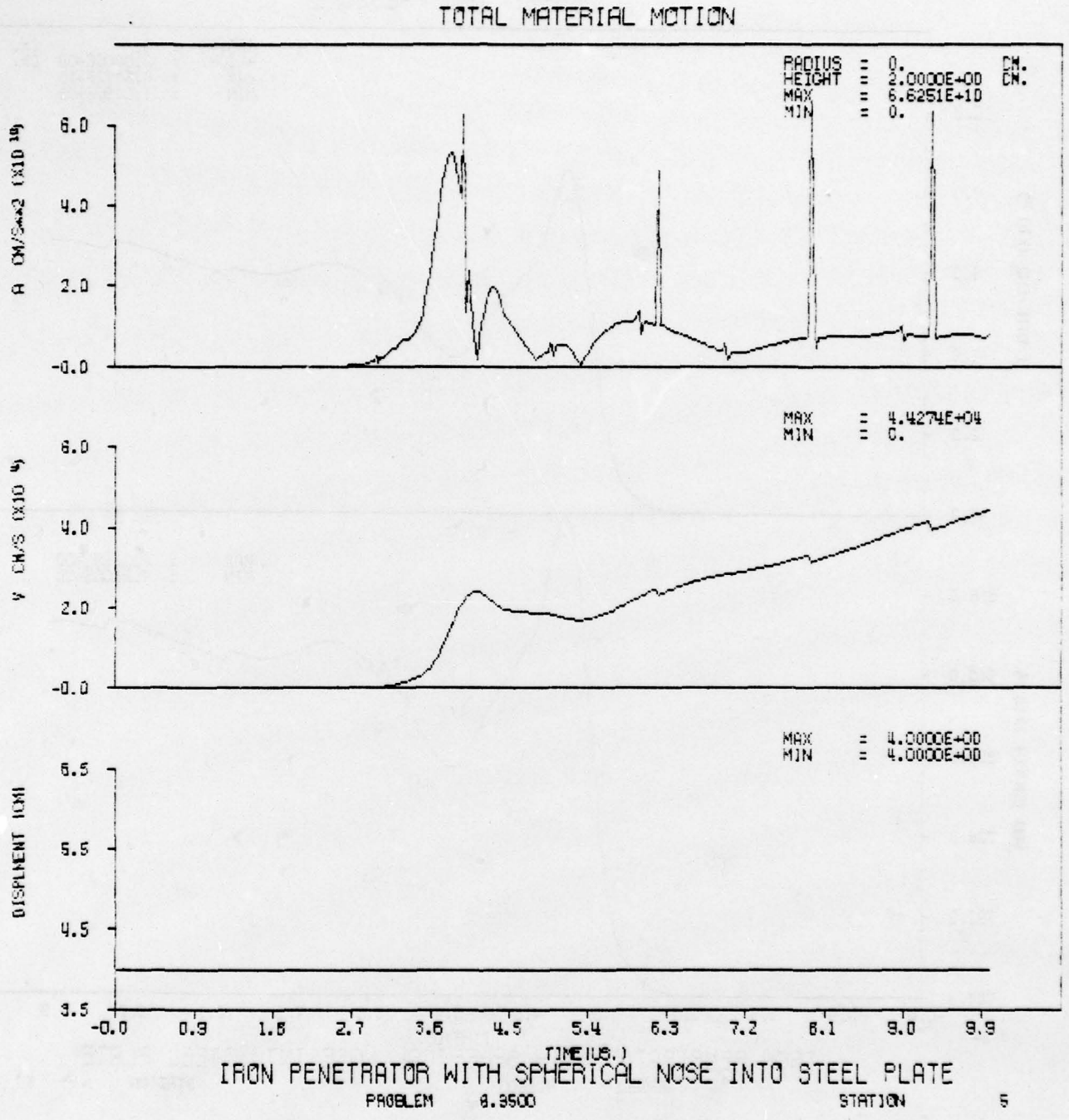

Figure 87. Total Motion Histograms for Station 5

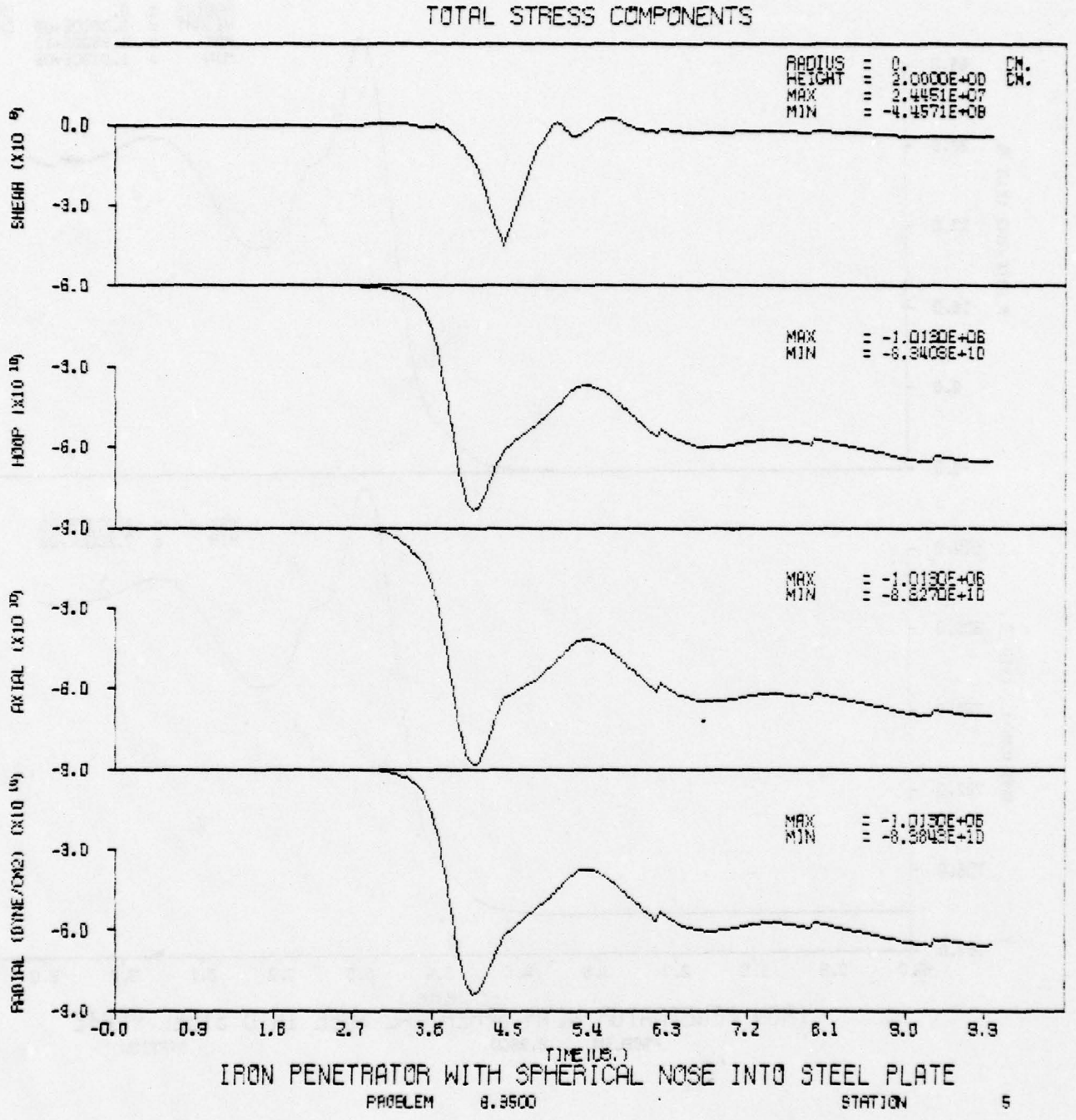

Figure 88. Stress Histograms for Station 5

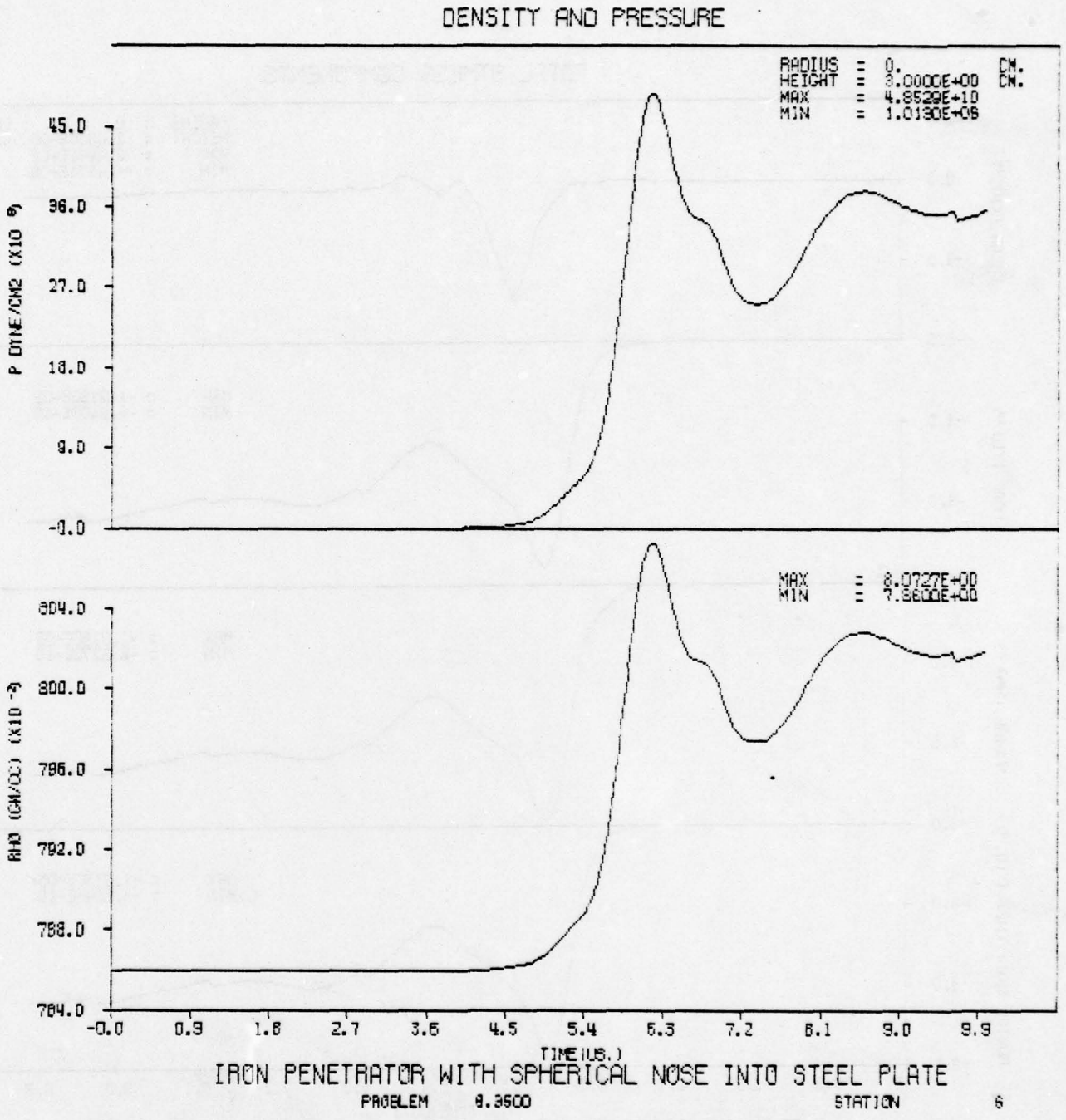

Figure 89. Density and Pressure Histograms for Station 6

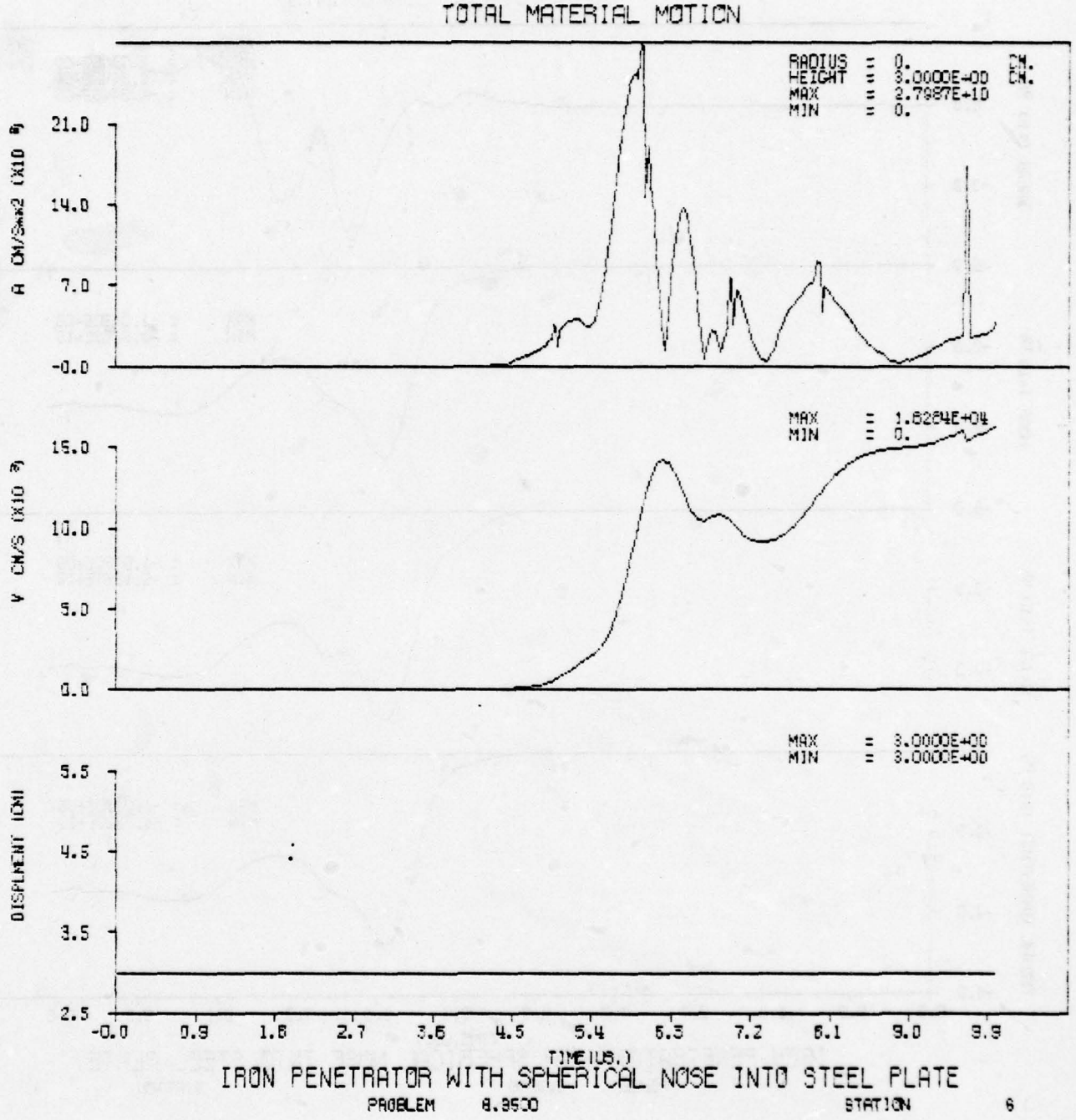

Figure 90. Total Motion Histograms for Station 6

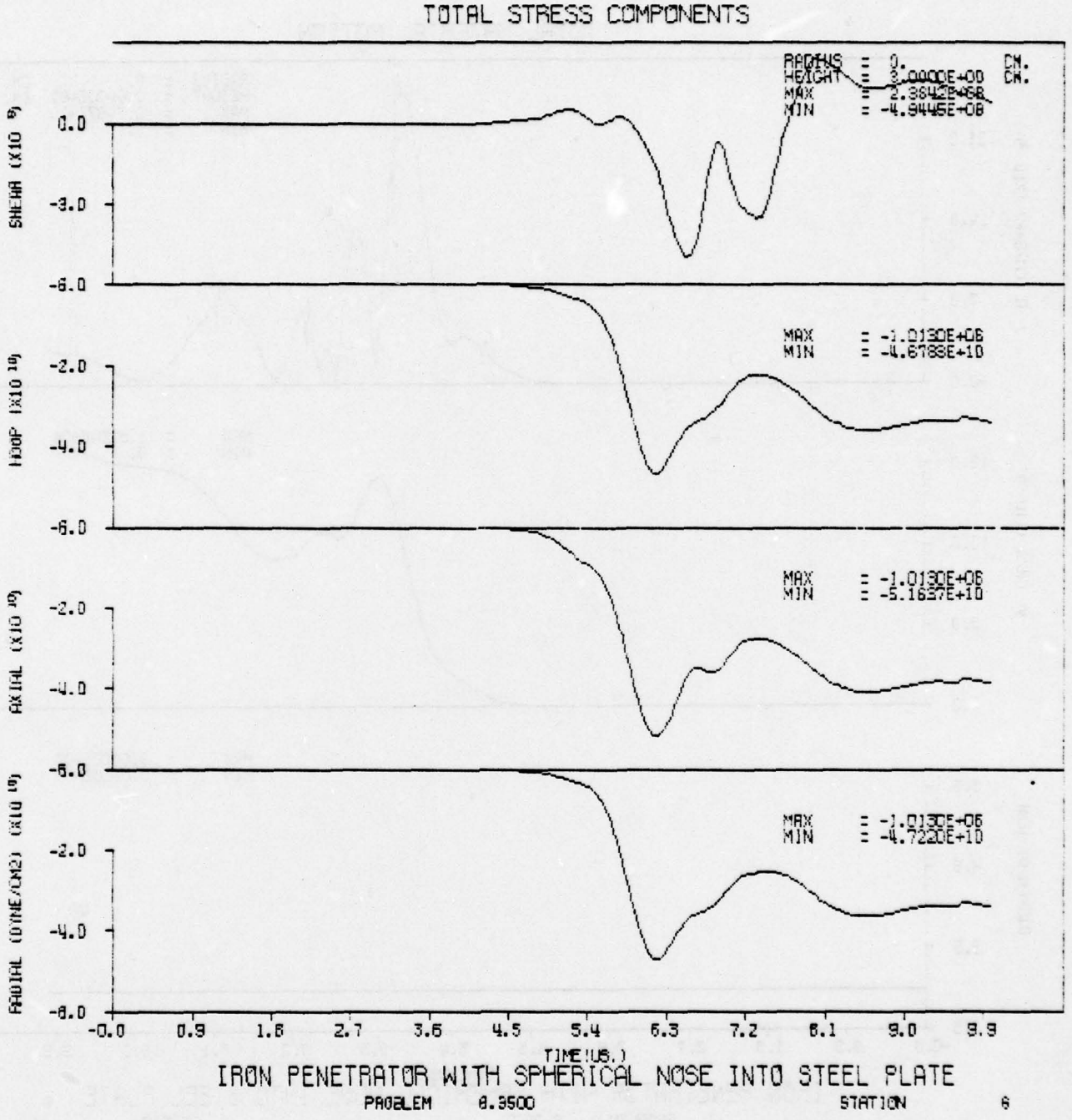

Figure 91. Stress Histograms for Station 6

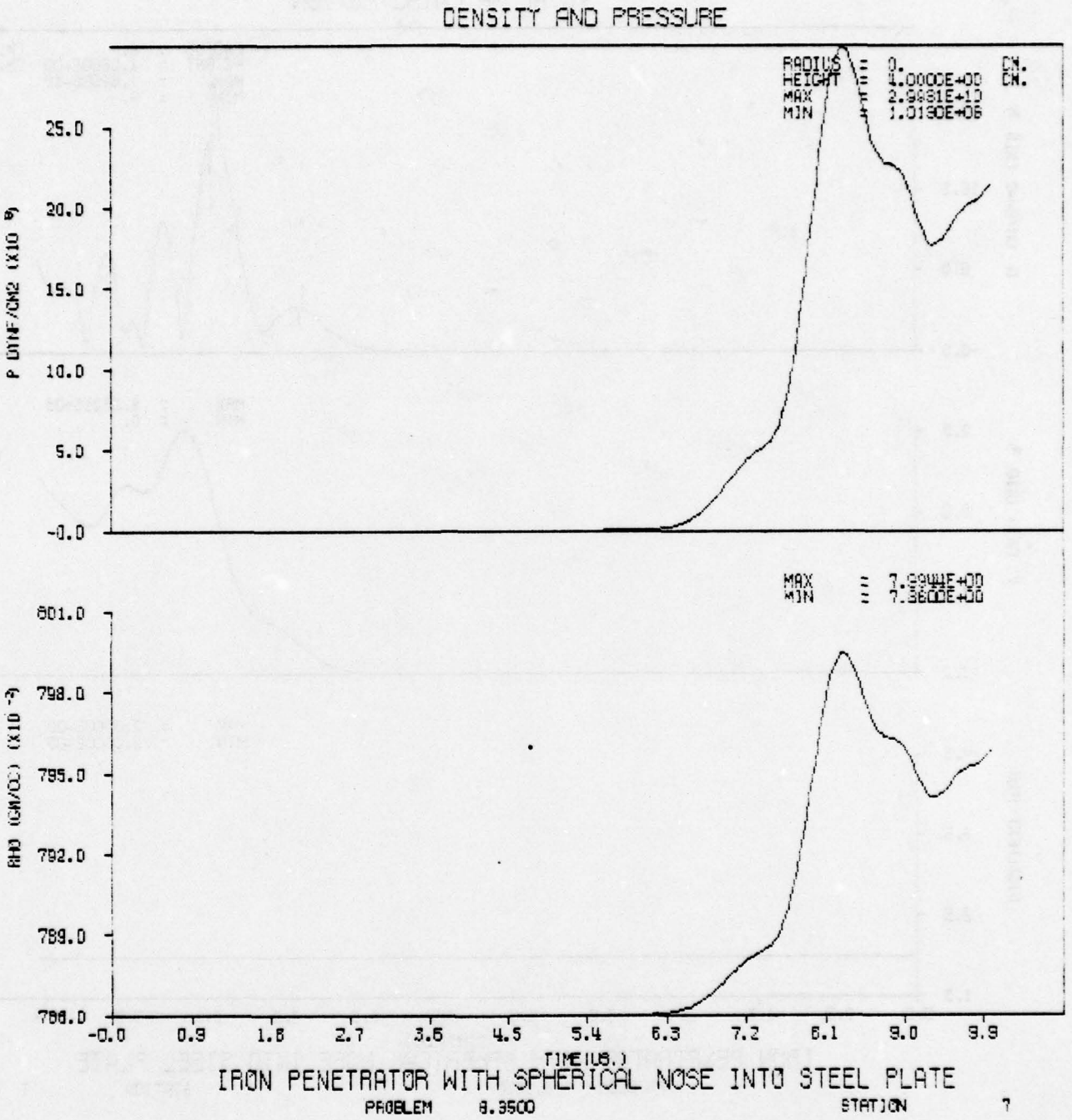

Figure 92. Density and Pressure for Station 7

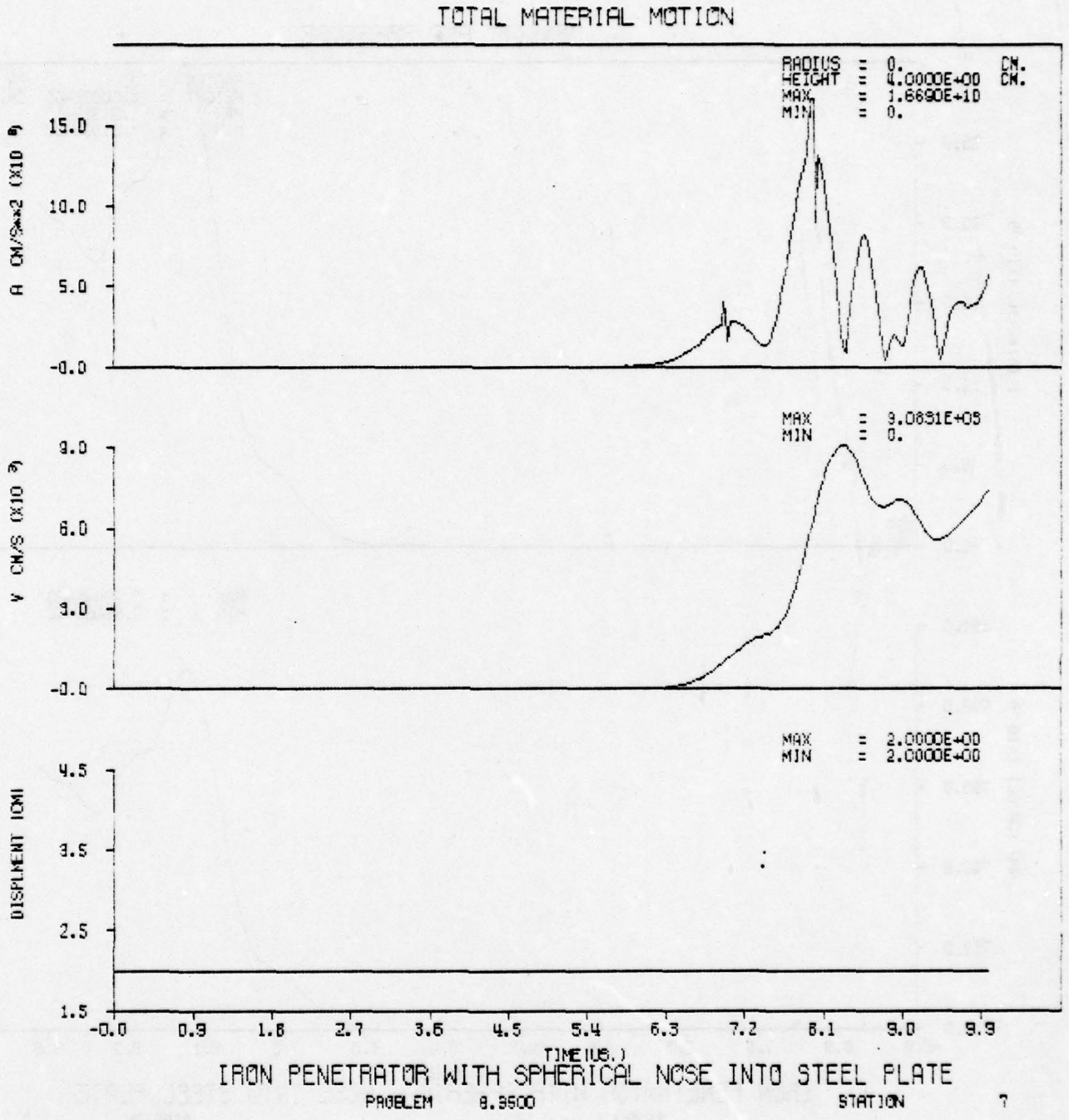

Figure 93. Total Motion Histograms for Station 7

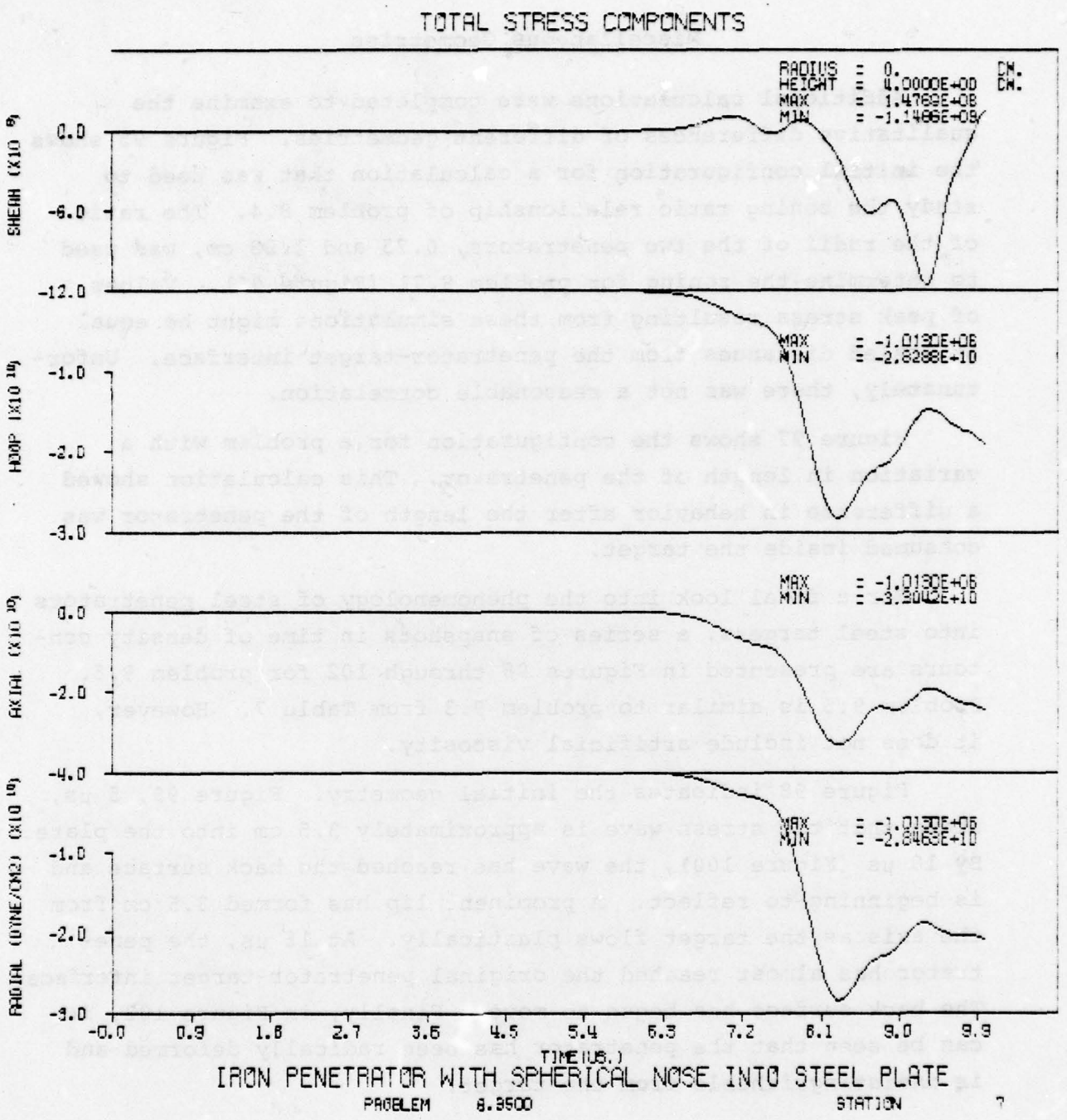

Figure 94. Stress Histograms for Station 7

Miscellaneous Geometries

Additional calculations were completed to examine the qualitative differences of different geometries. Figure 95 shows the initial configuration for a calculation that was used to study the zoning ratio relationship of problem 8.4. The ratio of the radii of the two penetrators, 0.75 and 1.28 cm, was used to determine the zoning for problem 8.71 (Figure 96). Values of peak stress resulting from these simulations might be equal at scaled distances from the penetrator-target interface. Unfortunately, there was not a reasonable correlation.

Figure 97 shows the configuration for a problem with a variation in length of the penetrator. This calculation showed a difference in behavior after the length of the penetrator was consumed inside the target.

For a final look into the phenomenology of steel penetrators into steel targets, a series of snapshots in time of density contours are presented in Figures 98 through 102 for problem 9.5. Problem 9.5 is similar to problem 9.3 from Table 7. However, it does not include artificial viscosity.

Figure 98 indicates the initial geometry. Figure 99, 5 μs, shows that the stress wave is approximately 3.5 cm into the plate. By 10 μs (Figure 100), the wave has reached the back surface and is beginning to reflect. A prominent lip has formed 3.5 cm from the axis as the target flows plastically. At 15 μs, the penetrator has almost reached the original penetrator-target interface. The back surface has begun to move. Finally, in Figure 102, it can be seen that the penetrator has been radically deformed and is indistinguishable from the target.

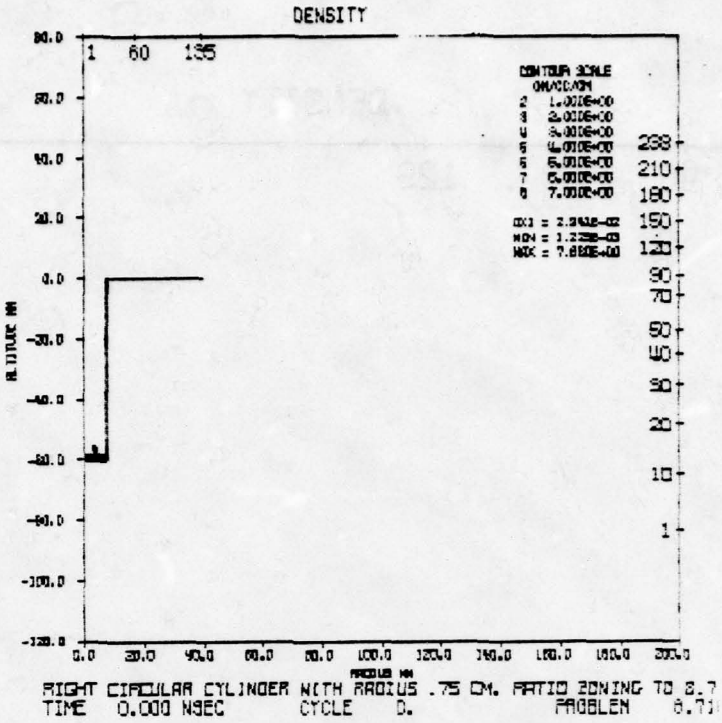

Figure 95. Density Contours for 0.0 μs

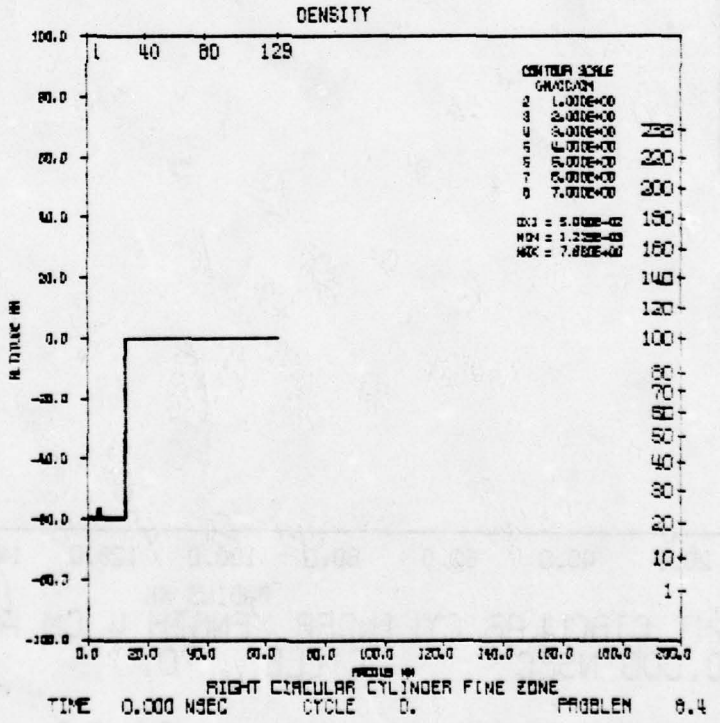

Figure 96. Density Contours for 0.0 μs

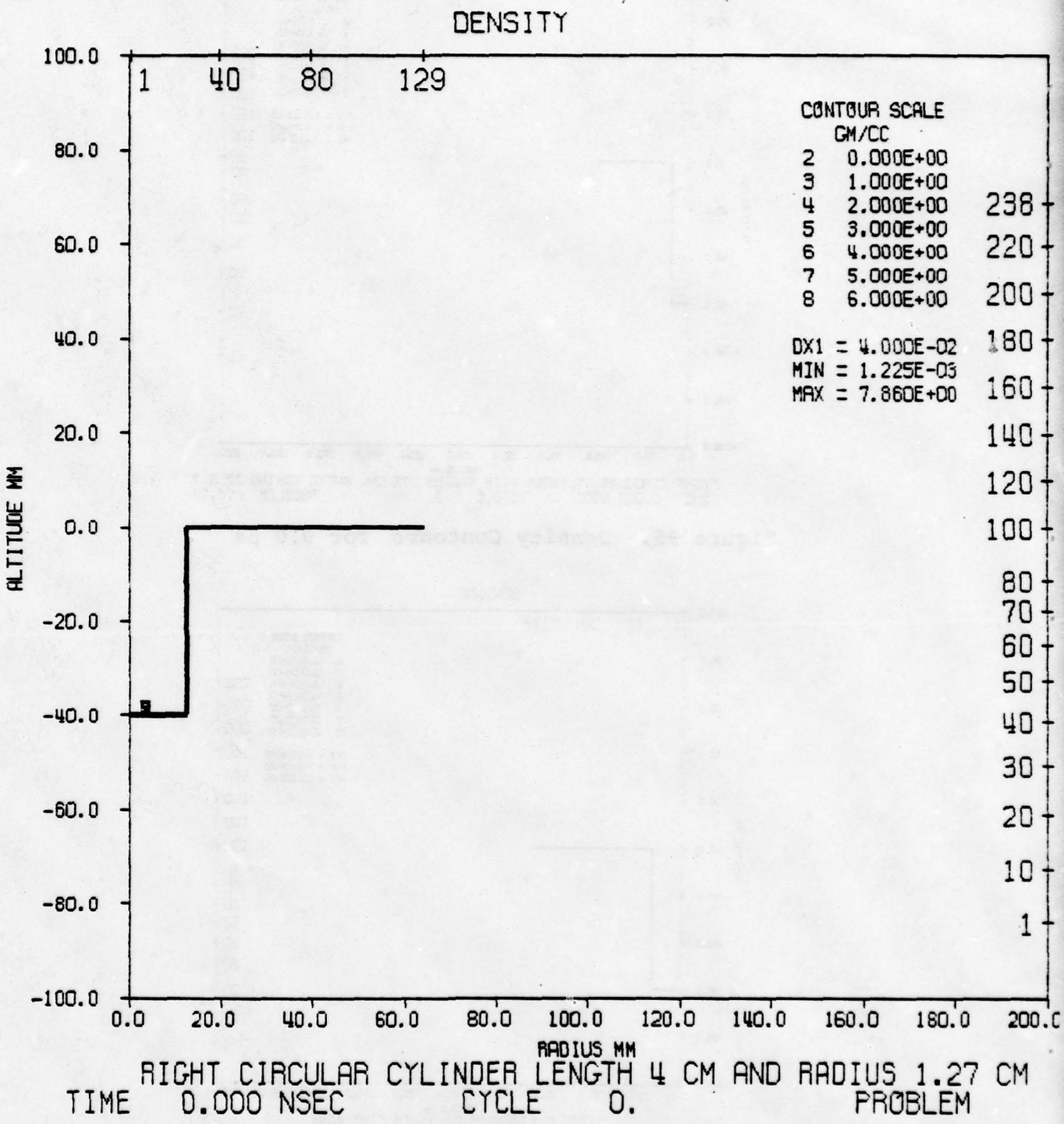

Figure 97. Density Contours for 0.0 μs

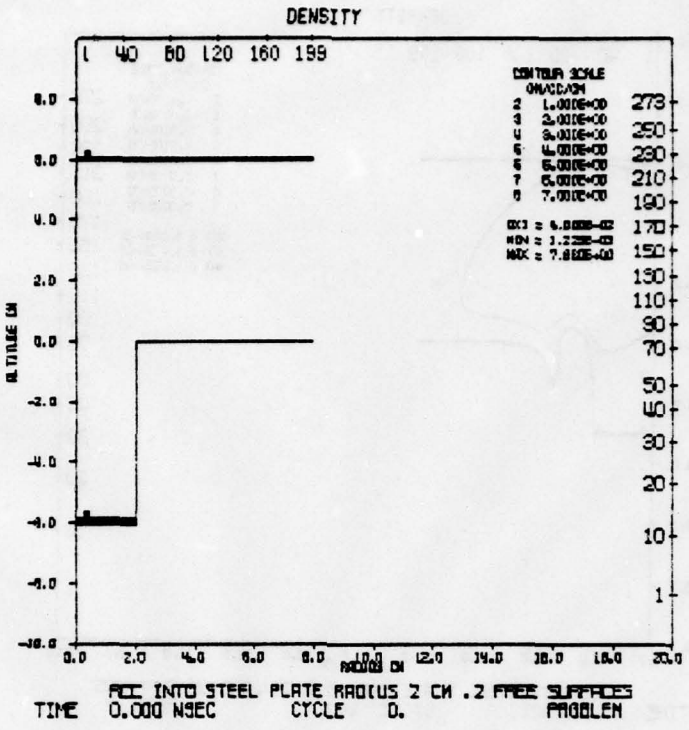

Figure 98. Density Contours for 0.0 μs

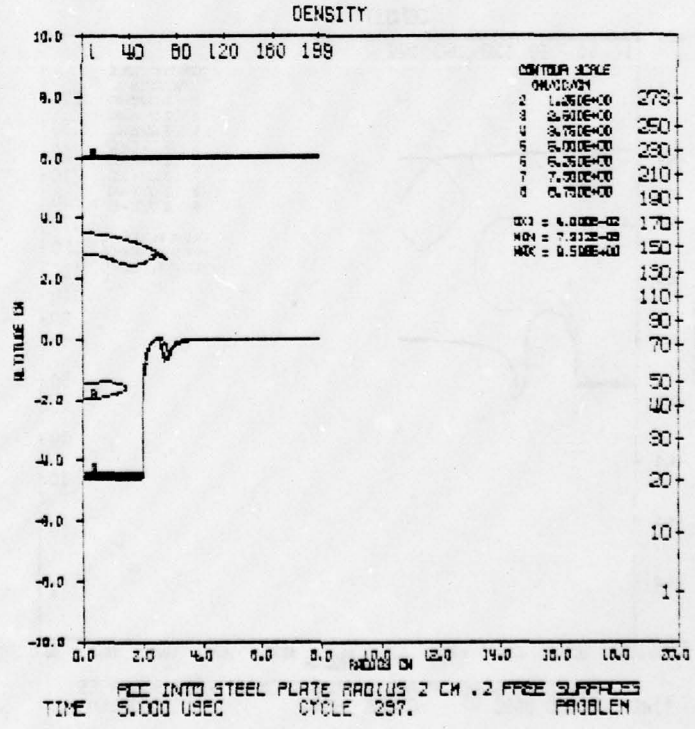

Figure 99. Density Contours for 5.0 μs

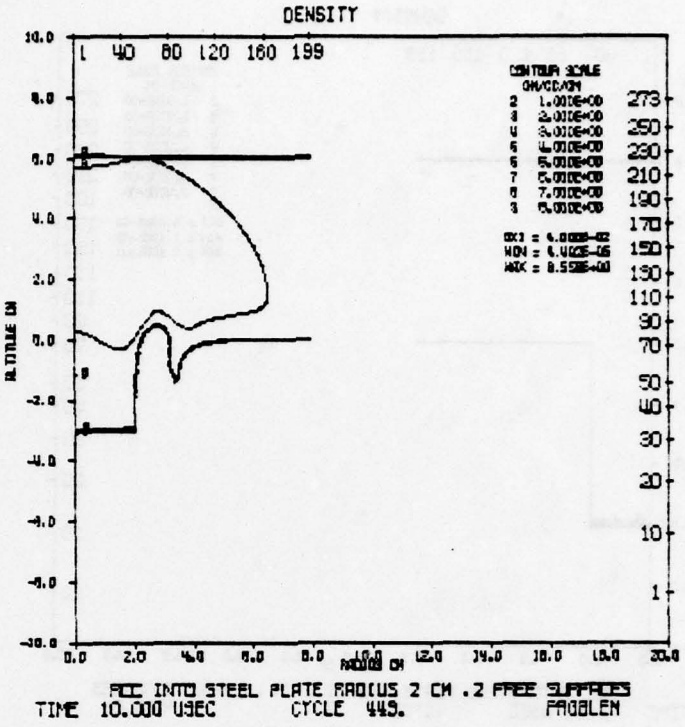

Figure 100. Density Contours for 10.0 μs

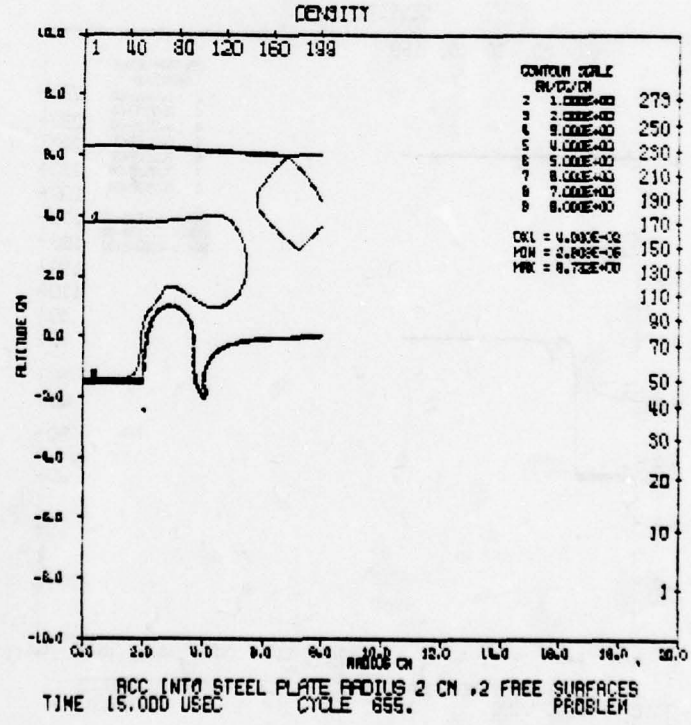

Figure 101. Density Contours for 15.0 μs

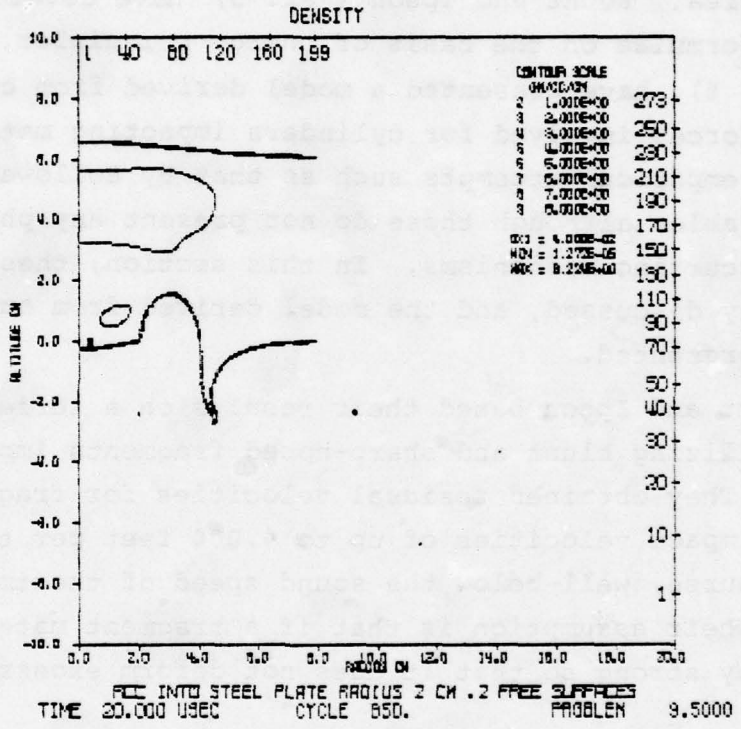

Figure 102. Density Contours for 20.0 μs

SECTION VI

PREDICTIVE MODELING

Obtaining a predictive model of penetration from the numerical simulations is highly desirable. If one can predict, through simple models the important physical parameters as a function of space and time, expensive and time consuming calculations will not be necessary. Several attempts have been made in this area. Recht and Ipson (Ref. 5) have developed simplified formulae on the basis of energy principles. Hayda et al. (Ref. 6), have presented a model derived from considering the dynamic forces involved for cylinders impacting metallic targets. Numerous empirical attempts such as that by Holloway et al. (Ref 7), are available; although these do not present any physical insight to the occurring mechanisms. In this section, these models will be briefly discussed, and the model derived from out calculations will be presented.

Recht and Ipson based their results on a series of experiments utilizing blunt and sharp-nosed fragments impacting thin plates. They obtained residual velocities for fragments having initial impact velocities of up to 4,000 feet per second. This is, of course, well below the sound speed of the impact material, steel. Their assumption is that if a fragment material is relatively strong so that it does not deform excessively, and

---

5. Recht, R. F., and T. W. Ipson, "Ballistic Perforation Dynamics," Journal Applied Mechanics, Vol. 30, pp 384-390, Sept 1963.
6. Hayda et al., Combined Theoretical and Experimental Investigation of Armor Penetration Mechanics, AFATL TR-70-78, Air Force Armament Laboratory, Eglin AFB, Fl., Aug 1970.
7. Holloway, G., M. Danish, and J. Matts, Penetration Relations for Tungsten Alloy Fragments Versus Selected Target Materials Army Ballistic Research Laboratory, Aberdeen, Md., March 1978.

the plate is relatively thin,

$$\frac{\text{PLATE THICKNESS}}{\text{FRAGMENT LENGTH}} < \frac{1}{2} \; ; \; \frac{\text{PLATE THICKNESS}}{\text{DIAMETER FRAGMENT}} < \frac{1}{2}$$

a plate plug will normally be ejected. This statement restricts the range of validity of their model. It relies heavily upon what is termed punch press. Acceleration of material is virtually absent and only geometry and strength of materials are important. The authors describe the penetration process as a two-step phenomenon. First, the fragment or penetrator experiences rapid deceleration and acceleration of the plate-plug. Pressures at the interface are high enough to cause deformation at the interface and shear boundary. The second step is the punch press idea mentioned above, in which the plug is sheared from the plate. The kinetic energy of the penetrator and the plate-plug provide the necessary energy to overcome the shear resistance. As one might expect, the analytical models they propose lose validity as the penetrator loses its integrity.

Additional work in the plate-plug regime was done by Hayda and others in 1970. In their work for the AFATL, they investigated penetrator velocities from threshold ballistic limits up to 1.2 km/sec. They, too, have derived analytical formulae for residual velocities and minimum perforation velocities.

Throughout the work reported here, a different regime has been investigated. One is interested in not only penetration through various thicknesses of materials but in doing a lot of damage to the target and whatever might be behind the target. One is compelled to choose penetrators with impact velocities that place the penetration process into the hydrodynamic regime where strength of materials becomes less important, where the initial stresses upon impact are many orders of magnitude above the yield strength of the materials involved. In fact, one wants the material to deform substantially and flow plastically throughout the penetration event. Quantifying this regime is an important

task to be performed. Of course, the one parameter that is usually cited is the impact velocity. The expectation is that impact speeds at the sound speed or greater of the target material will qualify the penetration process as hydrodynamic. This conclusion would follow from the physics of wave propagation which would predict strong shocks being generated that would overcome the inherent material strength of the metal. However, extremely high stresses generated at the penetrator-target interface produce very large pressures that give rise to strong shock waves moving out through the target material. An interesting plot to examine is the relationship of pressure versus impact velocity for a given penetration geometry. Figure 103 illustrates the initial peak stress at the penetrator target interface as a function of impact velocity for a copper penetrator impacting a steel plate. The peak stresses follow a linear curve until a velocity of 3,000 to 4,000 meters per second is reached. At which time, the slope becomes more pronounced. This change in slope signals the transition to the hydrodynamic flow. In Figure 104, the average speed of a copper penetrator (3 cm in length) has been plotted as a function of depth into a steel plate. Average speed is simply the speed at the midpoint of the remaining penetrator body. Initial velocities of 5, 3, 2, and 1 km/s are shown. A pronounced difference in curves can be observed as one proceeds to higher impact velocities. The initially steeper slopes of the 2, 3, and 5 km/s curves have to do with the sound speed of the penetrator and the velocity of impact. The tail end of the penetrator does not know what the front end has experienced until the stress wave reaches it. Meanwhile, the penetrator continues to move into the plate at a speed that can be approximated by the following formula.*

---

*Matuska, Dan, private communication, August 1978.

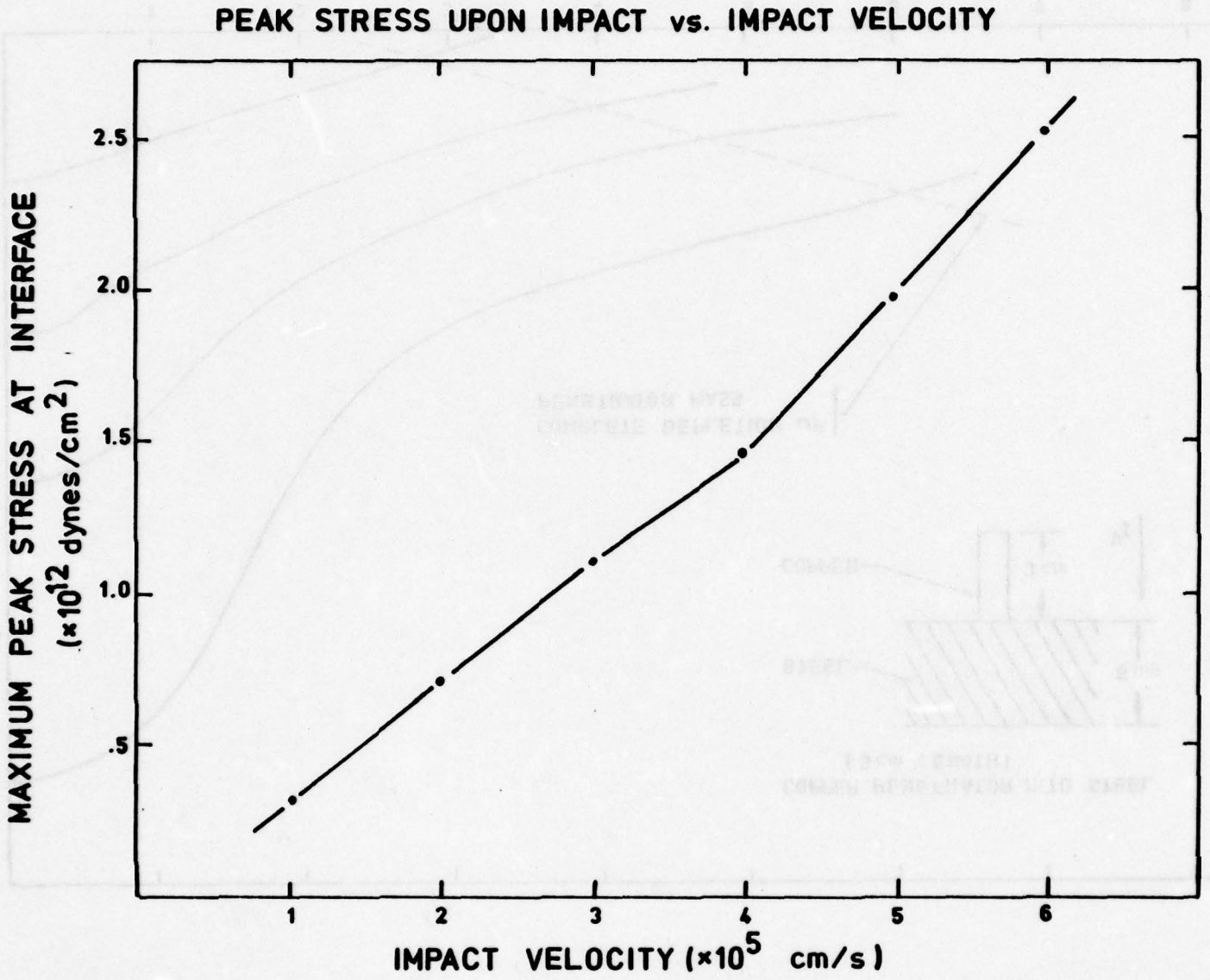

Figure 103. Copper Penetrator into Steel Target

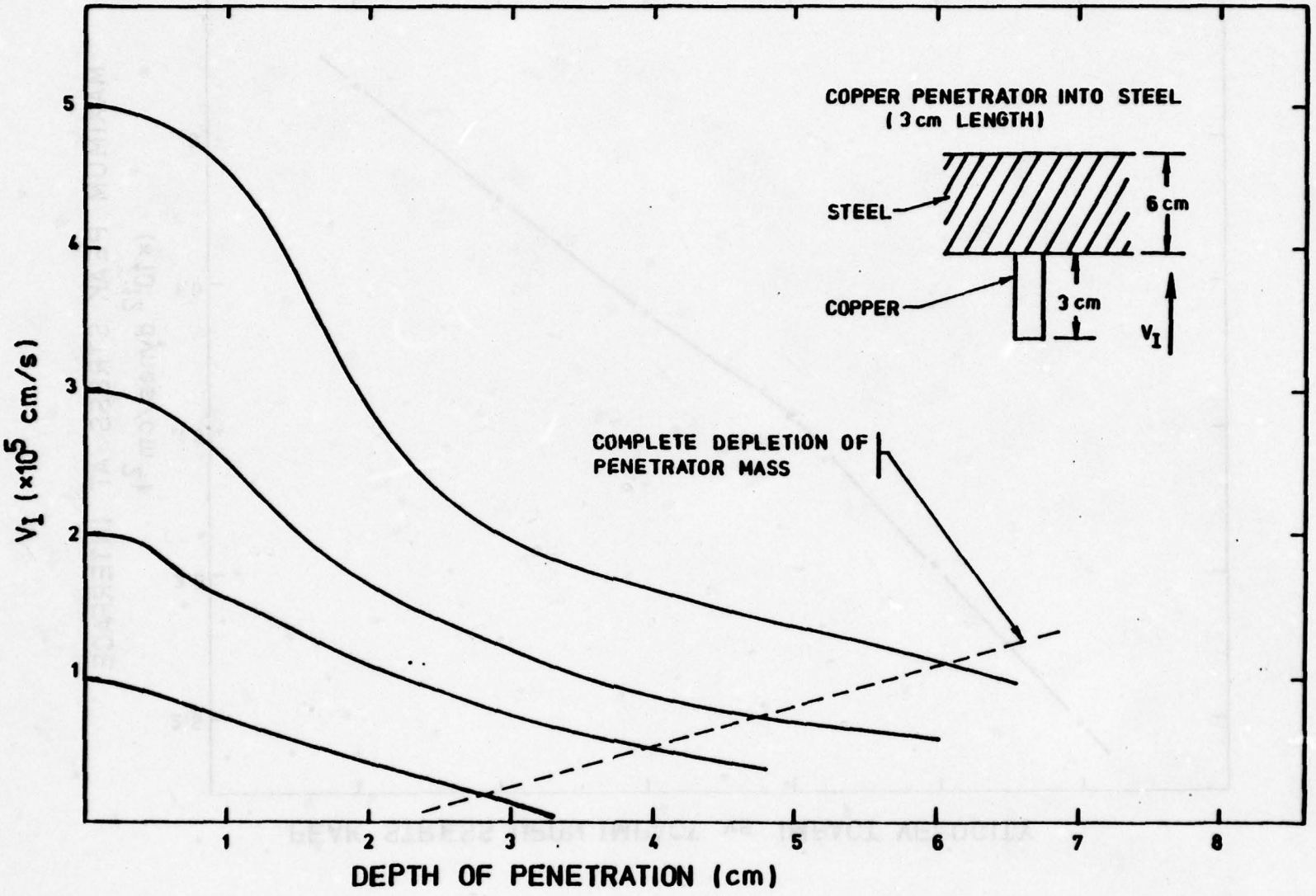

Figure 104. Average Speed of Penetrator vs. Depth

$$Sp = \frac{V_I}{2}\sqrt{\frac{\rho_\rho}{\rho_t}}$$

where V_I is the velocity at impact,

ρ_ρ is the density of the penetrator, and

ρ_t is the density of the target.

This relationship only holds until the penetrator has reacted to the traveling stress waves produced by the impact. There is then a leveling off in penetration velocity. Physically, the penetrator has imparted the majority of its kinetic energy to the plate and the plate penetrator begins to move as an ensemble. At some point, the mass of the penetrator becomes depleted due to material left along the walls of the "hole" that has been created. After complete depletion of mass, the plate plug that has received the kinetic energy and momentum of the penetrator continues to move. However, the entire plate has been set in motion, and although the depth of the hole continues to increase relative to the point of initial impact, it is not necessarily creating a deeper hole since a large area of the target has been deformed.

Scaling of penetration variables is a means of simplifying the complex nature of the penetration process. Some attempt at scaling has been attempted. Table 11 lists the data from three calculations that are similar except for the radius of the penetrator: 0.75 cm, 1.27 cm, and 2.0 cm. These calculations were run without artificail viscosity included. Compare the data in Table 11 with the data plotted in Figure 71. The difference can be attributed to artificial viscosity since the calculations were otherwise identical. As suggested by Matuska, the data from these calculations has been reformatted and scaled by scaling the distance by the penetrator radius.

Table 11 lists the scaled distances, D/R_o. The scaled data are plotted in Figure 105. It reveals a very good correlation in peak stress versus scaled distance from the penetrator-plate interface. Such a simple scaling relationship can be used as a guide to predict the peak stress at a given point within a penetrator target. It applies, of course, only to the generic types of problems presented here. However, such behavior is encouraging and indicates that other geometrical parameters may be scaled.

Table 11. Radius Study--Steel Cylinder Penetrator into Steel Target Plate

R_o = 0.75 cm			R_o = 1.27 cm			R_o = 2.00 cm		
Distance (cm)	D/R_o	Peak Stress (dynes/cm^2)	Distance (cm)	D/R_o	Peak Stress (dynes/cm^2)	Distance (cm)	D/R_o	Peak Stress (dynes/cm^2)
0	0	11.97×10^{11}	0	0	11.97×10^{11}	0	0	11.97×10^{11}
0.5	0.67	9.84×10^{11}	0.5	0.39	9.86×10^{11}	0.5	0.25	9.86×10^{11}
1.0	1.33	7.45×10^{11}	1.0	0.79	9.93×10^{11}	1.0	0.50	9.93×10^{11}
1.5	2.00	3.93×10^{11}	1.5	1.18	9.18×10^{11}	1.5	0.75	9.98×10^{11}
2.0	2.67	2.41×10^{11}	2.0	1.57	6.67×10^{11}	2.0	1.00	9.97×10^{11}
2.5	3.33	1.58×10^{11}	2.5	1.97	4.47×10^{11}	2.5	1.25	9.38×10^{11}
3.0	4.00	1.14×10^{11}	3.0	2.36	3.25×10^{11}	3.0	1.50	7.75×10^{11}
3.5	4.67	0.92×10^{11}	3.5	2.76	2.40×10^{11}	3.5	1.75	5.90×10^{11}
4.0	5.33	0.87×10^{11}	4.0	3.15	1.88×10^{11}	4.0	2.00	4.61×10^{11}
4.5	6.00	0.73×10^{11}	4.5	3.54	1.49×10^{11}	4.5	2.25	3.66×10^{11}
5.0	6.67	0.58×10^{11}	5.0	3.94	1.23×10^{11}	5.0	2.50	3.01×10^{11}
5.5	7.33	0.43×10^{11}	5.5	4.33	1.01×10^{11}	5.5	2.75	2.49×10^{11}
6.0	8.00	0.26×10^{11}	6.0	4.72	0.61×10^{11}	6.0	3.00	1.60×10^{11}

No artificial viscosity included
Initial impart velocity 3×10^5 cm/s
Steel cylinder 6 cm long
Steel target plate 6 cm thick

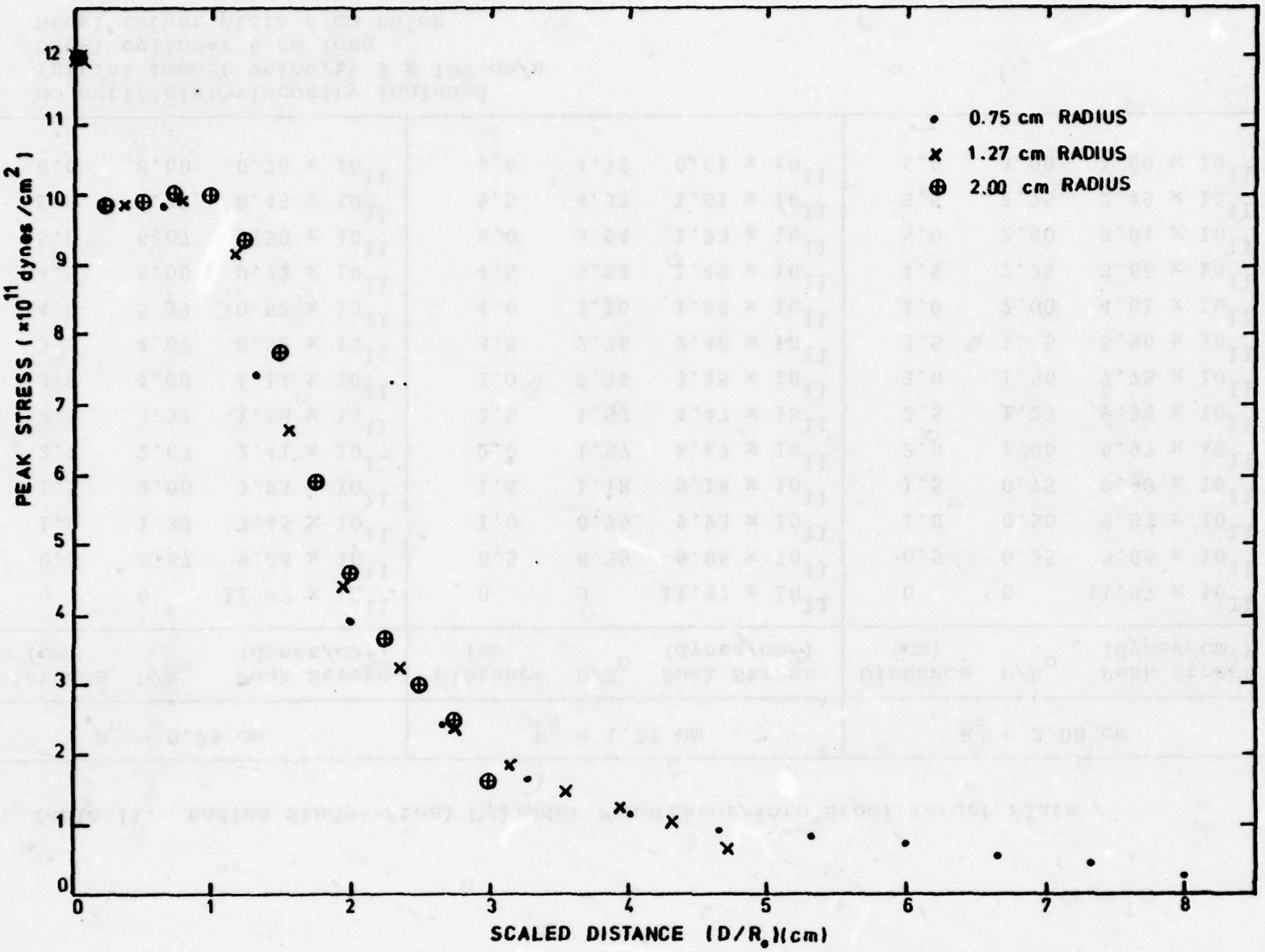

Figure 105. Scaled Distance vs. Peak Stress

SECTION VII

FIREBALL AND GROUND COUPLING CALCULATIONS USING HULL

It is the long-term goal to perform, with RADIATION HULL, meaningful calculations of the ground motion resulting from a large yield, near surface burst. As initial steps in this effort, the following has been accomplished: (a) perform fireball calculations with HULL, and (b) develop a numerical model which will enable us to calculate radiation flow across the air-ground interface.

Fireball Calculations

A fireball calculation has been performed as a test problem for the radiation option in HULL. The results of this calculation have been compared in detail with results from a 1-D Lagrangian code and the agreement is excellent.

Figure 106 indicates the initial conditions for the HULL problem. The specific internal energy of a 15-meter sphere was set to 6×10^{14} ergs/g. The density was set to 1.223×10^{-3} g/cm^3 throughout the problem mesh. There were no initial velocities. The single material in the problem was SiO_2, not air. This was because we have incorporated LASL equation-of-state and opacity tables into the code and wished to use this problem to test the added physical properties.

Figures 107 through 111 illustrate problem parameters after 3.5 μs have elapsed. The problem is reasonably spherical indicating acceptable corner coupling. Comparing the physical parameters along the axis and in the equatorial plane with results from a 1-D code, one finds excellent agreement. In Figures 112 and 113, velocity and temperature distributions along the axis in the HULL calculation are presented and compared with the physical parameters from the 1-D calculations.

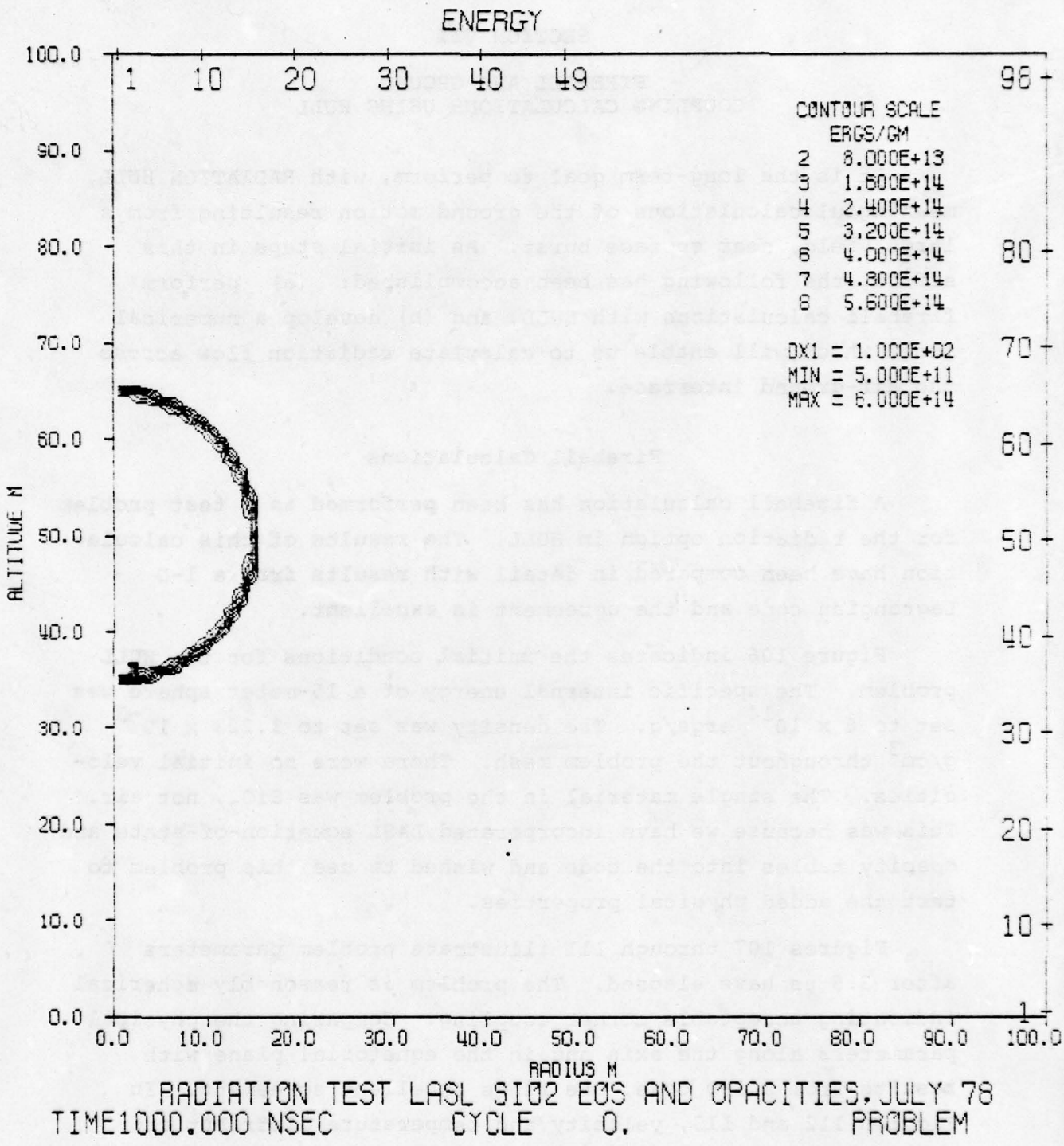

Figure 106. Energy Contours for 1.0 μs

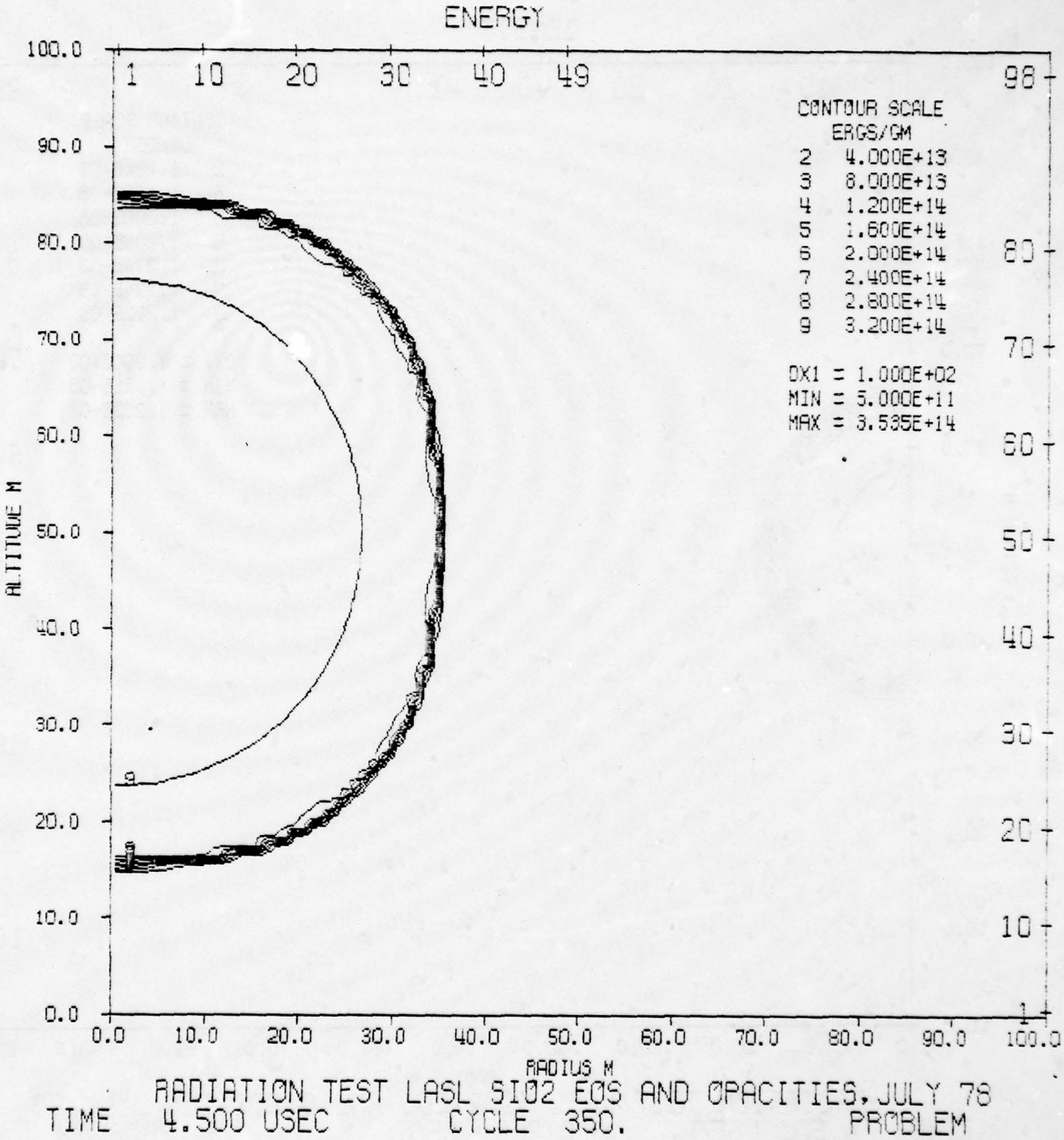

Figure 107. Energy Contours for 4.5 μs

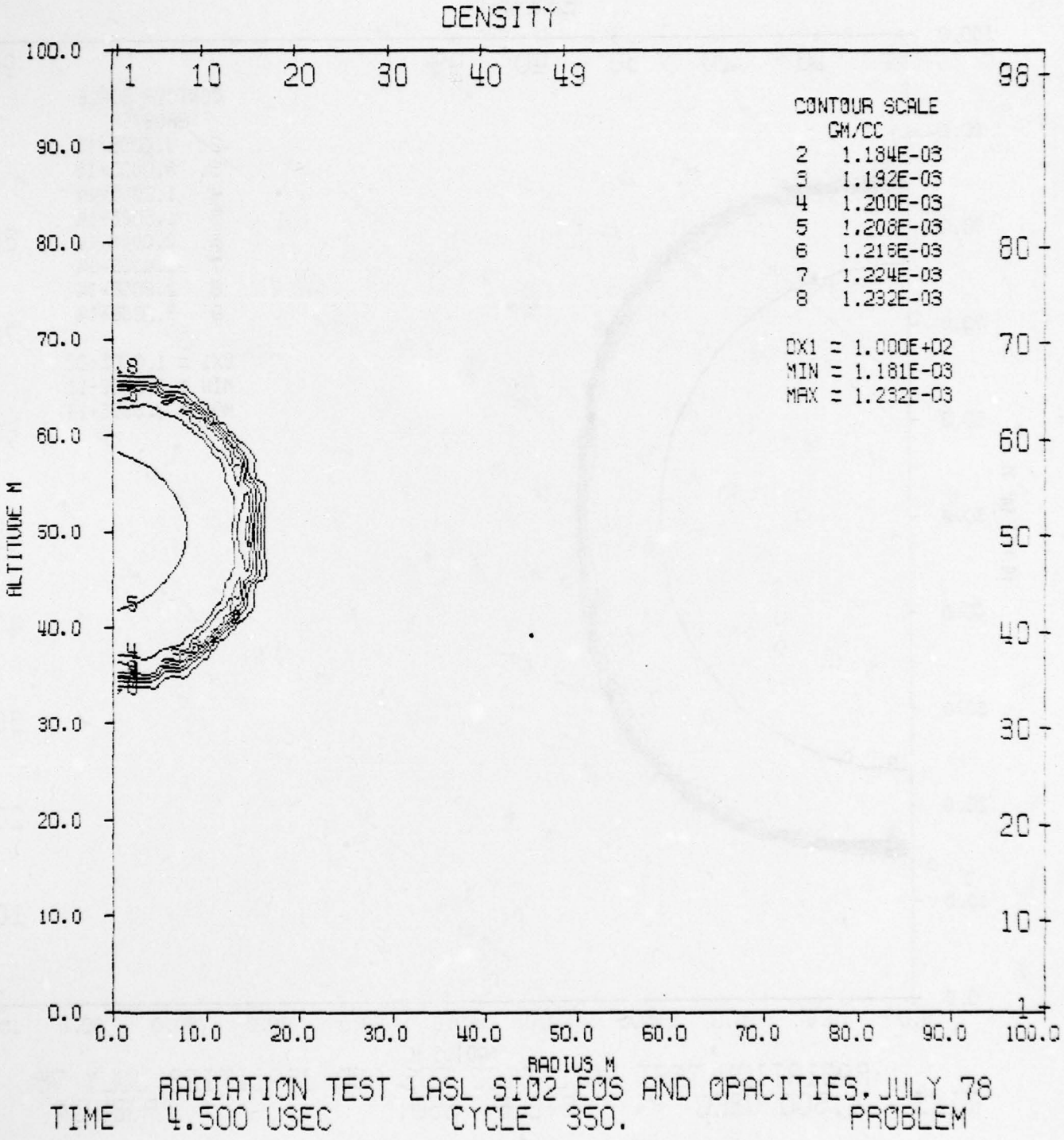

Figure 108. Density Contours for 4.5 μs

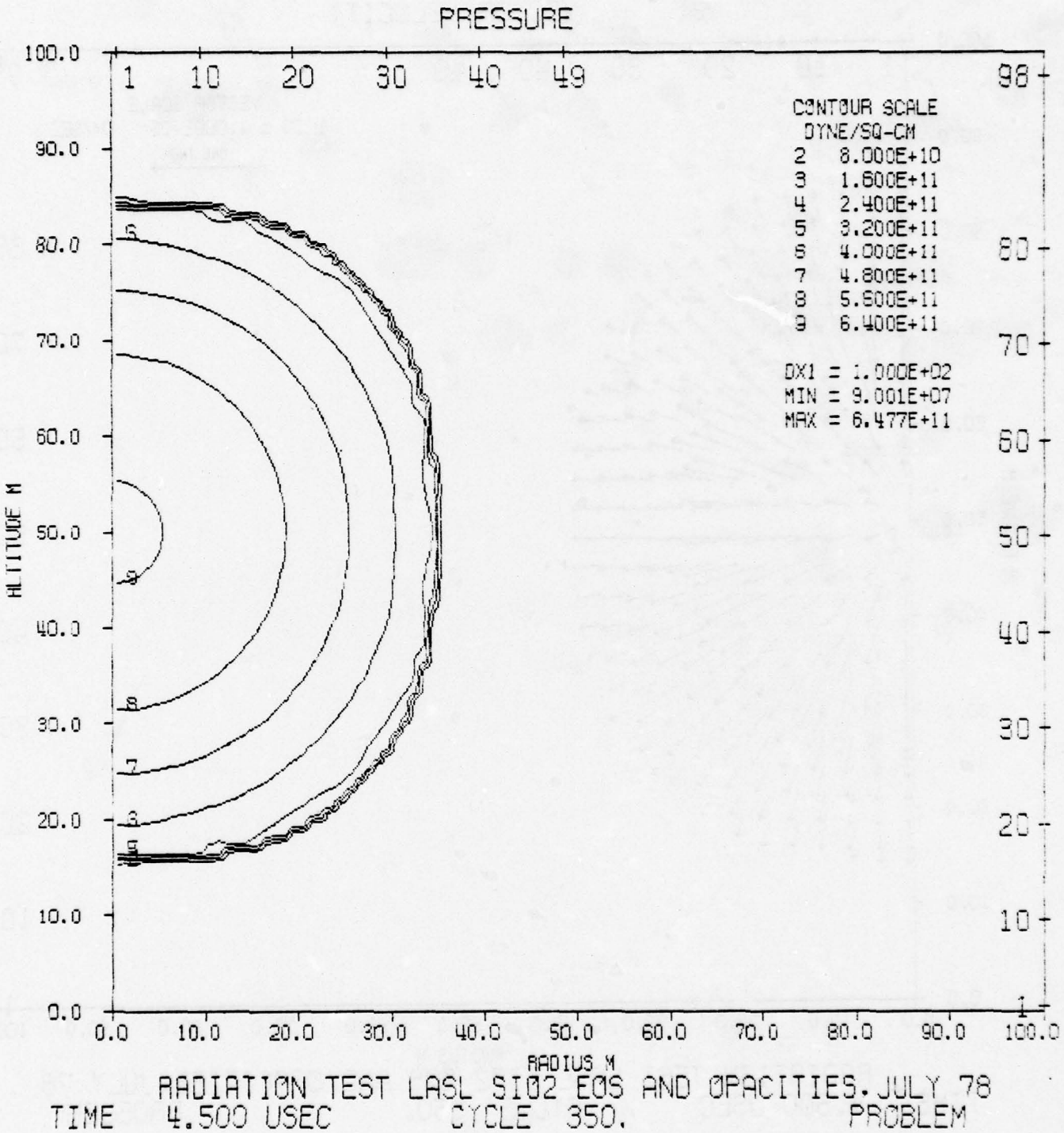

Figure 109. Pressure Contours for 4.5 μs

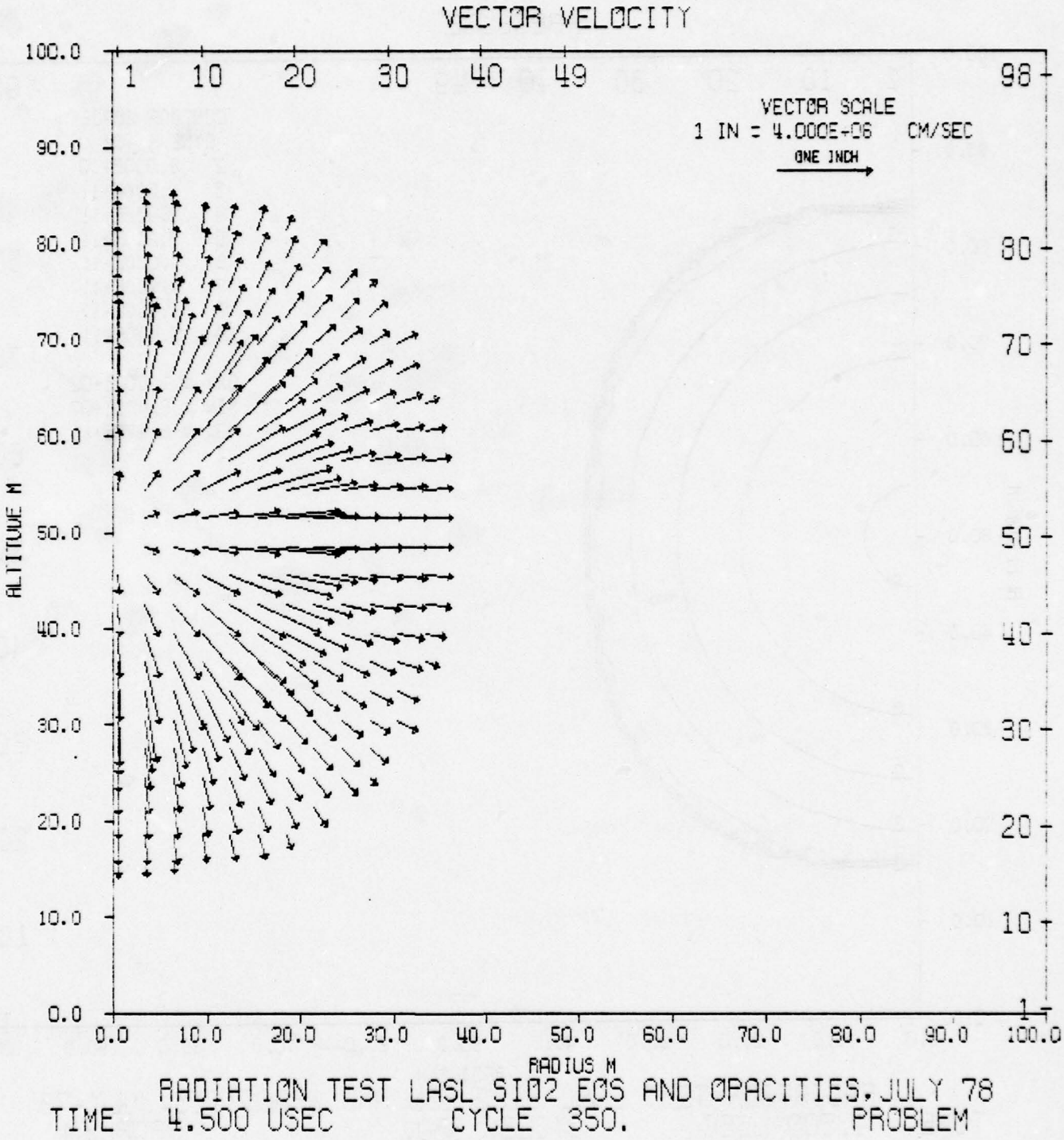

Figure 110. Vector Velocity Plot for 4.5 μs

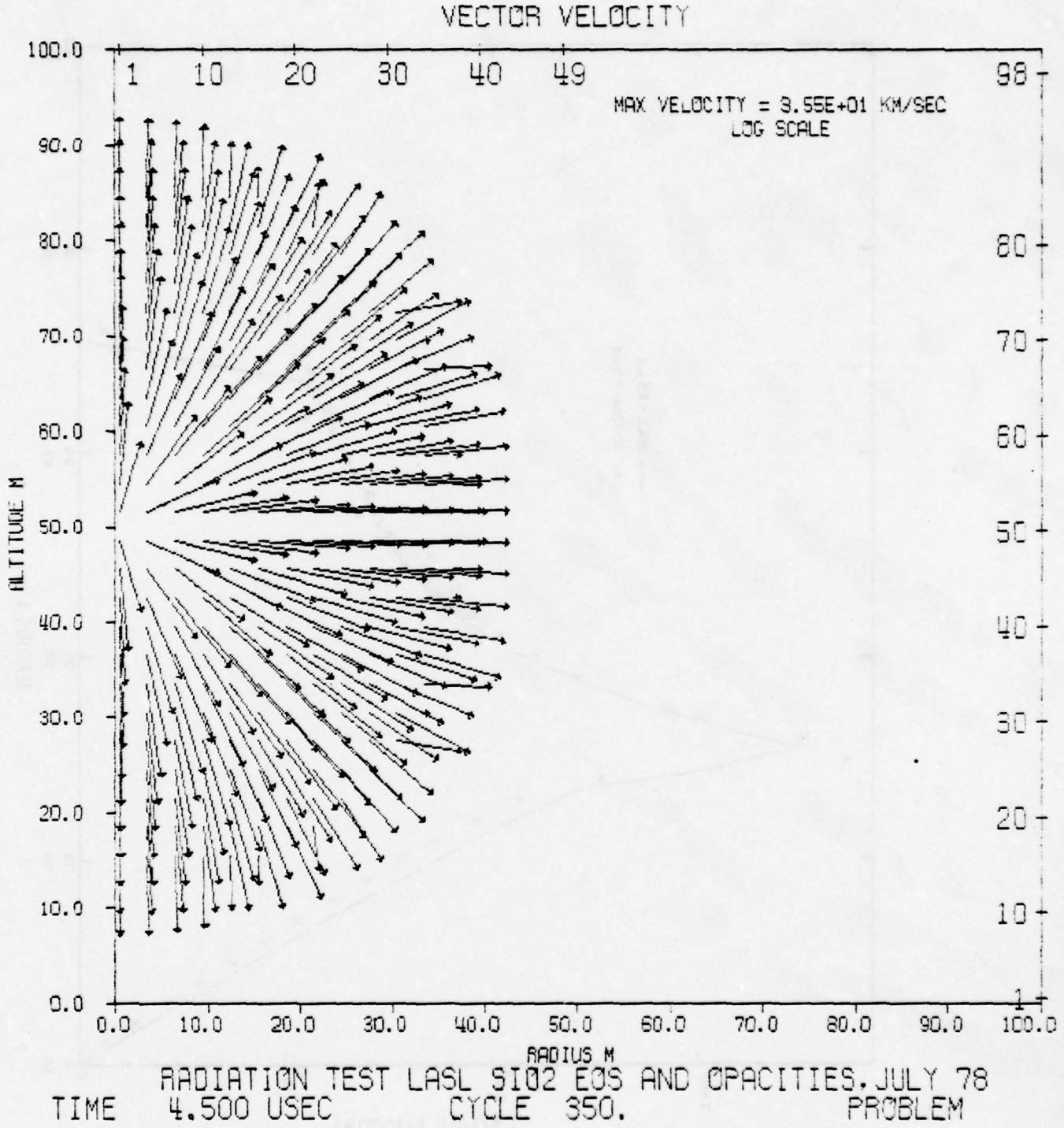

Figure 111. Log Vector Velocity Plot for 4.5 μs

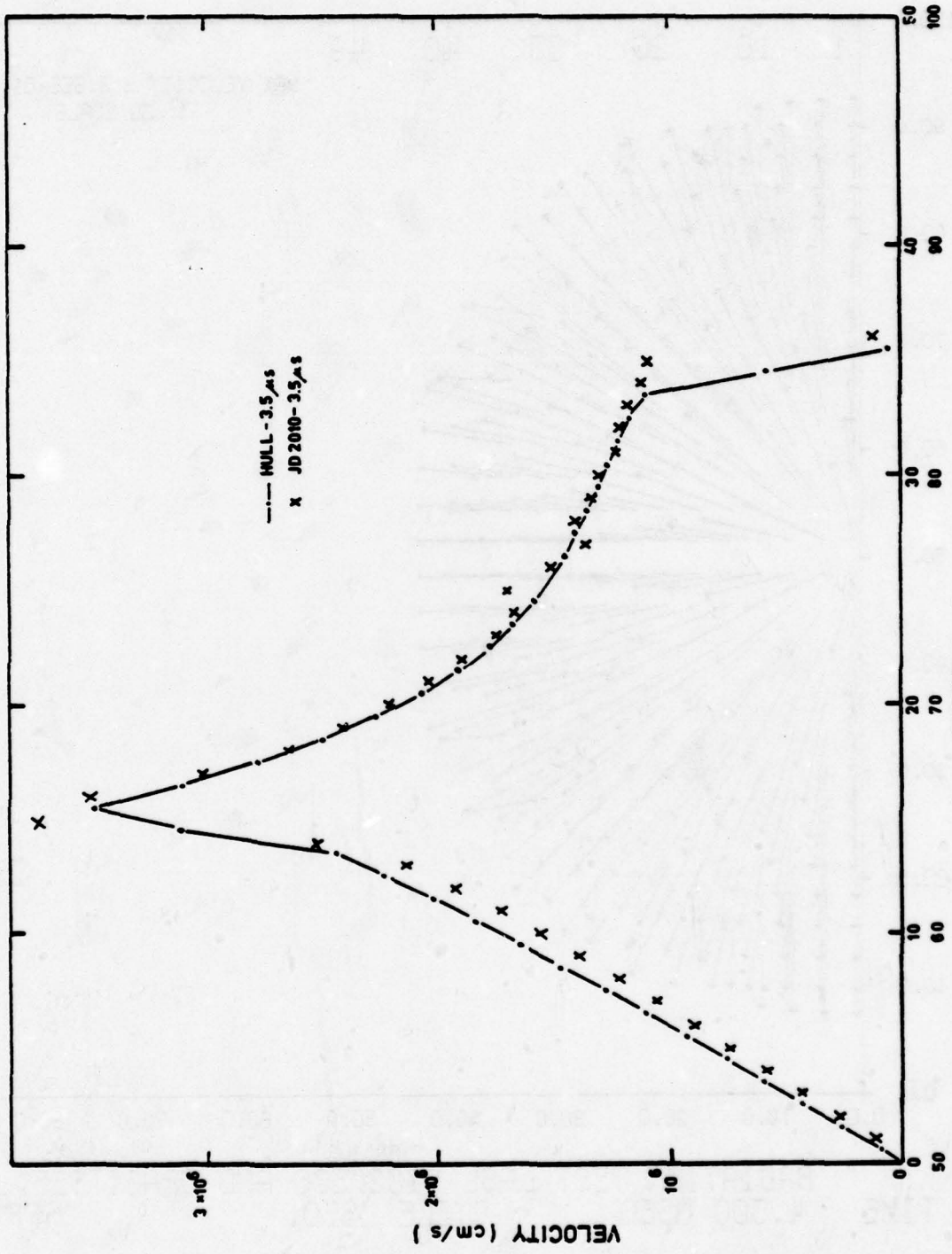

Figure 112. Comparison of Velocity Profiles at 3.5 μs

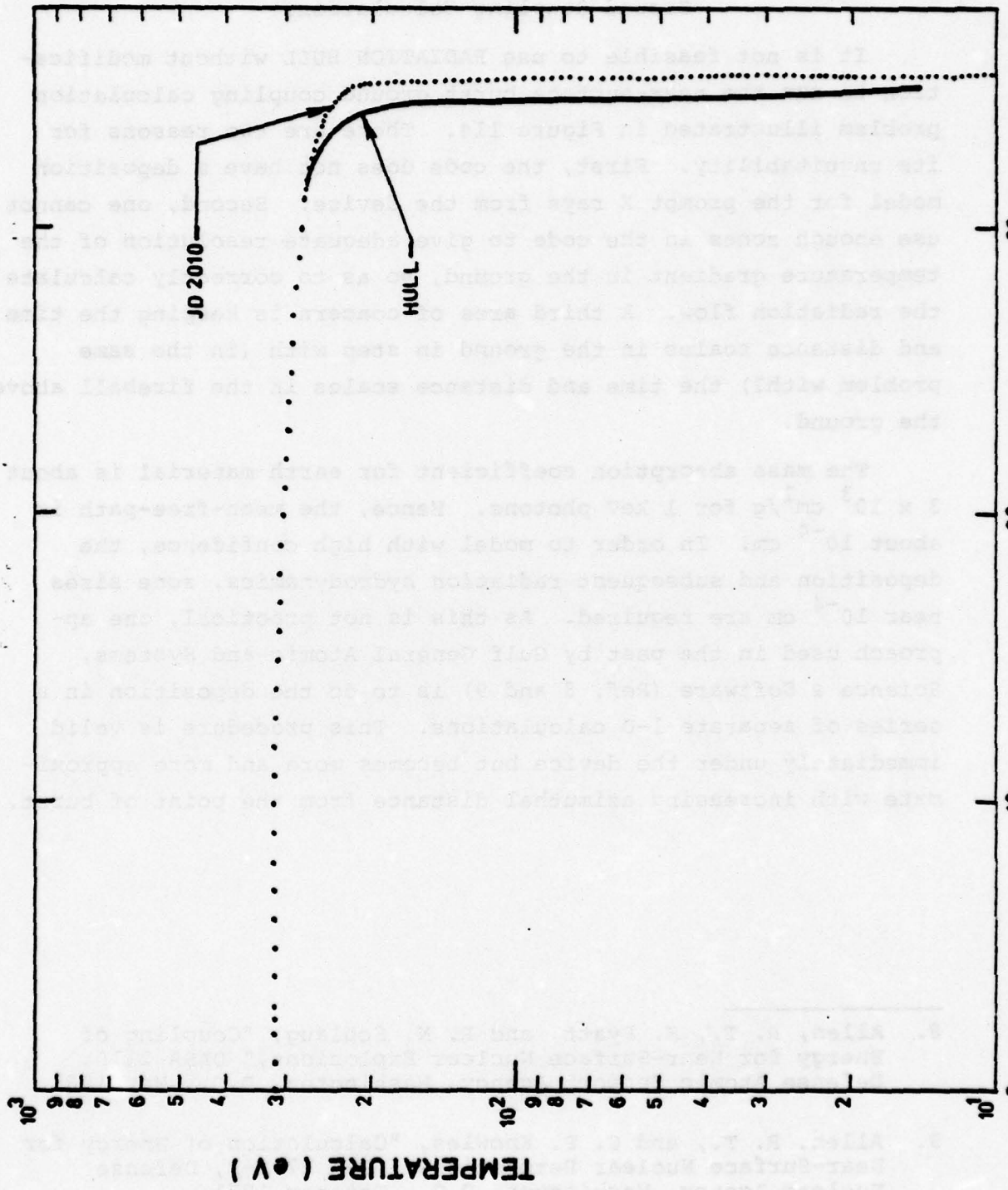

Figure 113. Comparison of Temperature Profiles at 3.5 μs

Ground Coupling Calculations

It is not feasible to use RADIATION HULL without modification to run the near-surface burst ground coupling calculation problem illustrated in Figure 114. There are two reasons for its unsuitability. First, the code does not have a deposition model for the prompt X rays from the device. Second, one cannot use enough zones in the code to give adequate resolution of the temperature gradient in the ground, so as to correctly calculate the radiation flow. A third area of concern is keeping the time and distance scales in the ground in step with (in the same problem with?) the time and distance scales in the fireball above the ground.

The mass absorption coefficient for earth material is about 3×10^3 cm^2/g for 1 keV photons. Hence, the mean-free-path is about 10^{-4} cm. In order to model with high confidence, the deposition and subsequent radiation hydrodynamics, zone sizes near 10^{-4} cm are required. As this is not practical, one approach used in the past by Gulf General Atomic and Systems, Science & Software (Ref. 8 and 9) is to do the deposition in a series of separate 1-D calculations. This procedure is valid immediately under the device but becomes more and more approximate with increasing azimuthal distance from the point of burst.

---

8. Allen, R. T., K. Pyatt, and R. N. Schlaug, "Coupling of Energy for Near-Surface Nuclear Explosions," DASA 2110, Defense Atomic Support Agency, Washington, D.C., May 1968.

9. Allen, R. T., and C. P. Knowles, "Calculation of Energy for Near-Surface Nuclear Detonations," DNA 2792-F, Defense Nuclear Agency, Washington, D.C., October 1971.

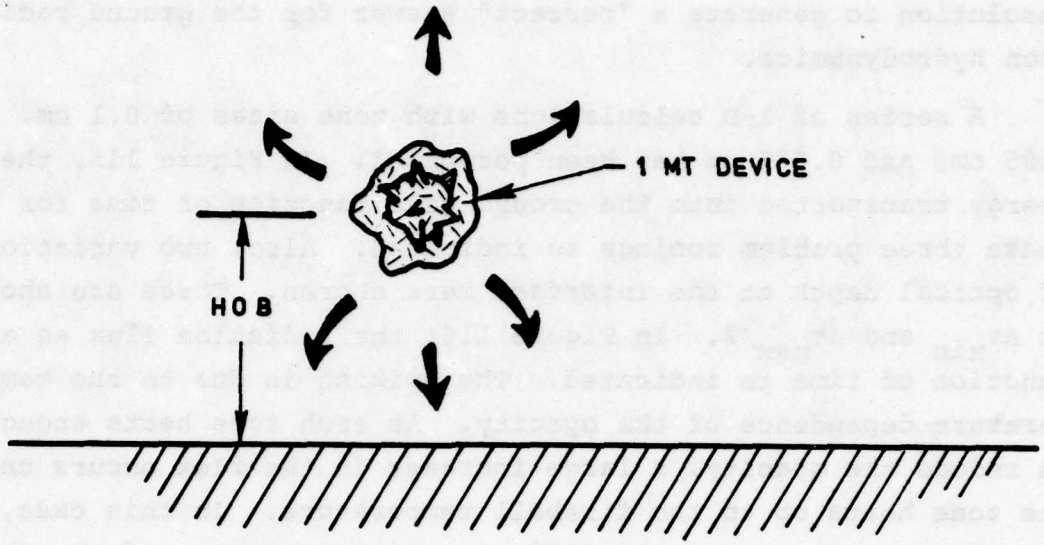

Figure 114. Schematic of 1 MT Near-Surface Burst

One would prefer to overlay an exponential deposition routine using ray tracing through the problem geometry, but this presents problems with the HULL architecture.

A related problem is correctly calculating fireball coupling to the ground. While there is considerable controversy as to the magnitude of such coupling, it is clear that in order to calculate it with high confidence, one requires zone sizes of 10^{-3} cm. This again is not feasible in a 2-D code. Using zones that are too large introduces two sources of error. First, the temperature profile is not adequately defined. Second, the radiation flux is not correctly computed, particularly at optically thick-thin interfaces. The crux of the problem is choosing an appropriate source profile and opacity profile through the discontinuity. If one chooses the larger opacity, the flux is too small while selecting the smaller opacity produces a flux which is too large. Our approach will be to develop a flux prescription for the 2-D code using 1-D calculations with sufficient

resolution to generate a "correct" answer for the ground radiation hydrodynamics.

A series of 1-D calculations with zone sizes of 0.1 cm, 0.05 cm, and 0.025 cm has been performed. In Figure 115, the energy transported into the ground as a function of time for these three problem zonings is indicated. Also, two variations of optical depth at the interface were chosen. These are shown as $\Delta\tau_{min}$ and $\Delta\tau_{max}/2$. In Figure 116, the radiation flux as a function of time is indicated. The spiking is due to the temperature dependence of the opacity. As each zone heats enough to reduce the opacity, a large increase in the flux occurs until the zone heats up to the fireball temperature. In this case, one chooses not to use the diffusion limiter option of the code.

The foregoing relates the progress in a specific problem area. Formulation of a model for the 2-D code can be very time consuming and difficult, but the result is the ability to try to solve complex problems with a 2-D code, without sacrificing large amounts of computer time.

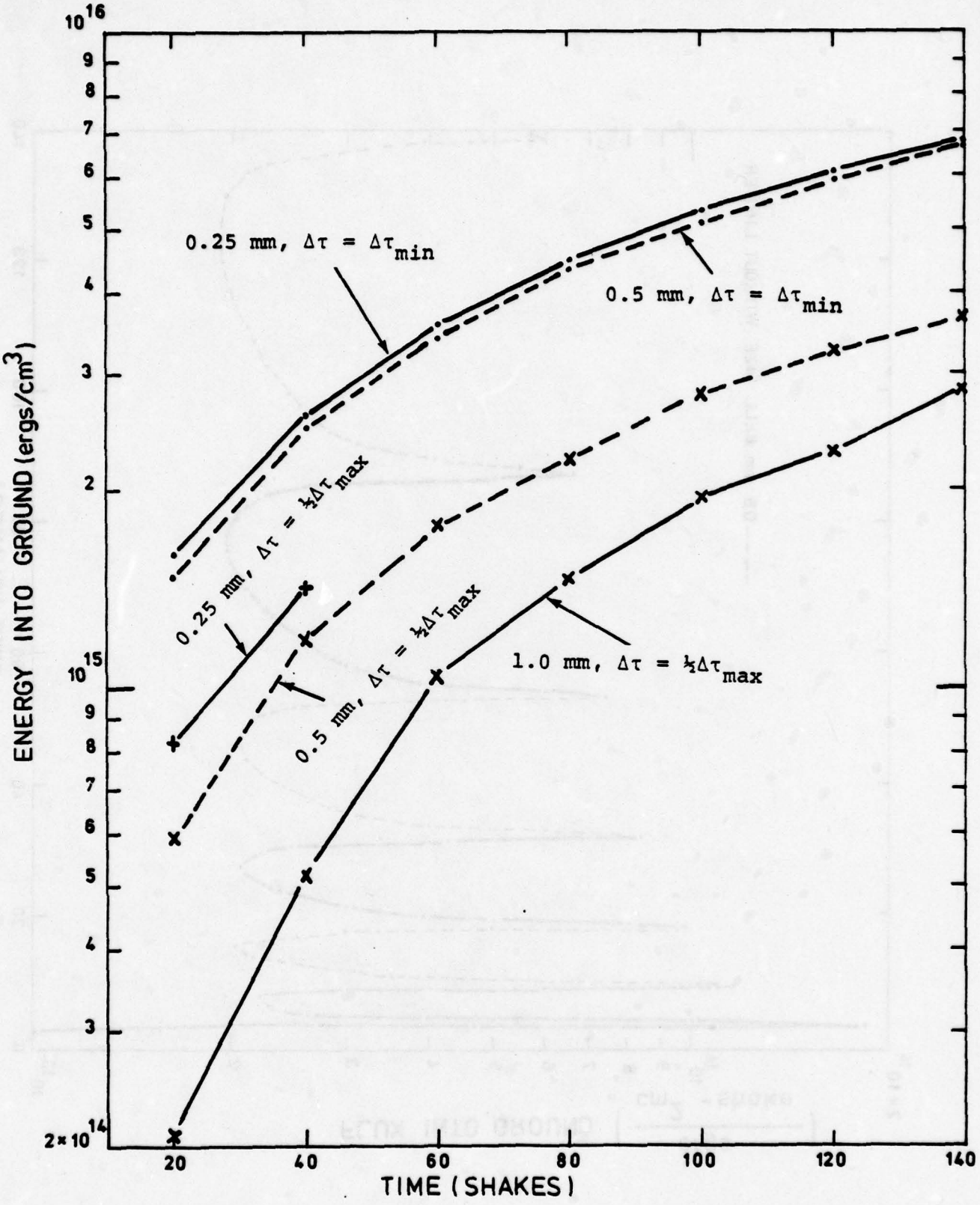

Figure 115. Energy into Ground vs. Time

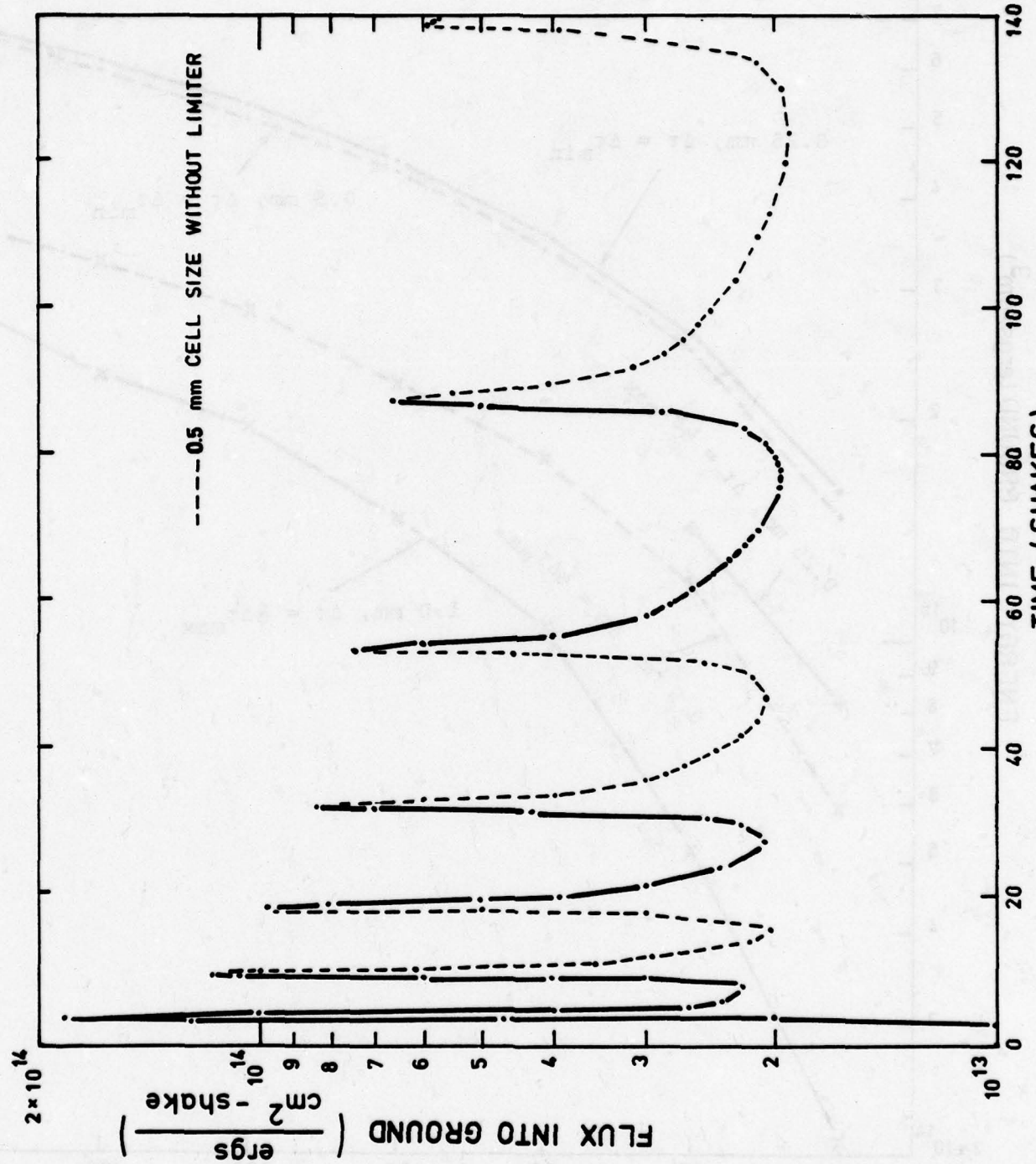

Figure 116. Flux into Ground vs. Time

SECTION VIII

HULL CODE CONVERSION

The conversion of the HULL code system to computer systems other than CDC was accomplished in two steps. First, the HULL code system was converted to the IBM 370 system which included modification of code for all other conversions. Then the code system was converted to the CRAY-1 and, specifically to the BOS (Basic Operating System), which is an early version of the CRAY Operating System (COS).

IBM Conversion

The first step in the conversion to IBM was to isolate the machine dependent functions as much as possible. This portion of the effort made the conversion to the CRAY-1 easier. It was then necessary to make modifications which were unique to the IBM system.

To perform many of the machine dependent functions, it was necessary to write a new set of utility subroutines which would isolate the machine dependent features. The new routines were: BACKUP, CDATE, NEXT, RDL, SEARCH, SINK, TIMTGO, VALVE, and WR. These routines replaced former routines in the HULL code system which performed the same functions (see Appendix A for a full description of the routines). In addition, the SAIL subroutines COMPR, STORN (FETCH), GETNUM, GTWD, INTEG, and STOR were added to the HULL code system to be used by the above mentioned subroutines or to replace existing machine dependent operations.

Other machine dependent features which required conversion were the asterisk delimited hollerith fields in the FORMAT statements. Since this is not allowed on the IBM system nor on many other systems, the hollerith fields were corrected to "H" delimited hollerith fields. This was a major effort because there were more than 200 FORMAT statements which had asterisk delimited hollerith fields.

The method for testing for an end of file is not in the ANSI 66 standard FORTRAN; therefore, a new option RDEND was established. With a value 1, the end of file test is through an "END=" parameter in the READ statement while a value of 2 means the end of file test is through a function ECF. This enables future conversion to use either type of end of file test.

The form of the multiple entry points is different on CDC and IBM systems. Therefore, IBM's form was added which accounts for all forms of the multiple entry point statement.

Finally, the declaration statement which defined variables containing character information was made into a PROC called DECLARCH. On CDC systems, it is called INTEGER, and DOUBLE PRECISION on the IBM systems.

After completing the conversion common to all systems, the changes which were unique to the IBM system were made. These changes are listed below.

Because the character variables in the IBM system were DOUBLE PRECISION, the ZBLK array must also be DOUBLE PRECISION. There was no problem for the ZBLOCK parameters that were stored in the ZBLK array as floating point (or REAL) numbers. However, the logical parameters were stored in the ZBLK array as logicals, and therefore, would only require one word of storage. Thus, an array LZBLK (NW,100,2) was equivalenced to the ZBLK (100,2) array where NW = 1 for CDC and NW = 2 for IBM. Then the logical values were stored in ZBLK (1,I,1) which was proper for both CDC and IBM systems.

Next, there were only 8 characters per character variable on the IBM system, while the CDC system had 10. Whereas the title card of 80 characters would fit into the variables ZBLK (N,1), N = 93,100 on the CDC system, it had to be stored in the variables (ZBLK (N,1), N = 93,100), (ZBLK (N,2), N = 93,94) for the IBM system.

Because of the IBM system word length of 32 bits, both the partial data blocks and station tape records had to be restructured. The comparative particle block structures are shown in Figures 117 and 118, and the comparative station records are shown in Figures 119 through 124. The partial word storage on the CDC system is accomplished by a masking function on the CDC system. On the IBM system, half word access is obtained by using the INTEGER 2 array which is equivalent to real particle or station array.

Finally, in order to obtain a stable code, it was necessary to DOUBLE PRECISION all variables used in the multimaterial equation of state.

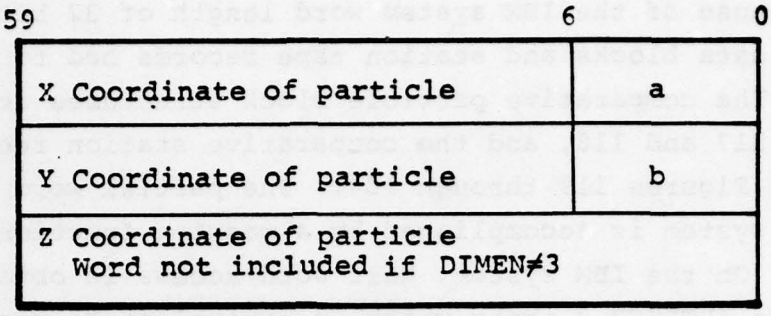

Figure 117. CDC Particle Block

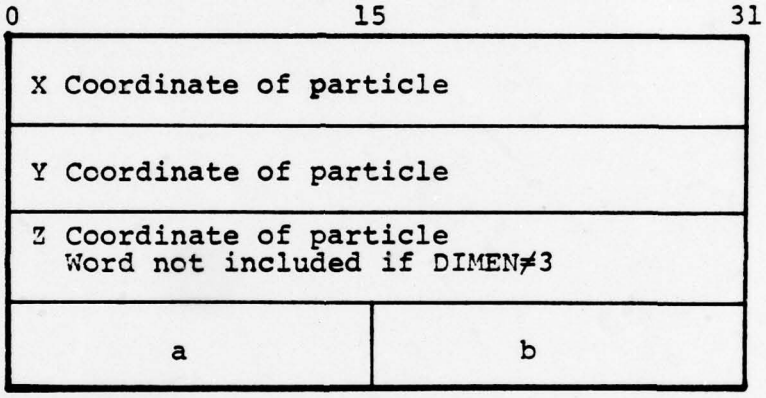

a = station or particle number

b = 'S' Euleran station

'L' Lagrangian stations

'P' Tracer particles

Figure 118. IBM Particle Block

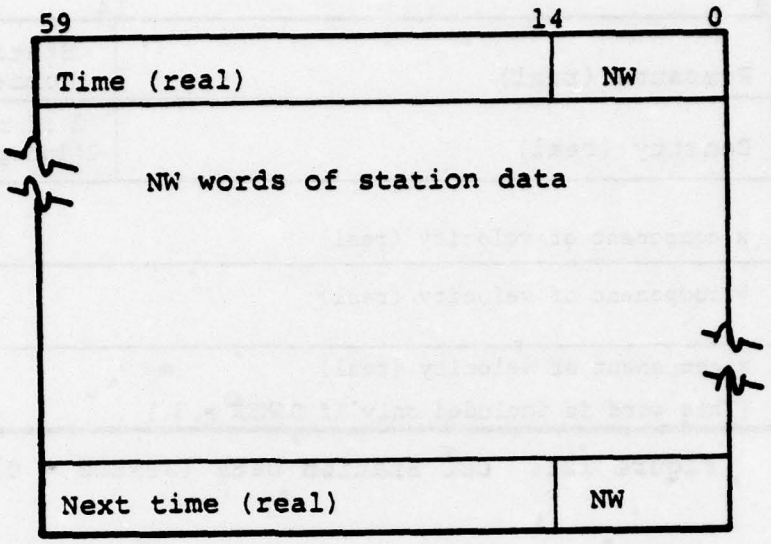

Figure 119. CDC Station Record

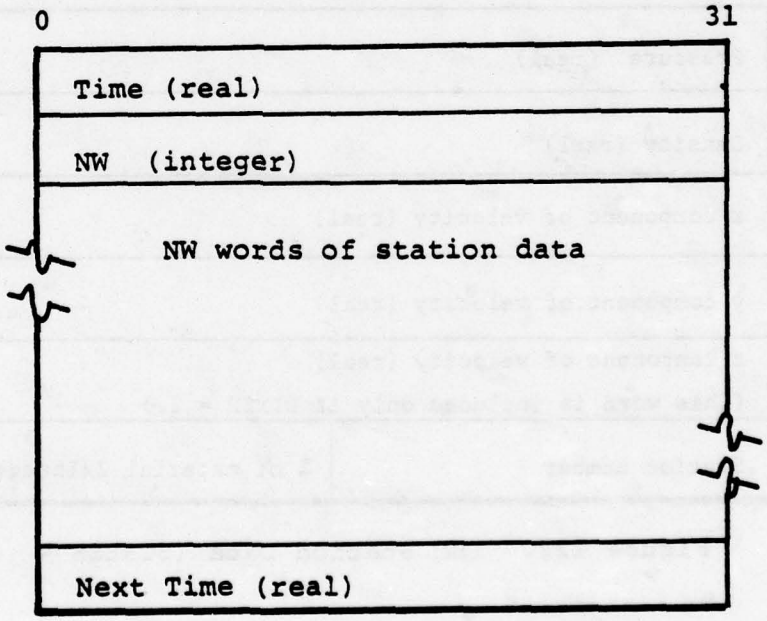

Figure 120. IBM Station Record

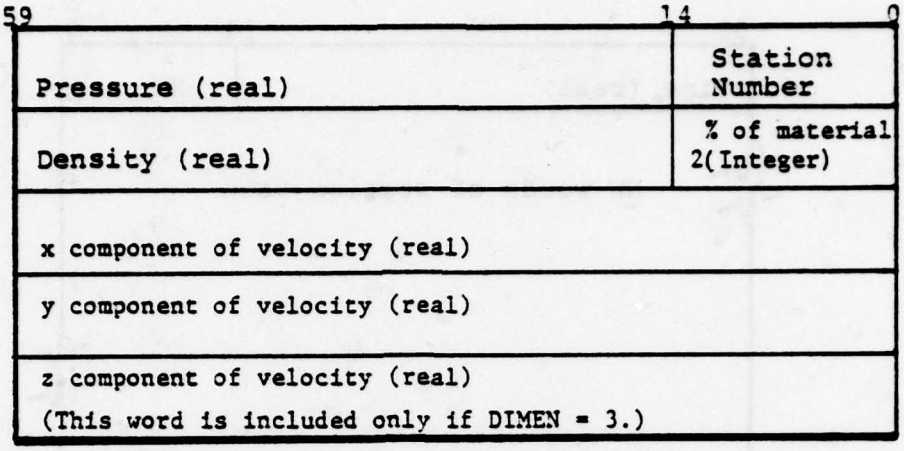

Figure 121. CDC Station Data (STRESS = 0)

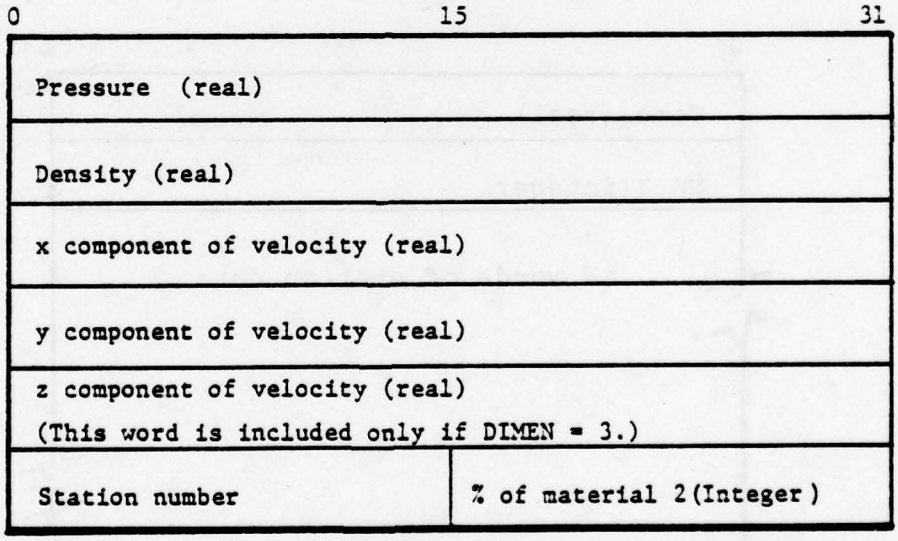

Figure 122. IBM Station Data (STRESS = 0)

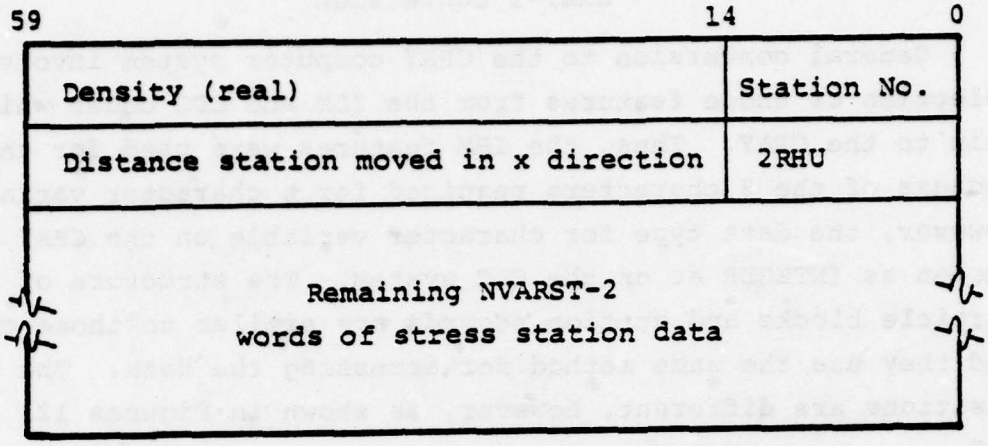

Figure 123. CDC Station Data (STRESS ≠ 0)

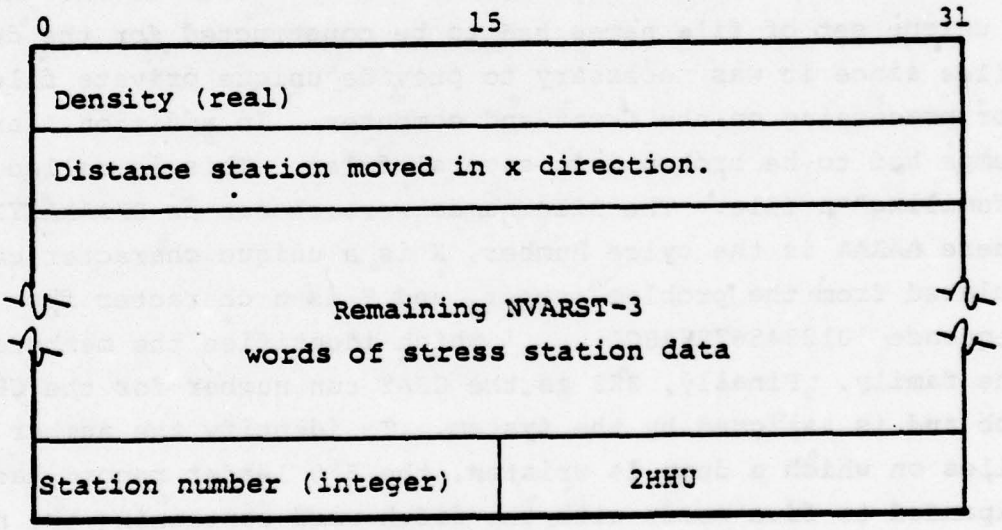

Figure 124. IBM Station Data (STRESS ≠ 0)

CRAY-1 Conversion

General conversion to the CRAY computer system involved selection of those features from the IBM and CDC codes which pertain to the CRAY. Thus, the IBM features were used for the CRAY because of the 8 characters required for a character variable. However, the data type for character variable on the CRAY was chosen as INTEGER as on the CDC system. The structure of the particle blocks and station records are similar to those on CDC, and they use the same method for accessing the data. The bit positions are different, however, as shown in Figures 125 through 128.

There were a number of modifications which became necessary for compatibility with the BOS operating system as it runs at Los Alamos Scientific Laboratory (LASL). The calls to SECOND for CP time which are used to calculate the "whiz" factor had to be changed. The TIMTGO routine had to be rewritten. Also, a unique set of file names had to be constructed for the dump files since it was necessary to provide unique private file names for processing on the front-end computer. In addition, large dumps had to be broken into several files. This is called "familing" a file. The file names were chosen as DAAAAAXYZZZ where AAAAA is the cylce number, X is a unique character calculated from the problem number, and Y is a character from the sequence '0123456789ABCD. . .' which identifies the members of the family. Finally, ZZZ is the CRAY run number for the CRAY job and is assigned by the system. To identify the number of files on which a dump is written, the 550 leader record has been expanded to five words with the fifth word containing the number of files in the family as an integer.

Because the EOF test in BOS does not work, an end of file flag, "$EOF," was added to all coded reads for the CRAY code. The UNIT function in RDL also had to be made INTEGER.

All files (both print and dump) which are disposed from the CRAY, are returned to the front-end computer as private files. Since the front-end computer system will destroy any private file after 8 hours of nonuse, a program had to be written to process the CRAY files when they arrived back at the front-end computer. This processor was written using the BCON controller. It also handles the generation and compilation of HULL.

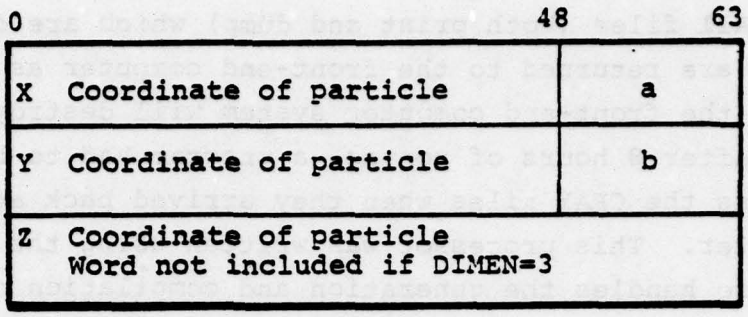

Figure 125. CRAY Particle Block

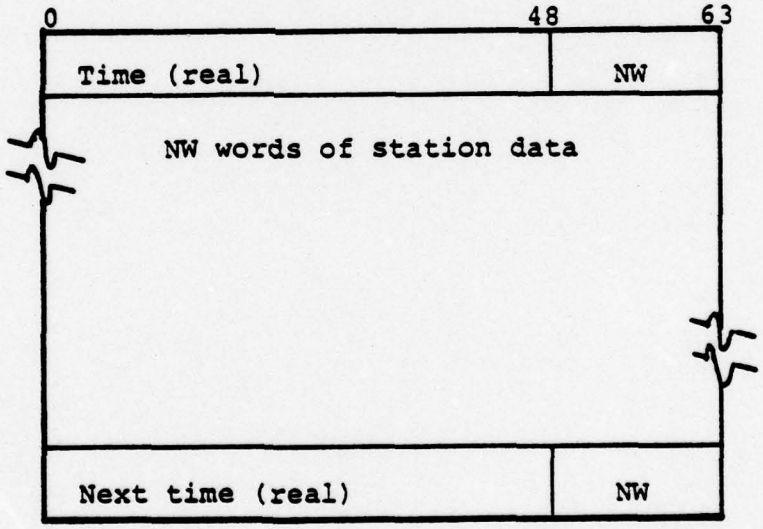

Figure 126. CRAY Station Record

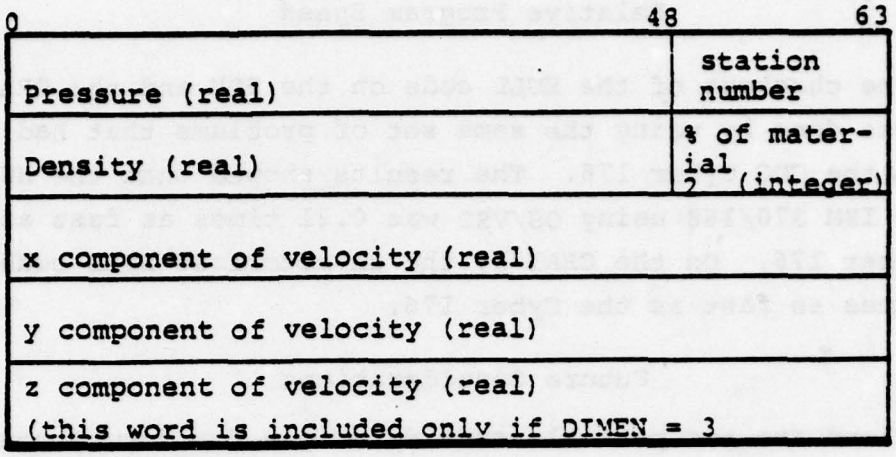

Figure 127. CRAY Station Data (STRESS = 0)

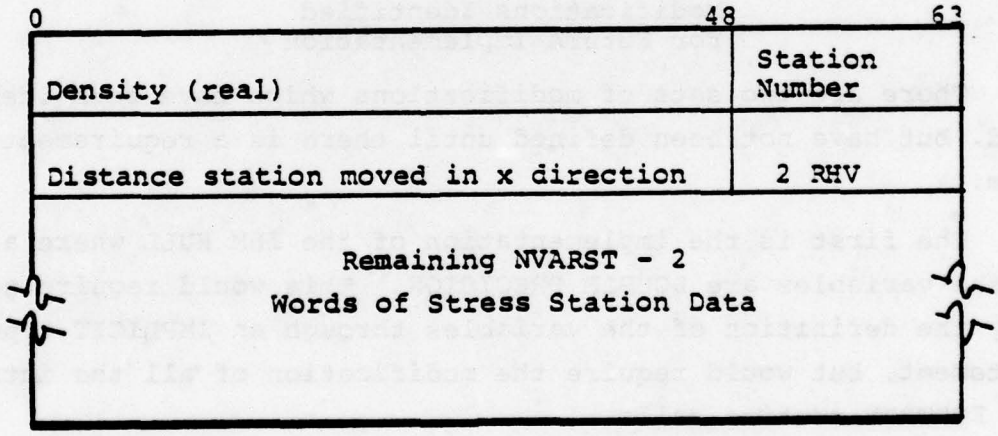

Figure 128. CRAY Station Data (STRESS ≠ 0)

Relative Program Speed

The checkout of the HULL code on the IBM and the CRAY systems was done by using the same set of problems that had been run on the CDC Cyber 176. The results showed that the HULL code on the IBM 370/168 using OS/VS2 was 0.21 times as fast as on the Cyber 176. On the CRAY-1, the unvectorized HULL code was 2.1 times as fast as the Cyber 176.

Future Considerations

There are two possible considerations for future conversion. First, the code necessary to run HULL on a CRAY-1 using COS (CRAY Operating System) is already present with the exception of about 3 assembly routines. Finally, if CDC transitions to the new compiler FTN5, the code can be modified by correcting the octal constants used for masking.

Modifications Identified for Future Implementation

There are two sets of modifications which have been identified, but have not been defined until there is a requirement for them.

The first is the implementation of the IBM HULL where all of the variables are DOUBLE PRECISION. This would require not only the definition of the variables through an IMPLICIT type statement, but would require the modification of all the intrinsic FORTRAN routine calls.

Also, the interactive particle (CODE=2) option in HULL is currently not functioning. To reimplement this option, the KEEL portion for interactive particles must be rewritten. In addition, the code should be modified to handle both noninteractive and interactive particles so stations could be run with interactive particles.

APPENDIX A

SUMMARY OF NEW HULL SYSTEM ROUTINES

During the conversion effort, certain routines were either written or redesigned. Some of these routines use routines from the SAIL system. This appendix describes the function and calling sequence of the SAIL system routines used and the new HULL library routines.

NAME: COMPR

PURPOSE: To compare character strings.

ENTRY: LOGICAL FUNCTION COMPR (M1, I1, NCR, M2, I2)

Description of Parameters

Name	Type	I/O	Usage
M1	character	I	first character string
I1	integer	I	relative position of first character to be compared
NCR	integer	I	number of compared characters
M2	character	I	second character string
I2	integer	I	relative positive of first character to be compared in second *string*
COMPR	logical	O	= .TRUE. if strings are equal = .FALSE. if not

NAME: FETCH

PURPOSE: To extract integers packed in a character word.

ENTRY: SUBROUTINE FETCH (N, I1, I2, I3)

Description of Parameters

Name	Type	I/O	Usage
N	character word (integer - CDC) (real*8 - IBM)	I	character word containing the integers
I1	integer	O	integer contained in first quarter of word
I2	integer	O	integer contained in second quarter of word
I3	integer	O	integer contained in last half of word

NAME: GETNUM

PURPOSE: To decode numbers of the form XXX.YYY.

ENTRY: SUBROUTINE GETNUM (NCARD, IS, IB, IC, IFN)

Description of Parameters

Name	Type	I/O	Usage
NCARD	character	I	field to be scanned for number
IS	integer	I	the first character position in NCARD to be scanned for number
		O	if IFN < 0, the character position of the first nonblank character
			if < 0, no nonblank characters were encountered in scan
			if > 0, first character position past number decoded
IB	integer	O	integer value of number found prior to a blank or period
IC	integer	O	integer value of number found after period; zero if none found
IFN	integer	I	the last character position to be scanned for number
		O	if < 0, IFN is the character position of a character which could not be decoded into a number
			if > 0, contains number of characters found in decoding IC

NAME: GTWD

PURPOSE: To parse a character unit from a character string.

ENTRY: SUBROUTINE GTWD (IWD, NCARD, IS, IFN)

Description of Parameters

Name	Type	I/O	Usage
IWD	character	O	the character unit generated (maximum 20 characters on CDC and 16 characters on IBM)
NCARD	character	I	the character string to be parsed
IS	integer	I	the first character position for the parsing scan
		O	if IFN > 0, the first character position past the unit assembled
IFN	integer	I	last character of NCARD to be scanned
		O	if < 0, field contained no non-blank characters
			if > 0, number of characters in unit assembled

NAME: INTEG

PURPOSE: To convert an integer into a character string.

ENTRY: SUBROUTINE INTEG (NX, IFL, NCR, IFC)

Description of Parameters

Name	Type	I/O	Usage
NX	integer	I	number to be converted
IFL	character	O	character string to contain number; must be 24 characters long on IBM and 30 characters long on CDC
NCR	integer	O	number of characters generated for the number
IFC	integer	O	position of first character of string generated

NAME: STOR

PURPOSE: To transfer character strings.

ENTRY: SUBROUTINE STOR (M1, M2, I1, NCR, I2)

Description of Parameters

Name	Type	I/O	Usage
M1	character	I	character string into which the characters are to be transferred
M2	character	O	character string from which the characters are to be transferred
I1	integer	I	position in M2 where first character is to be placed when transferred
NCR	integer	I	number of characters to be transferred
I2	integer	I	position in M2 of first character to be transferred

SAIL LIBRARY ROUTINES

NAME: STORN

PURPOSE: To store three integers packed in a character word.

ENTRY: SUBROUTINE STORN (N, I1, I2, I3)

Description of Parameters

Name	Type	I/O	Usage
N	character word (integer CDC) (real*8 IBM)	O	word into which the integers are to be stored
I1	integer	I	integer to be stored in first quarter of word
I2	integer	I	integer to be stored in second quarter of word
I3	integer	I	integer to be stored in second half of word

HULL LIBRARY ROUTINES

NAME: BACKUP

PURPOSE: To backspace a record written by RDC.

ENTRY: SUBROUTINE BACKUP (LFN, N)

Description of Parameters

Name	Type	I/O	Usage
LFN	unit	I	unit to be backspaced
N	integer	I	number of RDC records to be backspaced

NAME: CDATE

PURPOSE: To return current date.

ENTRY: SUBROUTINE CDATE (DT)

Description of Parameters

Name	Type	I/O	Usage
DT	character	O	date is in format BDDMMMYY where B = blank DD = day of month MMM = month YY = year

NAME: NEXT

PURPOSE: To scan card image and generate next parsed element.

ENTRY: SUBROUTINE NEXT

Common Blocks Accessed

Name	Type	Common	Usage
CARD	character	/CARD/	current card image
TEST, TESTC	character	/CARD/	parsed character unit generated
IPOINT	integer	/CARD/	scan point at both beginning and end of scan
NCHAR	integer	/CARD/	number of characters in TEST, TESTC
NCOL	integer	/CARD/	number of characters of CARD to be scanned
EOFC	character	/EOF/	test set to this value if read produces an end of file

NAME: RDL

PURPOSE: To read a block of data and return the length read.

ENTRY: SUBROUTINE RDL (NT, DT, LN, IRTN)

Description of Parameters

Name	Type	I/O	Usage
NT	any	I	the file to be read
DT	any	O	the origin of the block which will contain the data read
LN	integer	I	the number of words in the block
		O	the number of words read
IRTN	integer	O	return code -1 successful read 0 end of file encountered +1 error in read

HULL LIBRARY ROUTINES

NAME: RDL2

PURPOSE: To read into level 2 variables on CDC 7600 and Cyber 176

ENTRY: SUBROUTINE RDL2 (PT, LN, IRTN)

Description of Parameters

The parameters are identical with those for RDL.

NAME: SEARCH

PURPOSE: To locate a data record beginning with a specified keyword.

ENTRY: SUBROUTINE SEARCH (WORD, I, NREC)

Description of Parameters

Name	Type	I/O	Usage
WORD	character	I	keyword for search
I	integer	O	= 1 record found = 2 record not found
NREC	integer	O	record number of keyword

Input file is positioned so that calls to NEXT and value will process record beginning with the keyword.

NAME: TIMTGO

PURPOSE: To get the remaining job CPU time on CDC system.

ENTRY: SUBROUTINE TIMTGO (SEC)

Description of Parameters

Name	Type	I/O	Usage
SEC	integer	O	The amount of CPU time (sec) remaining until the current time limit is reached.

NAME: VALUE

PURPOSE: To decode a number or a logical constant.

ENTRY: SUBROUTINE VALUE (WS, ITYPE)

Description of Parameters

Name	Type	I/O	Usage
WS	real	O	number or logical value
ITYPE	integer	O	conversion type = 1 number WS set = 2 logical WS set = 3 character WS not set

Common Block Reference

NAME	Type	Common	Usage
CARD	character	/CARD/	card image being scanned
TEST, TESTC	character	/CARD/	parsed character unit
IPOINT	integer	/CARD/	current character pointer
NCHAR	integer	/CARD/	number of characters in TEST, TESTC
NCOL	integer	/CARD/	number of characters to scan on card

NAME: WRE

PURPOSE: To wait for the completion of asynchronous output.

ENTRY: SUBROUTINE WRE (NU)

Description of Parameters

Name	Type	I/O	Usage
NU	unit	I	file for which the completion of the output operation is desired

NAME: WR

PURPOSE: To write a block of data.

ENTRY: SUBROUTINE WR (NO, BLOCK, LN, IRTN)

Description of Parameters

Name	Type	I/O	Usage
NO	unit	I	file to be written
BLOCK	any	I	origin of the block to be written
LN	integer	I	number of words to be written
IRTN	integer	O	return code = -1 successful write = 1 error in write

NAME: WRR

PURPOSE: To write a block to a file but return to CPU execution immediately on systems that have asynchronous I/O capability in FORTRAN.

ENTRY: SUBROUTINE WRR (NO, BLOCK, LN, IRTN)

Description of Parameters

The parameters are identical to those in WR.

NAME: WRR2

PURPOSE: To write a block from level 2 on CDC 7600 and Cyber 176 system with immediate return.

ENTRY: SUBROUTINE WRR2 (NO, BLOCK, LN, IRTN)

Description of Parameters

The parameters are identical to those in WR.

NAME: WR2

PURPOSE: To write a block for level 2 on CDC 7600 and Cyber 176 systems.

ENTRY: SUBROUTINE WR2 (NO, BLOCK, LN, IRTN)

Description of Parameters

The parameters are identical to those in WR.